MEASUREMENT AND APPLICATION OF OPTICAL NONLINEARITIES IN INDIUM PHOSPHIDE, CADMIUM MERCURY TELLERIDE AND PHOTONIC CRYSTAL FIBRES

Trefor James Sloanes

A Thesis Submitted for the Degree of DEng
at the
University of St. Andrews

2009

Full metadata for this item is available in the St Andrews
Digital Research Repository
at:
https://research-repository.st-andrews.ac.uk/

Please use this identifier to cite or link to this item:
http://hdl.handle.net/10023/723

This item is protected by original copyright

Measurement and Application of Optical Nonlinearities in Indium Phosphide, Cadmium Mercury Telluride and Photonic Crystal Fibres

This thesis is presented in application for the
degree of Doctor of Engineering
to the University of St. Andrews

by

Trefor James Sloanes

I, Trefor James Sloanes, hereby certify that this thesis, which is approximately 28,500 words in length, has been written by me, that it is the record of work carried out by me and that it has not been submitted in any previous application for a higher degree.

I was admitted as a research student in October, 2003 and as a candidate for the degree of Doctor of Engineering in August, 2004; the higher study for which this is a record was carried out in the University of St Andrews between 2003 and 2008.

date ……………… signature of candidate ………………

I hereby certify that the candidate has fulfilled the conditions of the Resolution and Regulations appropriate for the degree of Doctor of Engineering in the University of St Andrews and that the candidate is qualified to submit this thesis in application for that degree.

date ………………signature of supervisor ………………

In submitting this thesis to the University of St Andrews we understand that we are giving permission for it to be made available for use in accordance with the regulations of the University Library for the time being in force, subject to any copyright vested in the work not being affected thereby. We also understand that the title and the abstract will be published, and that a copy of the work may be made and supplied to any bona fide library or research worker, that my thesis will be electronically accessible for personal or research use unless exempt by award of an embargo as requested below, and that the library has the right to migrate my thesis into new electronic forms as required to ensure continued access to the thesis. We have obtained any third-party copyright permissions that may be required in order to allow such access and migration, or have requested the appropriate embargo below.

The following is an agreed request by candidate and supervisor regarding the electronic publication of this thesis:

Access to Printed copy and electronic publication of thesis through the University of St Andrews.

date …………signature of candidate …………signature of supervisor …………

Abstract

The two-photon absorption (TPA) coefficient is measured in indium phosphide (InP) using femtosecond pulses to be 45cm/GW at 1.32μm. Nanosecond pulses are subsequently used to find the free-carrier refractive index cross-section, σ_r, and the free-carrier absorption coefficient, σ_{fca}. The quantity $\beta\sigma_r$ is measured to be $-113\text{x}10^{-20}$cm^4/GW at 1.064μm and $-84\text{x}10^{-20}$cm^4/GW at 1.534μm. At 1.064μm, with β assumed to be 22cm/GW, the value suggested by theory, σ_r is $-5.1\text{x}10^{-20}$cm^3. Similarly, at 1.534μm, assuming β to be 20cm/GW gives a σ_r value of $-4.1\text{x}10^{-20}$cm^3. Due to refraction affecting the measurements of σ_{fca}, only an upper limit of $1\text{x}10^{-15}$cm^2 can be put on its value.

The free-carrier experiments are repeated on two samples of cadmium mercury telluride (CMT) having bandgaps of 0.89eV and 0.82eV. For the first sample, $\beta\sigma_r$ is measured to be $-148\text{x}10^{-20}$cm^4/GW. Assuming β to be 89cm/GW gives a σ_r value of $-1.7\text{x}10^{-20}$cm^3 whilst σ_{fca} is found to be at most $3\text{x}10^{-15}$cm^2. Significant linear absorption occurs in the second sample which generates a large free-carrier population. It is shown that this significantly enhances the nonlinearities. Finally, the results of the work are tested by modelling a nonlinear transmission experiment, and the results found in this work give a closer fit to experimental results than the result of theory.

Four-wave mixing (FWM) in a photonic crystal fibre is exploited to create a high output power optical parametric amplifier (OPA). To optimise the OPA conversion efficiency, the fibre length has to be increased to 150m, well beyond the walk-off distance between the pump and signal/idler. In this regime, the Raman process can take over from the FWM process and lead to supercontinuum generation. The OPA exhibits up to 40% conversion efficiency, with the idler (0.9μm) and the signal (1.3μm) having a combined output power of over 1.5W.

Acknowledgements

First and foremost I wish to thank my two supervisors at DSTL, Drs Phil Milsom and Ken McEwan, for all of their support and help throughout my doctorate. Their advice has been invaluable in the production of this work. Also at DSTL, thanks go to Dr. Steve Till for reviewing my thesis, and to the members of the team, past and present, who have kept things entertaining during my time here.

From Qinetiq I must thank Dr Laurent Michaille for providing tutoring and assistance with the photonic crystal fibre experiments, not to mention providing the fibre in the first place.

From St. Andrews I wish to thank my academic supervisor, Prof. Alan Miller, without whom I wouldn’t be doing this doctorate in the first place. I also must thank Arvydas Ruseckis for assisting with the femtosecond experiments.

Last but by no means least, I must thank my parents, who have supported and encouraged me throughout my academic studies, and my girlfriend, Kathryn, for sticking by me and encouraging me even when distance kept us apart.

List of publications

"Two-photon induced free carrier absorption and refraction in Indium Phosphide", T.J. Sloanes, P.K. Milsom, K.J. McEwan, M.B. Haeri, T.O. Clatterbuck, J. McCartney, H. Bookey, A.K. Kar, *[To be submitted to J. Appl. Phys.]*

"Optimisation of high average power optical parametric generation using a photonic crystal fiber", T.J. Sloanes, K.J. McEwan, L. Michaille, B. Lowans. *Opt. Express.* **16** 19724-19733 (2008)

"Optimisation of high power four-wave mixing in a photonic crystal fibre", T.J. Sloanes, K.J. McEwan, L. Michaille, *[Oral Presentation at Photon06, Manchester, 2006]*

"Measurements of Optical Nonlinearities in Indium Phosphide", T.J. Sloanes, K.J. McEwan, P.K. Milsom *[Poster presentation at QEP-17, Manchester, 2006]*

"Four-wave mixing and supercontinuum generation with picosecond pulses in photonic crystal fibres", T.J. Sloanes, K.J. McEwan *[DSTL internal report]*

1 Introduction 1

1.1 Nonlinear behaviour 3
1.2 Optical nonlinearities 4
1.3 Indium phosphide 6
1.4 Cadmium mercury telluride 8
1.5 Photonic crystal fibres 10
1.6 Thesis layout 11
1.7 References 12

2 Modelling the Nonlinear Response of the Material 15

2.1 Introduction to two-photon absorption, free carrier absorption and nonlinear refraction 17
  2.1.1 Nonlinear behaviour in semiconductors 18
  2.1.2 Two-photon absorption and resulting refractive effects 19
  2.1.3 Free-carrier absorption and refraction 23
  2.1.4 Total contributions to absorption and refraction 28
2.2 Nonlinearity measurement techniques 29
  2.2.1 Z-Scan technique 29
  2.2.2 Pump-probe experiment 31
2.3 Mathematical models 32
  2.3.1 Femtosecond pulses 32
  2.3.2 Nanosecond pulses 34
2.4 References 40

3 Femtosecond Measurements on Indium Phosphide 41

3.1 Introduction 43
3.2 Isolating the two-photon absorption coefficient 44
3.3 Initial experimental procedure and results 48
  3.3.1 Experimental description 48
  3.3.2 Experimental results 49
3.4 Conclusions 55
3.5 References 56

4 Nanosecond Measurements on Indium Phosphide 57

4.1 Introduction 59
4.2 Beam and material characterisation 60
  4.2.1 Measurement of 1.064μm beam waist and M^2-value 60
  4.2.2 Measurement of 1.534μm beam waist and M^2-value 65
  4.2.3 Indium phosphide characterisation 67
4.3 Free-carrier lifetime measurements 70
  4.3.1 Experimental procedure 70

4.3.2 Pump-probe experimental results 72
4.4 1.064μm and 1.534μm z-scan description and results 74
4.4.1 Experimental procedure for 1.064μm z-scans 74
4.4.2 Results of 1.064μm z-scans 76
4.4.3 Experimental procedure for 1.534μm z-scans 83
4.4.4 Results of 1.534μm z-scans 85
4.5 Conclusions 88
4.6 References 89

5 Nanosecond Measurements in Cadmium Mercury Telluride 91

5.1 Introduction 93
5.2 Beam and material characterisation 94
5.2.1 Beam characterisation 94
5.2.2 Cadmium mercury telluride characterisation 94
5.3 Z-Scan description and results 99
5.3.1 Experimental procedure 99
5.3.2 Results of z-scans on CMT1 (1.4μm band-edge) 100
5.4 Results of z-scans on CMT2 (1.5μm band-edge) 103
5.5 Conclusions 107
5.6 References 108

6 Nonlinearities in Photonic Crystal Fibres 111

6.1 Chapter summary 113
6.2 Introduction 114
6.3 Photonic crystal fibres 116
6.4 Frequency conversion in PCFs 118
6.5 Experimental method 121
6.6 Results 124
6.6.1 Preliminary investigations with 10m fibre 124
6.6.2 Spectral output dependence on input power with 150m fibre 126
6.6.3 Spectral output dependence on fibre length 128
6.6.4 Supercontinuum fibre 131
6.7 Conclusions 133
6.8 References 134

7 Conclusions 141

7.1 Introduction 143
7.2 Measurement of β in indium phosphide 144
7.3 Measurement of σ_{fca} in indium phosphide and cadmium mercury telluride 145
7.4 Measurement of σ_r in indium phosphide and cadmium mercury telluride 146

7.5 Use of the experimentally determined parameters 148
7.6 Further semiconductor work 149
7.7 New frequency generation in photonic crystal fibres 150
7.8 Future photonic crystal fibre work 151
7.9 References 152

1 Introduction

1.1 Nonlinear behaviour

When light travels through a transparent material, it can be so intense that it causes the refractive index of the material to change. Hence, the material properties affecting the transmission can be dependent upon the light intensity. This is an example of nonlinear behaviour.

I aim to measure some of the optical nonlinearities that occur in semiconductor materials. Specifically, I will be investigating two-photon absorption and free-carrier absorption and refraction in samples of indium phosphide (InP) and cadmium mercury telluride, (CdHgTe or CMT).

Two-photon absorption occurs when two photons are absorbed by the material liberating a single electron-hole pair. This occurs via a short-lived virtual state. For a reasonable chance of it occurring, high intensity radiation is required, so that many photons are present in a small area. The free-carriers generated by the two-photon absorption can then absorb and refract the beam. I intend to measure the parameters that determine each of these nonlinear processes in this thesis.

I also present an investigation into supercontinuum generation and four-wave mixing in a photonic crystal fibre, which is a fibre designed with an array of holes running down its length. A supercontinuum is a broad spectrum of light, similar to the light from a light bulb, but not necessarily at visible wavelengths. In the experiments described in this thesis, the supercontinuum is generated by injecting a monochromatic laser into a photonic crystal fibre. The optical nonlinearities present in the fibre core cause the beam to spread spectrally. Four-wave mixing is also observed and used in the fibre to generate light at new wavelengths. This is a nonlinear process whereby light from two sources combine to produce light at new wavelengths.

This chapter is intended to be an introduction to my thesis. Section 1.1 contains an overview of optical nonlinearity measurements in semiconductors. Sections 1.2 and 1.3 contain information on the indium phosphide and cadmium mercury telluride materials used in the experiments in later chapters. Section 1.4 has an overview of the photonic crystal fibre experiments. Finally, section 1.5 describes the layout of my thesis.

1.2 Optical nonlinearities

The development of the laser in 1960 provided the tool that would allow a variety of optical nonlinearities to be observed and measured, due to the requirement for high optical intensities. Two photon absorption (TPA) in a semiconductor was first observed in 1964[1] in cadmium sulphide and since then, many different semiconductor materials have been studied. See, for example, the works of Miller et al.[2] and Van Stryland et al.[3].

In addition to the TPA, large refractive nonlinearities can occur due to free-carriers generated in the material. These were first reported at bandgap resonant wavelengths by Miller et al.[4]. In this thesis TPA is used as the excitation source for generating the free-carriers which produce the refractive (and absorptive) nonlinearities, as demonstrated by Kar et al.[5] in indium antimonide.

A diagrammatic summary of the various nonlinear processes is displayed in fig. 1.1. As well as the nonlinearities discussed above, a few other phenomena are displayed and must be considered. Linear absorption can generally be ignored, as it is primarily TPA that is being investigated, so the laser has been chosen such that its photon energy is sub-bandgap to the material under investigation. However, in cases where the laser photon energy is above the bandgap, this can be a much more efficient carrier generation process than two-photon absorption. Some of the experiments in chapter 5 take advantage of this fact to demonstrate enhanced nonlinear effects.

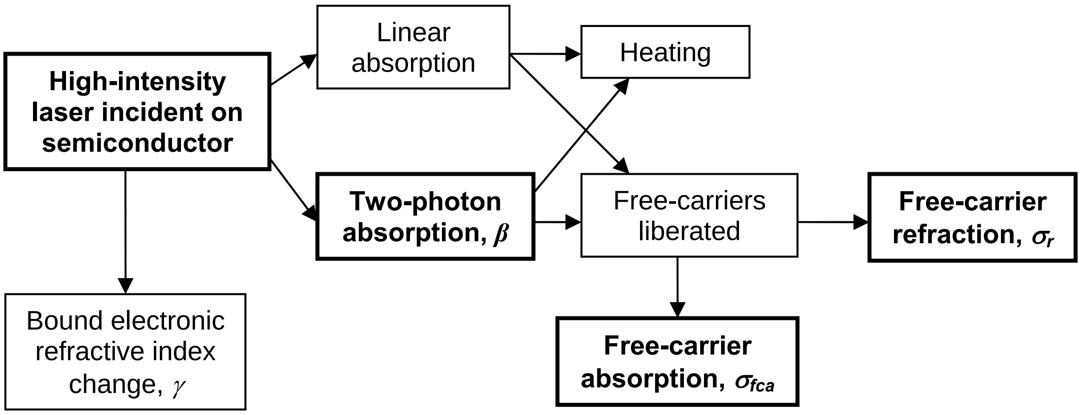
High-intensity laser incident on semiconductor
Linear absorption
Heating
Two-photon absorption, β
Free-carriers liberated
Free-carrier refraction, σ_r
Bound electronic refractive index change, γ
Free-carrier absorption, σ_{fca}

Figure 1.1: Summary of the important optical effects of a high intensity laser beam hitting a semiconductor.

Both linear and two-photon absorption can cause heating of the material. This causes the lattice to expand which changes the bandgap. This in turn can affect the two-photon absorption coefficient and the refractive index of the material. However, for low-pulse energies this is generally small and can be neglected.

The final nonlinearity to consider is the bound electronic refractive index change, which occurs at high intensities when the electric fields approach that of the inter-atomic electric fields. This has been observed and measured in a number of semiconductors[6,7], but is shown to be negligible in the experiments in this thesis (see chapter 3). All of the above processes are described in more detail in chapter 2.

In 1991 the z-scan technique[8] was developed, allowing sensitive measurements of optical nonlinearities to be made via a simple transmission experiment. Since then, many investigations have been made on a huge variety of materials, ranging from semiconductors[9], to synthesised organic compounds[10], to tea[11]. The work in this thesis is concerned with performing z-scans on indium phosphide and cadmium mercury telluride, and more information on these two semiconductors is provided in sections 1.3 and 1.4.

1.3 Indium phosphide

Indium phosphide was first prepared in 1910 by A.Thiel and H.Koelsch[12]. It is a binary semiconductor consisting of alternating indium (In) and phosphorus (P) atoms in a zincblende crystal structure (see fig. 1.2). The indium and phosphorus atoms sit in two face-centred cubic arrangements offset from each other by a quarter body diagonal.

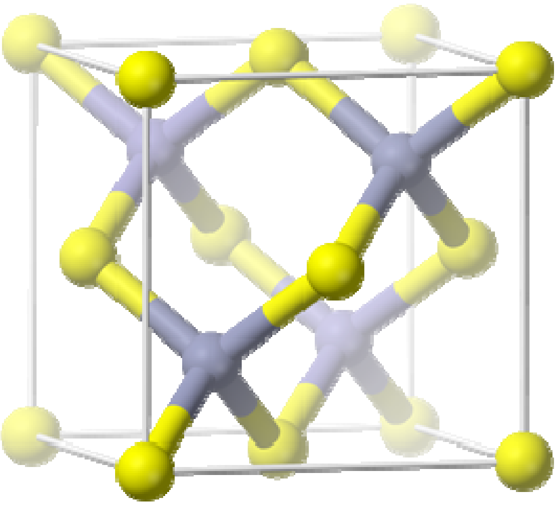

Figure 1.2: Diagram showing the zincblende crystal structure (image obtained from the public domain).

Indium is in group 13 (formerly III) and phosphorus is in group 15 (formerly V) of the periodic table. Hence, indium phosphide is known as a III-V semiconductor.

Since the 1980s, much work has been done on developing the material, mainly for use in the electronics industry. The relatively high electron and hole mobility facilitate the operation of very high speed electronics, and high-speed bipolar transistors based on InP are becoming more common in high-frequency applications[13]. Indium phosphide is also used as a substrate layer for the InGaAs and InGaP family of materials, which are used in photodetectors, as it shares the same lattice parameter. This means that high optical-quality material is readily available.

Considering how common the use of indium phosphide is and the availability of the material, it is surprising that there is little information on its nonlinear coefficients available in the literature. The most recent measurement of the TPA coefficient is that of Tiedje et al.[14], who report a value of 70cm/GW at 1.305μm using a pump-probe technique. Previous to that, Vignaud et al.[15] report the value ranging from 24cm/GW to 33cm/GW at 1.6μm. This again uses a pump-probe technique. Dvorak and Justus[16] used the z-scan technique to measure a TPA coefficient of 90cm/GW at 1.064μm. Measurements before this tend to be larger. Bendorius and Maltudis[17] report a value of 1800cm/GW whilst Lee and Fan[18,19] report values ranging from 180cm/GW to 260cm/GW, depending on carrier density, at 1.060μm.

The value I measure, 45cm/GW, is almost twice the value calculated from theory of 25cm/GW. However it is closer than some of the relatively recent measurements.

It is evident that there is a large scatter in the reported values measured experimentally. The tendency has been for the measured value to decrease as time has gone on, approaching that of theoretical estimates, probably due to improvements in experimental techniques. Due to the scatter, it is important to continue measurements until a consistent value can be ascertained.

There is less information regarding the free-carrier absorption coefficient and free-carrier refractive index cross-section. The only reported experimental value is that of Dvorak and Justus[16], who measure a free-carrier refractive cross-section of $-0.4\times10^{-21}\text{cm}^3$. This is at least an order of magnitude lower than predicted from theory. Therefore, it is important that this value be measured to see where the discrepancy lies.

1.4 Cadmium mercury telluride

Cadmium mercury telluride was first developed as a semiconducting material 50 years ago by William Lawson[20]. It is a ternary semiconductor alloy containing cadmium (Cd), mercury (Hg) and tellurium (Te) atoms in a Wurtzite crystal structure (see fig. 1.3), which is an example of a hexagonal crystal structure. Cd and Hg are transition elements found in group 12 (previously IIB) whilst Te is a metalloid found in group 16 (previously VIB). Its chemical formula is $Cd_xHg_{(1-x)}Te$ but it is often referred to as CMT (or MCT) for simplicity. The x denotes the molar fraction of cadmium present in the alloy. By varying this quantity, the bandgap of the material can be altered from -0.3eV, in the case of $x = 0$ (HgTe, which is a semimetal), to 1.56eV (0.79μm) in the case of $x = 1$ (CdTe). Cadmium and mercury have very different physical properties, for example mercury is a liquid at room temperature whilst cadmium is a solid. This makes it a difficult material to manufacture and process. It is also quite soft and fragile, so handling is difficult.

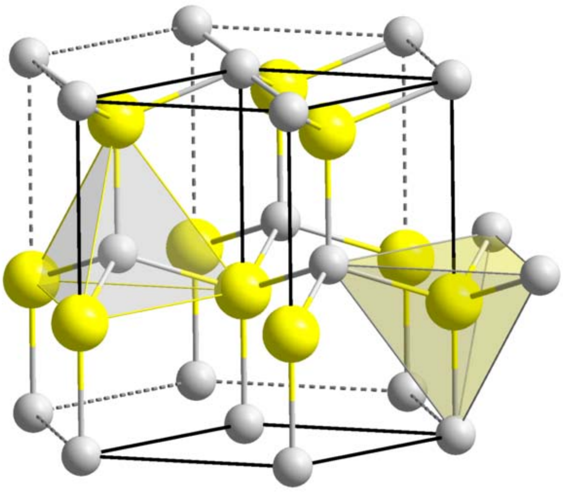

Figure 1.3: Diagram showing the wurtzite crystal structure (image obtained from the public domain).

The main area of application of CMT is in infra-red sensors in the mid- and long-wavebands (3-5μm and 10-12μm respectively). To produce material with appropriate bandgaps requires low x values ($x = 0.16$-0.18 and $x = 0.27$-0.39 respectively). Therefore most of the information reported in the literature is for CMT with these compositions. The material used in this thesis is unusual in that it has been designed for nonlinear absorption at 1.5μm so has a much higher *x* value (0.65-0.7, to be shown in chapter 5). Reference 21 contains a description of the growth technique of this high *x*-value material.

Whilst measurements of optical nonlinearities exist in the literature[2,22-24], there are none for material compositions similar to the ones used in the experiments in this thesis. Therefore measurement of the various optical nonlinearities should provide interesting results, relevant at short-wave infra-red wavelengths. An additional motivation is that nonlinear absorption may be stronger in CMT than other semiconductor materials, as suggested by Krishnamurthy et al[25], who calculate the nonlinear absorption in CMT to be twice as large as a similar sample of InAs having the same bandgap and thickness.

1.5 Photonic crystal fibres

Photonic crystal fibres (PCFs) are a relatively recent invention, first reported in 1996[26]. They are similar in concept to a standard optical fibre in that a core is surrounded by cladding material of a different refractive index, which causes light to be totally-internally reflected at the core-cladding boundary. The light is therefore guided down the core. The difference in PCFs is that the cladding is made up of an array of air-filled holes, rather than doped silica, say. This creates a large refractive index change resulting in light being strongly confined to the solid-core region. By tailoring the structure of the cladding, the zero group velocity dispersion (ZGVD) point of the fibre – that is the point at which a light pulse will propagate down the fibre without spreading temporally –can be altered. Although the nonlinear coefficients of silica are small, nonlinear processes can still be efficient due to the long interaction lengths and high radiation intensities in the core.

In the experiments in chapter 7, a photonic crystal fibre with its ZGVD at 1.040μm is pumped with picosecond pulses of 1.064μm radiation from a $Nd:YV0_4$ laser with the intention of generating new frequencies through nonlinear conversion. Normally, femtosecond pulses are used as they offer higher intensities so the nonlinear processes occur more strongly. However, by using picosecond pulses, a much higher average output power can be obtained. Through a combination of Raman shifting and soliton self-frequency shifting, a relatively flat supercontinuum is generated between ~1.1 and 1.4μm. This was later used in an experiment looking at the spectral returns of various pieces of optical equipment.

Four-wave mixing was also used in the same fibre to generate light at 0.9μm and 1.3μm at a power transfer efficiency of 14% and 9% respectively.

1.6 Thesis layout

Following the references at the end of this introductory chapter, chapter 2 contains a discussion of the general theory behind two-photon absorption and free-carrier absorption and refraction in semiconductors. There is also a description of the mathematical models used to generate fits to the experimental data, allowing the nonlinear parameters to be extracted from the experimental results. Chapter 3 describes the experiments using femtosecond pulses to measure the two-photon absorption coefficient in InP. Chapter 4 describes the measurement of the free-carrier nonlinearities in InP at 1.064μm and 1.534μm using nanosecond pulses. The details of similar measurements on two samples of cadmium mercury telluride at 1.534μm are described in chapter 5. Chapter 6 offers a change of subject, and is an account of the investigation into four-wave mixing and supercontinuum generation in a photonic crystal fibre. The final chapter, chapter 7, contains a summary and discussion of the results from the previous chapters.

1.7 References

1. R. Braunstein, N. Ockman, “Optical double-photon absorption in CdS” *Phys. Rev.* **134** pA499 (1964)
2. A. Miller, A. Johnston, J. Dempsey, J. Smith, C.R. Pidgeon, G.D. Holah, “Two-photon absorption in InSb and $Hg_{1-x}Cd_xTe$” *J. Phys. C.* **12** p4839 (1979)
3. E.W. Van Stryland, H. Vanherzeele, M.A. Woodhall, M.J. Soileau, A.L. Smirl, S. Guha, T.F. Boggess, “Two photon absorption, nonlinear refraction, and optical limiting in semiconductors” *Opt. Eng.* **24** p613 (1985)
4. D.A.B. Miller, M.H. Mozolowski, A. Miller, S.D. Smith “Non-linear optical effects in InSb with a c.w. CO laser” *Opt. Comm.* **27** p133 (1978)
5. A.K. Kar, J.G.H. Mathew, S.D. Smith, B. Davis, W. Prettl, “Optical bistability in InSb at room temperature with two-photon excitation” *Appl. Phys.Lett.* **42** p334 (1983)
6. R. Adair, L.L. Chase, S.A. Payne, “Nonlinear refractive index of optical crystals” *Phys. Rev. B* **39** p3337 (1989)
7. M. Sheik-Bahae, D.C. Hutchings, D.J. Hagen, E.W. Van Stryland, “Dispersion of bound electronic refraction in solids” *J. Quant. Elec.* **27** p1296 (1991)
8. M. Sheik-Bahae, A.A. Said, T.H. Wei, D. J. Hagen, E.W. Van Stryland, “Sensitive Measurement of optical nonlinearities using a single beam” *J. Quant. Elec.* **26** p760 (1990)
9. A.A. Said, M. Sheik-Bahae, D.J. Hagen, T.H. Wei, J. Wang, J. Young, E.W. Van Stryland, “Determination of bound-electronic and free-carrier nonlinearities in ZnSe, GaAs, CdTe and ZnTe” *J. Opt. Soc. Am. B* **9** p405 (1992)
10. S.J. Chung, T.C. Lin, K.S. Kim, G.S. He, J. Swiatkiewicz, P.N. Prasad, G.A. Baker, F.V. Bright, “Two-photon absorption and excited-state energy-transfer properties of a new multibranched molecule” *Chem. Mater.* **13** p4071 (2001)
11. Y.F. Zhang, T. Miyoshi, N. Matsuo, “Time-resolved Z-scan transmittance of Chinese tea” *J. Luminescence* **72** p557 (1997)
12. A. Thiel, H. Koelsch, “Studien über das Indium” Z. Anorg. Chem. **66** p288 (1910)
13. http://spectrum.ieee.org/archive/1593 (2008)
14. H.F. Tiedje, H.K. Haugen, J.S. Preston “Measurement of nonlinear absorption coefficients in GaAs, InP and Si by an optical pump THz probe technique” *Opt. Comm.* **274** p187 (2007)

15. D. Vignaud, J.F. Lampin, F. Mollot, “Two-photon absorption in InP substrates in the 1.55μm range” *Appl. Phys. Lett.* **85** p239 (2004)
16. M.D. Dvorak, B.L.Justus, “Z-scan studies of nonlinear absorption and refraction in bulk, undoped InP” *Optics comms.*, **114** p147 (1995)
17. R.A. Bendorius, E.K. Maldutis, “Nonlinear absorption of laser radiation in InP and GaAs” *Soviet-Phys. Coll.* **23** p69 (1983)
18. C.C. Fan, H.Y. Fan, “Two-Photon Absorption and Photoconductivity in GaAs and InP” *Appl. Phys. Lett.*. **20** p18 (1972)
19. C.C. Fan, H.Y. Fan, “Two-photon absorption with exciton effect for degenerate valence bands” *Phys. Rev. B* **9** p3502 (1974)
20. W.D. Lawson, S. Nielsen, E.H. Putley, A.S. Young, “Preparation and properties of HgTe and mixed crystals of HgTe-CdTe” *J. Phys. Chem. Solids* **19** p325 (1959)
21. P. Capper, C. Maxey, C. Butler, M, Grist, J. Price, “Bulk-growth of near-IR cadmium mercury telluride (CMT)” *J. Mater. Sci. - Mater. Electron.* **15** p271 (2004)
22. D. Craig, A. Miller, “Room temperature optical nonlinearities in CdHgTe” *Optica Acta.* **33** p397 (1985)
23. J.G.H. Mathew, D. Craig, A. Miller, “Optical switching in a CdHgTe étalon at room temperature” *Appl. Phys. Lett.* **46** p128 (1985)
24. D. Craig, A.K. Kar, J.G.H. Mathew, A. Miller, “Two Photon Induced Optical Bistability in CdHgTe at Room Temperature” *J. Quantum. Electron.* **QE-21** p1363 (1985)
25. S. Krishnamurthy, A. Cher, A.B. Chen, “Below band-gap optical absorption in semiconductor alloys” *J. Appl. Phys.* **88** p260 (2000)
26. JC Knight, TA Birks, P St J Russell, DB Atkin, “All-silica single mode optical fiber with photonic crystal cladding”, *Opt. Lett.*, **21** (19) 1547-1549 (1996); Errata, *Opt Lett.*, **22** (7) 484-485 (1997)

2 Modelling the Nonlinear Response of the Material

2.1 Introduction to two-photon absorption, free carrier absorption and nonlinear refraction

As the name suggests, two-photon absorption occurs in a semiconductor when two photons are absorbed simultaneously via a virtual state, promoting an electron from the valence band into the conduction band. For this process to occur, two conditions are required: the photon energies must lie between half the bandgap energy and the bandgap energy, and the light must be of high intensity.

As well as this nonlinear absorption, nonlinear refractive effects can occur. The high intensity radiation can cause charges to move, polarising the material. This results in a refractive index change within the material via the change in susceptibility. This intensity-dependent refractive index change is called the optical Kerr effect.

The free carriers produced by the two-photon absorption (or linear absorption, for that matter) also give rise to absorptive and refractive effects. Generally, in semiconductors, these free-carrier nonlinearities have a greater effect than the processes that produced them, as they have larger cross-sections. For this reason, these types of materials are sometimes referred to as excited-state absorbers.

In recent years, the measurement of nonlinearities in semiconductors has been led by Van Stryland and co-workers[1]. In 1991 Said *et al.* measured the two-photon absorption of a number of different semiconductors[2]. They found that their results agreed well with simple two-band, band-filling models. This allows the nonlinear response of a semiconductor material to be predicted reasonably well knowing only a few material parameters – the bandgap energy, the linear refractive index and the photon energy. This is despite the complexity of the nonlinear processes and their interactions.

Two semiconductor materials will be investigated in the thesis: indium phosphide (InP) and cadmium-mercury telluride (CMT). According to one recent report[3], InP has a larger two-photon absorption coefficient ($\beta\approx 90$cm/GW) than predicted by the above model. This makes it an interesting material to study. CMT is of interest because its bandgap can be varied by changing the proportion of cadmium and mercury. The CMT samples studied in these experiments have a relatively large bandgap, and there appear to be no reported studies on the nonlinear performance at these bandgaps.

This chapter describes the theory used to explain the nonlinearities being measured. Descriptions of the measurement techniques used are given, along with explanations of the mathematical models used to generate theoretical data. Sections 2.1.1-2.1.4 explain the various optical nonlinearities in detail. Section 2.2 describes the experimental techniques used later in the thesis. Section 2.3 describes the mathematical models used to generate fits to the experimental data, allowing extraction of the nonlinear coefficients. Finally, a list of references is given in section 2.4.

2.1.1 Nonlinear behaviour in semiconductors

The nonlinear effects expected to be observed are two-photon absorption, the optical Kerr effect, free-carrier absorption and free-carrier refraction. These are 3rd order and 3rd order-induced 1st order behaviours, and are described below.

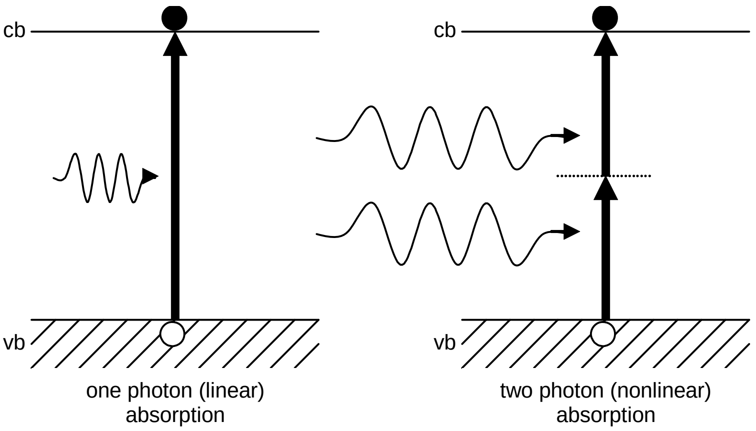
cb
vb
one photon (linear) absorption
cb
vb
two photon (nonlinear) absorption

Figure 2.1: Diagram showing linear and nonlinear absorption of photons in a semiconductor, resulting in generation of electrons and holes (free-carriers).

Due to the gap between energy-bands in a semiconductor, photons can be absorbed creating an electron-hole pair (fig.2.1). When one photon is absorbed to create an electron-hole pair, it is known as linear absorption because the absorption is described by equations that are linear in light intensity. If more than one photon is absorbed to create the electron-hole pair, it is known as multiphoton, or nonlinear, absorption. Nonlinear behaviour is described by equations that depend on the square or cube etc. of the light intensity. Physically, this means that harmonics of the radiation are causing the behaviour. Nonlinear absorption only occurs where there are large numbers of photons present in a short period of time. Therefore, high intensity lasers are required. This is because two (or more) photons must be incident on the same atom (or molecule) simultaneously. In general, only 2nd or 3rd order nonlinear behaviour is observed, as the strength of the optical field required to view the behaviour increases with the order of the effect. At orders higher than 3, the fields required are generally extremely large, so these effects are rarely observed. Therefore, the most common nonlinear absorption observed is when just two photons are absorbed simultaneously. Conceptually, the process occurs via an intermediate virtual state, and is known as two-photon absorption (TPA)[4].

The beam intensities required to initiate two-photon absorption are so high that refraction of the laser beam can occur due to the optical Kerr effect. Additionally, free-carriers are generated that further absorb and refract the beam. The generated free-carriers can have a larger absorption cross-section than the initial two-photon absorption so can absorb the beam more strongly.

2.1.2 Two-photon absorption and resulting refractive effects

The high-intensity radiation required for two-photon absorption to occur causes the distribution of electrons in the material's atoms to change, resulting in the material becoming polarised. When the electromagnetic field is small, the induced polarisation of the medium, $\boldsymbol{P}$, is approximately linearly proportional to the electric field, $\boldsymbol{E}$:

$$\boldsymbol{P} = \varepsilon_0 \chi \boldsymbol{E} \tag{1}$$

where ε_0 is the permittivity of free space and χ is the electric susceptibility tensor.

At high electric field magnitudes, the field approaches that of the intermolecular fields (of the order of 10^5V/m). This causes the polarisation to have a nonlinear dependence on the electric field, which can be expressed as a power series:

$$\boldsymbol{P} = \sum_n \varepsilon_0 \chi^{(n)} \boldsymbol{E}^n \tag{2}$$

Ignoring terms greater than 3rd order, this simplifies to:

$$\boldsymbol{P} = \varepsilon_0\left[\chi^{(1)}\boldsymbol{E} + \chi^{(2)}\boldsymbol{E}^{2} + \chi^{(3)}\boldsymbol{E}^{3}\right] \tag{3}$$

Each of the different terms in eq. (3) has a different physical effect:

$\chi^{(1)}$ is the linear susceptibility tensor and determines linear absorption and refraction. $\chi^{(2)}$ is the first nonlinear term but is only observable in non-centrosymmetric materials (i.e. ones that have no inversion symmetry), where it produces the Pockels effect. It is also responsible for nonlinear frequency mixing e.g. sum and difference frequency mixing. In centrosymmetric materials the induced polarisations cancel each other out. $\chi^{(3)}$ produces third-order effects and is responsible for two-photon absorption and the optical Kerr effect.

Frequency doubling and subsequent linear absorption is possible but is ignored in this thesis and by almost all researchers that study two-photon absorption. Therefore, the $\chi^{(2)}$ term has been neglected. Using this fact, equation (3) can be simplified further to:

$$\boldsymbol{P} = \varepsilon_0\left[\chi^{(1)} + \chi^{(3)}\boldsymbol{E}^2\right]\boldsymbol{E} \tag{4}$$

i.e.

$$\boldsymbol{P} = \varepsilon_0\chi\boldsymbol{E} \tag{5}$$

where

$$\chi = \chi^{(1)} + \chi^{(3)}\boldsymbol{E}^2 \tag{6}$$

χ is related to the total refractive index, n, by

$$n = \sqrt{1+\chi} \tag{7}$$

Similarly, n_0, the linear refractive index, can be defined as:

$$n_0 = \sqrt{1+\chi^{(1)}} \tag{8}$$

Combining eqs. (6-8) gives

$$n = n_0\sqrt{1+\frac{\chi^{(3)}\boldsymbol{E}^2}{n_0^2}} \tag{9}$$

Using the Taylor expansion for small $\chi^{(3)}$ this simplifies to:

$$n \approx n_0 + \frac{\chi^{(3)}}{2n_0}\boldsymbol{E}^2 \tag{10}$$

The optical intensity, *I*, can be related to the electric field amplitude, ***E***, via

$$I = \frac{1}{2}n_0 c\varepsilon_0\left|\boldsymbol{E}^2\right| \tag{11}$$

Hence,

$$n = n_0 + n_2 I \tag{12}$$

where

$$n_2 = \frac{\chi^{(3)}}{n_0^2 c\varepsilon_0} \tag{13}$$

Therefore, a third order nonlinearity gives rise to an intensity-dependent refractive index. This is the optical Kerr effect and n_2 is called the nonlinear refractive index.

$\chi^{(3)}$ can be considered to be complex. Therefore,

$$\chi^{(3)} = \chi_R^{(3)} + i\chi_I^{(3)} \tag{14}$$

The imaginary component is related to β via[5]

$$\chi_I^{(3)} = \frac{n_0^2 \varepsilon_0 c^2}{\omega} \beta \tag{15}$$

and the real component related to the constant γ via[2,5]

$$\chi_R^{(3)} = 2 n_0^2 \varepsilon_0 c \gamma \tag{16}$$

In SI units, the coefficient n_2 has the value γ where

$$\gamma = n_2 \left(\frac{40\pi}{c n_0} \right) \tag{17}$$

Then the refractive index change due to the optical Kerr effect at intensity I is given by:

$$\Delta n = n_2 I \tag{18}$$

Although an expression for β is given above, a more convenient way of estimating β, which is dependent only on the linear refractive index, n_0, and the energy gap of the material, E_g, was proposed by Van Stryland et al.[6]:

$$\beta(2\omega') = K \frac{\sqrt{E_p}}{n_0^2 E_g^3} F_2 \left(\frac{2\hbar\omega'}{E_g} \right) \tag{19}$$

where K is a material-independent constant having a value of 3.1×10^3 (in units such that E_p and E_g are in eV, and β is in cm/GW[6]). E_p, which is related to the Kane momentum parameter, is nearly material independent and possesses a value of ~21eV for most direct-gap semiconductors. It should be noted that this value is larger than that used later. This is consistent with the original authors' observations. F_2 is a function of the form:

$$F_2(x) = \frac{(x-1)^{3/2}}{(x)^5} \tag{20}$$

The effects described above are not the only sources of absorption and refraction, as the free carriers produced can also absorb and refract the beam. These processes are described in the next section.

2.1.3 Free-carrier absorption and refraction

When nonlinear absorption occurs free carriers are generated. These too can absorb and refract the laser beam. These processes are described by the free carrier absorption cross-section, σ_{fca}, and the refractive index cross-section, σ_r.

The number of carriers generated per unit volume per second is given by:

$$\frac{dN(t)}{dt} = \frac{\beta I(t)^2}{2\hbar\omega} - \frac{N(t)}{\tau_r} \tag{21}$$

where τ_r is the free-carrier recombination time. This equation can be integrated to give:

$$N(t) = \int_{-\infty}^{t} \frac{\beta dt'}{2\hbar\omega}\left[I_{in}^2(t')\right] e^{\frac{-(t-t')}{\tau}} \tag{22}$$

The intensity change due to free-carrier absorption is:

$$\frac{dI(t)}{dz} = -\sigma_{fca} N(t) I(t) \tag{23}$$

where σ_{fca} is the free carrier absorption cross-section.

Combining the two previous equations, the free-carrier absorption is given by:

$$\frac{dI(t)}{dz} = -\sigma_{fca} I_{in}(t) \int_{-\infty}^{t} \frac{\beta dt'}{2\hbar\omega}\left[I_{in}^2(t')\right] e^{\frac{-(t-t')}{\tau}} \tag{24}$$

where $I_{in}(t)$ is the input intensity at time t.

The refractive index cross-section can be estimated to first order using classical Drude theory to relate the relative permittivity, ε, to the linear refractive index, n_0, and the plasma induced refractive index change, Δn, via[7]:

$$(n_0 + \Delta n)^2 = \varepsilon = n_0^2\left(1 - \frac{\omega_p^2}{\omega^2}\right) \tag{25}$$

with the plasma frequency, ω_p, related to the charge carrier density, ΔN, by:

$$\omega_p^2 = \frac{e^2}{m_c \varepsilon_0 n_0^2}\Delta N \tag{26}$$

where m_c is the effective mass of the electron. Using eq. 25 and assuming that the refractive index change is small compared with the linear index gives:

$$n_0^2 + 2n_0\Delta n = n_0^2\left(1 - \frac{e^2}{m_c \varepsilon_0 n_0^2 \omega^2}\Delta N\right) \tag{27}$$

Rearranging gives:

$$\Delta n = \sigma_r \Delta N \tag{28}$$

Where σ_r, the refractive index cross-section, is given by:

$$\sigma_r = -\frac{e^2}{2n_o m_c \varepsilon_0 \omega^2} \tag{29}$$

and where m_c is the reduced mass of the electrons and heavy holes, which is given by

$$m_c = \frac{m_{hh} m_{eff}}{m_{hh} + m_{eff}} \tag{30}$$

An improvement on this formula was suggested by Auston[8]:

$$\sigma_r = -\frac{e^2}{2n_o m_c \varepsilon_0 \omega^2}\left[\frac{1}{1-\left(\frac{\hbar\omega}{E_g}\right)^2}\right] \quad \text{for } \hbar\omega < E_g \tag{31}$$

The equation is semi-empirical, but includes an estimate of the effect of band filling on the absorption and, hence, refraction. Here, $\hbar\omega$ is the photon energy and E_g is the energy gap.

Auston's formula breaks down near resonance so a different formula needs to be used when the photon energy approaches the bandgap energy. Wherrett et al.[7] proposed a model for near-resonant cases. It sums the effects of the individual contributions to the refraction from the electrons and holes.

$$\Delta n = \left(\sigma_{elec}^{tot} + \sigma_{holes}^{tot}\right) n_e^c \tag{32}$$

where

$$\begin{aligned}\sigma_{elec}^{tot} &= -\frac{e^2}{2n_0 m_c \varepsilon_0 \omega^2} * \\ &\left\{1 + \frac{4}{3\sqrt{\pi}}\frac{E_P}{k_B T}\left[\begin{array}{l}\frac{\mu_{c-hh}}{m_e} J_{\text{mod}}\left(\beta\frac{\mu_{c-hh}}{m_c}E_g, \beta\frac{\mu_{c-hh}}{m_c}\hbar\omega\right) \\ +\frac{\mu_{c-lh}}{m_e} J_{\text{mod}}\left(\beta\frac{\mu_{c-lh}}{m_c}E_g, \beta\frac{\mu_{c-lh}}{m_c}\hbar\omega\right)\end{array}\right]\right\}\end{aligned} \tag{33}$$

and

$$\sigma_{holes}^{tot} = -\frac{e^2}{2n_0 m_c \varepsilon_0 \omega^2} * \left\{ \begin{array}{l} \dfrac{m_c}{m_{hh}\left[1+\left(\dfrac{m_{lh}}{m_{hh}}\right)^{\frac{3}{2}}\right]} \left[\begin{array}{l} 1+ \\ \dfrac{4}{3\sqrt{\pi}} \dfrac{E_P}{k_B T} \dfrac{\mu_{c-hh}}{m_e} J_{\text{mod}}\left(\beta \dfrac{\mu_{c-hh}}{m_{hh}} E_g , \beta \dfrac{\mu_{c-hh}}{m_{hh}} \hbar\omega\right) \end{array} \right] \\ + \dfrac{m_c}{m_{hh}\left[1+\left(\dfrac{m_{hh}}{m_{lh}}\right)^{\frac{3}{2}}\right]} \left[\begin{array}{l} 1+ \\ \dfrac{4}{3\sqrt{\pi}} \dfrac{E_P}{k_B T} \dfrac{\mu_{c-lh}}{m_e} J_{\text{mod}}\left(\beta \dfrac{\mu_{c-lh}}{m_{lh}} E_g , \beta \dfrac{\mu_{c-lh}}{m_{lh}} \hbar\omega\right) \end{array} \right] \end{array} \right\} \quad (34)$$

Where $\mu_{c\text{-}hh}$ ($\mu_{c\text{-}lh}$) is the reduced mass associated with the conduction band and the heavy-hole (light-hole) valence band, m_e, m_c, m_{hh} and m_{lh} are the free-electron mass, conduction band electron mass, heavy-hole mass and light-hole mass respectively. $\beta = 1/k_B T$, $E_P \sim$ 11eV (not 21eV, as explained earlier) and the function J_{mod} is defined as:

$$J_{\text{mod}}(E_1, W_1) = -2J(-E_1) + J(-(W_1 + E_1)) + J(W_1 - E_1) \quad (35)$$

where

$$J(a) = \sqrt{\pi} - \sqrt{-a}\,\exp(-a)\pi\,\text{Erfc}\left(\sqrt{-a}\right) \qquad a<0 \quad (36)$$

$$= \sqrt{\pi} - \sqrt{a}\,\exp(-a)\pi\,\text{Erfi}\left(\sqrt{a}\right) \qquad a>0$$

These equations are plotted for indium phosphide in figure 2.2. Table 2.1 shows the parameters used and the σ_r values obtained for all the materials studied in this thesis (see chapters 4 and 5 for details of how the numerical parameters were obtained).

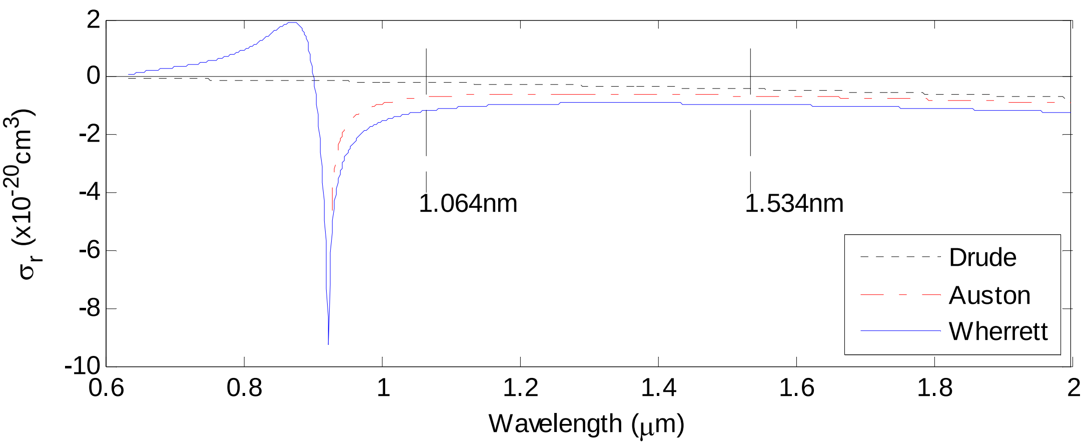

Figure 2.2: Comparison of σ_r value variation with wavelength in InP using Drude, Auston and Wherrett formulae.

Material	InP	InP	CMT1	CMT2
Wavelength (μm)	1.064	1.534	1.534	1.534
x	N/A	N/A	0.683	0.649
E_g**(μm)**	0.92	0.92	1.4	1.5
E_g**(eV)**	1.347	1.347	0.878	0.819
n	3.29	3.17	2.94	3
m_c	0.08	0.08	0.059	0.055
m_{hh}	1.3507	1.3507	0.4	0.4
m_{lh}	0.6	0.089	0.059	0.055
β **(cm/GW)**	22	20	87	91
Auston σ_r **(x10^{-20}cm^3)**	-0.78	-0.65	-4.1	-31
Wherrett σ_r **(x10^{-20}cm^3)**	-1.17	-0.94	-5.3	-14

Table 2.1: Summary of parameters used in the above equations and the results obtained (see chapters 4 and 5 for more details).

The next section combines the nonlinear effects discussed previously into two equations, describing the total nonlinear response of semiconductor materials.

2.1.4 Total contributions to absorption and refraction

Bringing the various absorptive components discussed in the previous sections together and including linear absorption, the total change in intensity with position inside the material is given by:

$$\begin{aligned}\frac{dI(t)}{dz} &= -\alpha I_{in}(t) \\ &\quad -\beta I_{in}^{2}(t) \\ &\quad -\sigma_{fca} I_{in}(t)\int_{-\infty}^{t} \frac{\beta dt'}{2\hbar\omega}\left[I_{in}^{2}(t')\right] e^{\frac{-(t-t')}{\tau}}\end{aligned} \tag{37}$$

where *α* is the linear absorption coefficient which can be small if the thermally generated free-carrier density is negligible.

The total change in refractive index, *Δn*, is given by

$$\Delta n(t) = \sigma_r N(t) + \gamma I(t) \tag{38}$$

For short pulses (e.g. of femtosecond duration), the intensity can be high even though the energy is quite low. This results in few carriers being generated, and *γ* dominates the refractive index change. On the other hand, longer pulses (e.g. nanoseconds) can be of higher energies whilst having low peak intensities. This results in more free-carriers being generated and the free-carrier refractive index change dominates the overall refraction.

The next section describes how these nonlinearities can be measured.

2.2 Nonlinearity measurement techniques

There are a number of different techniques for measuring the optical nonlinearities exhibited by semiconductors. The experiments described in this thesis mostly use z-scans, so most of the emphasis will be put on explaining how they work. Some pump-probe experiments are also done and will be explained too.

2.2.1 Z-Scan technique

The z-scan technique was invented by Van Stryland et al.[5]. It has many advantages over other nonlinearity measurement techniques in that it is very simple to perform, it is fast, gives the sign of the optical nonlinearity immediately in most cases and it is very sensitive.

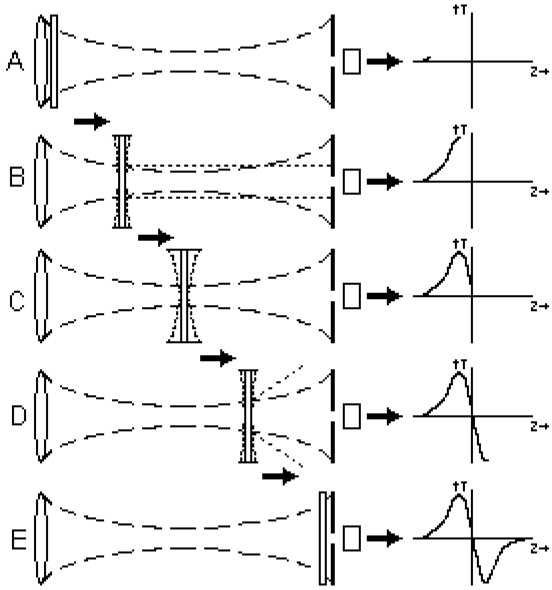

Figure 2.3A-E: Graphical depiction of the z-scan experiment, used for measuring optical nonlinearities.

Figure 2.3 shows a schematic of the procedure used in a z-scan measurement. Consider a lens focussing a Gaussian laser beam. The semiconductor sample is placed in the beam to the left of focus and a partially closed aperture is placed in front of a detector beyond the focus.

Far in front of focus, the intensity of the beam is not strong enough to cause any nonlinear absorption within the sample, so the signal measured on the detector is just the linear absorption (see fig.2.3A). As the sample is brought towards focus, the nonlinear absorption and, hence, the refraction associated with the generated free carriers, increases. The sample therefore acts as a variable lens, which gets stronger the closer it is to focus. Assuming the sign of the refractive index change is negative, so that the sample acts as a concave lens, the beam, which is being focussed by the lens, will be collimated (fig. 2.3B). Therefore slightly more light will pass through the aperture onto the detector, resulting in an increase in the measured signal. At focus (fig. 2.3C) the lensing effect of the sample is at its greatest. However, as the sample is at focus, it has no effect on the beam. As the sample is moved through focus the strength of the refraction decreases due to the lower intensity generating fewer free-carriers (fig. 2.3D). However, the beam is now diverging away from focus and the sample compounds this, resulting in the measured signal reducing to a minimum. Finally, with the sample far beyond focus (fig. 2.3E), the intensity is too weak to initiate nonlinear absorption so the measured signal returns to the linear transmission level.

The peak followed by trough behaviour illustrated above is characteristic of a material with a negative change in refractive index. Conversely, a trough followed by a peak is characteristic of a positive refractive index change.

It is very quick and easy to see the sign of the refractive index change, something not immediately obvious with other measurement techniques. It should be noted that the transmission profile graphs displayed in fig. 2.3 are for an ideal case only, where nonlinear absorption has been neglected. In most practical situations the measured transmission profile will be more complex. Frequently, two-photon and free-carrier absorption will modify the characteristic peak-trough, suppressing the peak and enhancing the trough. This can be quantified by performing a so-called open-aperture experiment, in which the total energy in the transmitted beam is collected. In this case the aperture is opened so that it no longer impinges on the beam (it is essentially removed from the set-up). This arrangement is insensitive to refraction, so only two-photon and free-carrier absorption is measured. The resulting transmission curve has a trough centred on the beam focus, where the absorption in the sample is strongest. By dividing a closed-aperture scan by an open-aperture scan, the effect of the free-carrier absorption can be removed[2,5], giving only the effect of the nonlinear refraction.

2.2.2 Pump-probe experiment

Pump-probe experiments on a material enable the carrier recombination rate to be measured. Various techniques exist, but the basic premise is the same for each. The material is initially excited using a pulse of light. The material is then probed using either a different laser or a separate pulse from the pump laser. If the same laser is used then generally a pulse from it will be delayed in time with respect to the pump pulse. The transmission of the probe pulse is then measured. If a continuous wave (cw) probe laser is used (see fig.2.4), the number of carriers generated by the pump pulse will change throughout the duration of the probe period, as they recombine. This affects the transmission of the sample, so a picture of the free carrier recombination can be built up by monitoring the transmission over time.

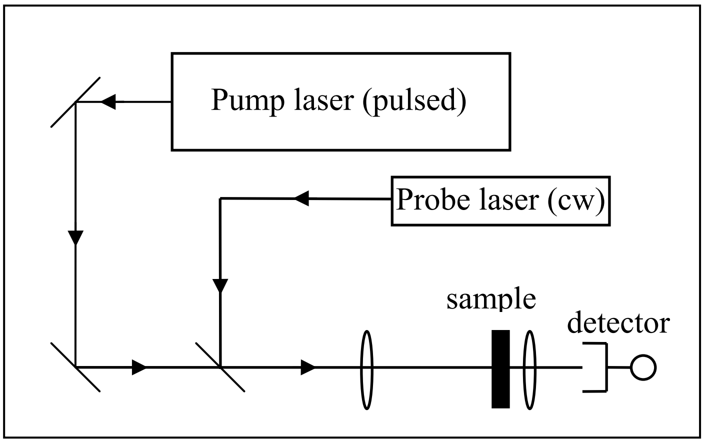

Figure 2.4: Example experimental set up for pump probe measurement.

2.3 Mathematical models

Mathematical models were written to allow the extraction of the nonlinear parameters of interest (the two-photon absorption coefficient, β, the nonlinear refractive index cross-section, σ_r, and the free-carrier absorption coefficient, σ_{fca},) from the experimental data. Using estimates of the nonlinear parameters, theoretical z-scan curves were generated. The estimates of the nonlinear parameters were then refined until the theoretical data produced by the model was a close-match to the experimental data.

Three different models were written. One was used for the femtosecond pulse measurements and the other two were used for the open and closed aperture z-scans performed with nanosecond pulses.

2.3.1 Femtosecond pulses

Assuming that linear and free-carrier absorption is negligible (due to the photon energy being sub-bandgap and using femtosecond pulses, respectively), eq. 37 reduces to:

$$\frac{dI(t)}{dz} = -\beta^2 I_{in}(t) \tag{39}$$

This can be solved[2] to give the transmission of a Gaussian beam through a sample of thickness L:

$$T(z) = \frac{1}{\pi^{1/2} q(0,0,z)} \int_{-\infty}^{\infty} \ln\left[1 + q(0,0,z)\exp\left(-\tau^2\right)\right] d\tau \tag{40}$$

Where

$$q(r,t,z) = \beta I(0,r,t,z) L_{eff} \tag{41}$$

$$I(0,r,t,z) = \frac{I_0 \exp\left[-2(r/\omega_0)^2 - (t/t_0)^2\right]}{1 + (z/z_0)^2} \tag{42}$$

$$L_{eff} = \left[1 - \exp\left(-\alpha_0 L\right)\right] / \alpha_0 \qquad (43)$$

and z is the sample position, $T(z)$ is the transmission when the sample is at position z, α_0 is the linear absorption coefficient and the other parameters are from standard Gaussian optics.

The fitting program works via a graphical user interface, which allows the various experimental parameters to be altered. The effect of a parameter change can be seen immediately. The convenience of this produces more accurate fits to the experimental data because more parameter combinations can be tested in a shorter period of time.

Figure 2.5 shows a screenshot of the fitting program. Best estimates of the parameters were inserted into the relevant boxes then they were altered via the sliders until a good fit was obtained.

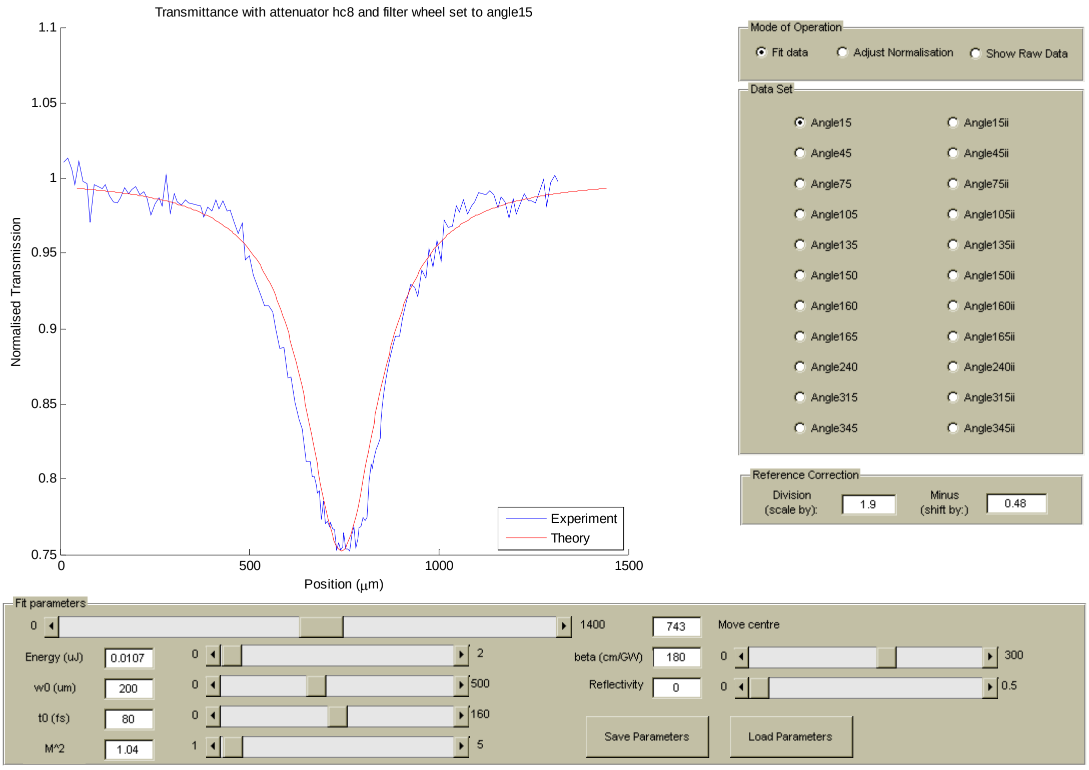
Transmittance with attenuator hc8 and filter wheel set to angle15
Normalised Transmission
1.1
1.05
1
0.95
0.9
0.85
0.8
0.75
0
500
1000
1500
Position (μm)
Experiment
Theory

Mode of Operation

● Fit data ○ Adjust Normalisation ○ Show Raw Data

Data Set

● Angle15 ○ Angle15ii
○ Angle45 ○ Angle45ii
○ Angle75 ○ Angle75ii
○ Angle105 ○ Angle105ii
○ Angle135 ○ Angle135ii
○ Angle150 ○ Angle150ii
○ Angle160 ○ Angle160ii
○ Angle165 ○ Angle165ii
○ Angle240 ○ Angle240ii
○ Angle315 ○ Angle315ii
○ Angle345 ○ Angle345ii

Reference Correction

Division (scale by): 1.9
Minus (shift by:) 0.48

Fit parameters

0 – 1400: 743 Move centre
Energy (uJ): 0.0107 (0 – 2)
w0 (um): 200 (0 – 500)
t0 (fs): 80 (0 – 160)
M^2: 1.04 (1 – 5)
beta (cm/GW): 180 (0 – 300)
Reflectivity: 0 (0 – 0.5)

Save Parameters
Load Parameters

Figure 2.5: Fitting program graphical user interface and example of a fit to the experimental InP data.

2.3.2 Nanosecond pulses

Modelling the nanosecond experiments was more complicated than the femtosecond case, as the nonlinear effects of the free carriers have to be included. Two programs were written in Matlab – one to consider the case when the total energy was collected (an open z-scan), the other to model the energy transmitted through an aperture (a closed z-scan).

Modelling an open z-scan:

In an open-aperture z-scan, the sample is translated through the focus of a laser beam along the direction of propagation. The transmitted energy is measured as the sample is moved to each new position.

In order to model this, the sample is split up into slices of thickness *dL*. The intensity of the beam entering the first slice is known, as is the effect of the material on the beam. Therefore, the intensity at the exit face of the slice can be calculated. This is then used to calculate the intensity entering the next slice. This process continues until the entire sample has been traversed by the beam, and the energy transmitted by the sample determined. The sample is then moved to its next position, and the entire process repeated.

Because the laser is pulsed, the intensity varies in both space and time, so the beam is split up into radial rings of width *dr*, and time-slices of duration *dt*.

A focussed beam is used in the experiments, so the radius of the spot at the front face of the sample varies as the sample is moved through the beam (it is assumed that the beam radius does not vary within the sample. In this case the thickness (~1mm) is small compared to the Rayleigh range of the laser (~7.5mm), suggesting this is the case). The spot size is calculated by assuming a Gaussian profile, and using standard Gaussian optics. So, for each position of the sample, the beam radius, $\omega(z)$, is given by:

$$\omega(z) = \omega_0 \sqrt{1 + (z / z_r)^2} \tag{44}$$

where the Rayleigh range, z_r, is given by:

$$z_r = \frac{\pi\omega_0^2}{\lambda} \tag{45}$$

and ω_0 is the beam radius at focus, z is the distance from focus and λ is the wavelength.

The energy, E, measured in the experiment must be converted into intensity for the calculations. Again, this is done by assuming a Gaussian profile. Therefore, the fluence is given by:

$$F = \frac{2E}{\pi\omega(z)^2}\exp\left[-2\left(\frac{r}{\omega(z)}\right)^2\right] \tag{46}$$

where r is the radius of the particular radial ring being considered. The intensity entering the slice is given by:

$$I_{in} = F\sqrt{\frac{2}{\pi t_0^2}}\exp\left[-2\left(\frac{t}{t_0}\right)^2\right] \tag{47}$$

where t_0 is the $1/e^2$ pulse duration and t is the point in time in the pulse under consideration.

For each position of the sample, the number of carriers generated via two-photon absorption needs to be calculated. This is given by the following equation:

$$N(t) = \int_{-\infty}^{t} \frac{\beta I_{in}^2(t')}{2\hbar\omega}dt' \tag{48}$$

where $N(t)$ is the number of carriers generated in time t, β is the two-photon absorption coefficient and ω is the frequency of the light. This assumes that the carrier recombination time is much longer than the pulse length, and carrier recombination is negligible (see chapter 4, section 4.3.2).

The absorption, $\alpha_{nl}(t)$, due to these carriers is given by:

$$\alpha_{nl}(t) = \beta I_{in}(t) + \sigma_{fca} N(t) \tag{49}$$

where σ_{fca} is the free-carrier absorption cross-section. Hence the intensity leaving the slice is:

$$I_{out}(t) = I_{in}(t)\exp[-\alpha_{nl}(t)dL] \tag{50}$$

This is used as the input to the next slice, until the entire width of the sample has been considered and the final output intensity is calculated. It is then a simple matter to convert the intensity back into energy by integrating over r and t.

The calculated transmitted energy is plotted against sample position, as is the experimental data. The two-photon absorption coefficient is then adjusted until the calculated data is a good fit to the experimental data. The experimental data is normalised by dividing the measured transmission data by the transmission level of the sample when it is far away from focus. This can occasionally result in points having >100% transmission, as evidenced below, where for some reason e.g. scattering or changes in detector response with temperature, more light was measured on the detector.

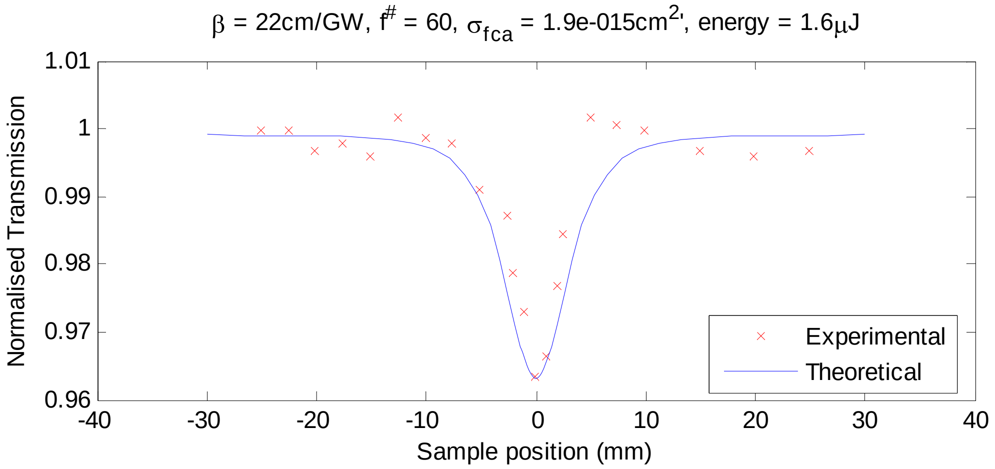

Figure 2.6: Example of an open-aperture fit produced by the modelling program for InP.

Modelling a closed z-scan

A closed z-scan is performed in much the same way as an open one. The difference being that an aperture is placed in front of the detector. The aperture is centred on the beam and partially closed, allowing a known proportion of the total light through. This makes the experiment sensitive to the refractive effects caused by the free-carriers generated in the material.

The model used for generating the theoretical data is similar to the previous one. Again, the beam is split into radial and temporal slices. However, the model needs to consider the phase of the beam so that the effect of the refraction can be modelled. To reduce complexity and computation time, the model does not split the sample into slices.

As before, the intensity entering the sample is given by:

$$I_{in} = \frac{2E}{\pi\omega^2} \exp\left[-2\left(\frac{r}{\omega}\right)^2\right] \sqrt{\frac{2}{\pi t_0^2}} \exp\left[-2\left(\frac{t}{t_0}\right)^2\right] \tag{51}$$

The field incident on the sample is given by:

$$\xi = \sqrt{I_{in}} \exp(-i\psi) \tag{52}$$

Where, from standard Gaussian optics, the phase-shift, ψ is:

$$\psi = \frac{\pi r^2}{\lambda R} - \arctan\left(\frac{z}{z_r}\right) \tag{53}$$

where r is the radius of the ring under consideration and R, the radius of curvature of the wavefront, is:

$$R = z\left[1 + \left(\frac{z_r}{z}\right)^2\right] \tag{54}$$

The number of carriers generated in a short time Δt is:

$$\Delta N = \frac{\beta I_{in}^{2}(t)}{2\hbar\omega}\Delta t \tag{55}$$

These carriers absorb and refract the beam. The nonlinear phase change induced by the carriers is:

$$\phi_{nl} = \frac{2\pi L}{\lambda}\sigma_r N \tag{56}$$

and the total absorption is:

$$\alpha_{nl} = \beta I_{in} + \sigma_{fca} N \tag{57}$$

The field leaving the sample is, therefore, a modification of the input field:

$$\xi_{out} = \xi_{in} \exp\left(-\frac{\alpha_{nl} L}{2} - i\phi_{nl}\right) \tag{58}$$

The output field needs to be propagated to the aperture in front of the detector:

$$\xi_{prop} = J_0\left(\frac{\omega}{\lambda(z_a - z)}\right)\exp\left(-\frac{i\pi\omega^2}{\lambda(z_a - z)}\right)2\pi\omega \tag{59}$$

where z_a is the distance of the aperture from the focus and J_0 is a zero-order Bessel function. The intensity at the aperture (radius a) is:

$$I_a = \left(\int_0^a \frac{\xi_{out}\xi_{prop}}{\lambda(a - z)} r dr\right)^2 \tag{60}$$

Integrating over time gives the fluence as a function of r:

$$F(r) = \int_{-\infty}^{\infty} I_a(r,t)\,dt \tag{61}$$

Similarly, integrating this over the area of the aperture gives the energy:

$$E_{out} = \int_0^a 2\pi r F(r)\,dr \tag{62}$$

The normalised transmission is finally obtained by taking the ratio of the output to input energies, taking into account the transmission of the aperture, T_a.

$$T = \frac{E_{out}}{T_a E_{in}} \tag{63}$$

This calculated transmission is plotted against sample position, as is the experimental data. The nonlinear coefficients are then altered until the theoretical data is a close match for the experimental data.

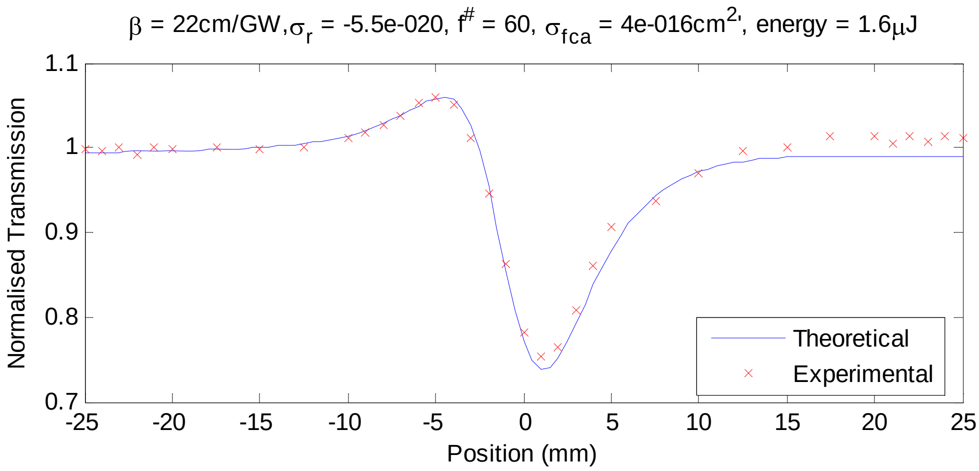

Figure 2.7: Example of a closed-aperture fit produced by the modelling program for InP.

2.4 References

1. E.W. Van Stryland, H. Vanherzeele, M.A. Woodhall, M.J. Soileau, A.L. Smirl, S. Guha, and T.F. Boggess, “Two-photon absorption, nonlinear refraction and optical limiting in semiconductors.” *Opt. Eng.* **24**, 613-623 (1985)
2. A.A. Said, M. Sheik-Bahae, D.J. Hagen, T.H. Wei, J. Wang, J. Young, E.W. Van Stryland, “Determination of bound-electronic and free-carrier nonlinearities in ZnSe, GaAs, CdTe and ZnTe.” *J. Opt. Soc. Am. B* **9**, 405-414 (1992)
3. M.D. Dvorak, B.L. Justus, “Z-scan studies of nonlinear absorption and refraction in bulk, undoped InP.” *Opt. Comm.* **114**, 147-150 (1995)
4. R. Braunstein, “Nonlinear optical effects” *Phys. Rev.* **125** p475 (1962)
5. M. Sheik-Bahae, A.A. Said, T.H. Wei, D.J. Hagen and E.W. Van Stryland, “Sensitive measurement of optical nonlinearities using a single beam.” *IEEE J. Quant. Electron* **26**, 760-769 (1990)
6. E.W. Van Stryland, M.A. Woodhall, H. Vanherzeele, M.J. Soileau, “Energy band-gap dependence of two-photon absorption” *Opt. Lett.* **10** p490 (1985)
7. B.S. Wherrett, A.C. Walker, F.P. Tooley, *Optical Nonlinearities and Instabilities in Semiconductors*, Ch10. Ed. Hartmut Haug (Academic Press 1998)
8. D.H. Auston, S McAffee, CV Shank et al., "Picosecond spectroscopy of semiconductors," *Solid State Electron,* **21**, p. 147 (1978).

3 Femtosecond Measurements on Indium Phosphide

3.1 Introduction

This chapter describes the measurement of the two-photon absorption coefficient, β, of indium phosphide. This was done by performing open-aperture z-scans using a femtosecond laser at the University of St. Andrews. Section 1.2 gives a brief introduction to the chapter, describing the motivation behind the experiments. Section 1.3 contains the details of the experiments performed and the results obtained, followed by the main conclusions in section 1.4. Finally, a list of references is given in section 1.5.

3.2 Isolating the two-photon absorption coefficient

As described previously in chapter 2, if indium phosphide is illuminated with an intense laser beam having a wavelength between the band-edge and twice the band-edge, or, equivalently, a photon energy between the bandgap energy and half the bandgap energy, two-photon absorption can occur. Electrons and holes are created, which can further absorb and refract the beam. These processes occur simultaneously, making it difficult to measure the nonlinearities. However, if the pulse duration is reduced then the relative contributions from two-photon absorption and free-carrier absorption vary. It is shown below that free-carrier effects can be neglected if femtosecond pulses are used.

For the free carrier absorption, α_{fca} to be insignificant compared to the two photon absorption, α_{TPA}:

$$\alpha_{fca} << \alpha_{TPA} \tag{1}$$

Here,

$$\alpha_{TPA} = \beta I_0 \tag{2}$$

and

$$\alpha_{fca} = \sigma_{fca} N \tag{3}$$

where β is the two-photon absorption coefficient and I_0 is the peak intensity. N is the carrier density determined from:

$$\frac{dN}{dt} = \frac{\beta I_0^2}{2\hbar\omega} - \frac{N}{\tau_r} \tag{4}$$

where $\hbar\omega$ is the photon energy. Assuming τ_r, the free-carrier recombination time, to be much longer than the pulse duration, t_0, and integrating equation 4 gives:

$$N = \frac{\beta I_0^2}{2\hbar\omega} t_0 \tag{5}$$

assuming a top-hat pulse. Substituting equations 2, 3 and 5 into 1 gives:

$$\sigma_{FCA} \frac{\beta I_0^2}{2\hbar\omega} t_0 << \beta I_0 \tag{6}$$

and rearranging gives:

$$t_0 << \frac{2\hbar\omega}{\sigma_{FCA} I_0} \tag{7}$$

To be easily measurable, the transmission needs to change significantly, say to e^{-1}. Hence:

$$T = e^{-\alpha_{TPA} L} \approx e^{-1} \tag{8}$$

where L is the sample thickness. Substituting 2 into this gives:

$$e^{-\beta I_o L} \approx e^{-1} \tag{9}$$

Hence:

$$I_0 = \frac{1}{\beta L} \tag{10}$$

Finally, substituting this into 7 gives:

$$t_0 << \frac{2\hbar\omega\beta L}{\sigma_{FCA}} \tag{11}$$

Inserting the best estimates for these factors:

$\hbar\omega$ = 1.51x10^{-19}J (from experiment)
β = 25x10^{-11}m/W (from theory[1])
σ_{fca} = 1x10^{-20}m^2(overestimate from experiments in chapter 4 and 5)
L = 0.001m (from experiment)

gives t_0 << 1ps. It should be noted that whereas the above analysis assumes a top-hat pulse, in reality the pulse is near-Gaussian. This means that the intensity will be lower at the wings of the pulse, so the number of carriers generated will be lower.

This result shows that in order to isolate the two-photon absorption coefficient, β, from free-carrier absorption, it is necessary to use pulses less than 1ps. The pulse length of the laser used in the experiments later in this chapter is 130fs. This is much smaller than 1ps so the free carrier absorption should be negligible, allowing β to be measured unambiguously.

In the results section following, two methods have been used to determine β from the experimental data. By neglecting the linear and free-carrier absorption, the change in intensity with position in the sample, z, is just:

$$\frac{dI(r,z,t)}{dz} = -\beta I_{in}(r,z,t)^2 \tag{12}$$

Integrating this over the thickness of the sample, L, gives:

$$I_{out}(r,t) = \frac{I_{in}(r,t)}{1+\beta I_{in}(r,t)L} \tag{13}$$

where $I_{out}(r,t)$ is the output (transmitted) intensity. Hence

$$\frac{I_{in}(r,t)}{I_{out}(r,t)} = \frac{1}{T} = 1 + \beta I_{in}(r,t)L \tag{14}$$

where T is the transmission at focus. This allows β to be determined by plotting $1/T$ vs.I_{in}. Although quick and simple to do, only one data point for each scan is used for this method. A more complicated but more accurate method, which uses all of the data points for each energy scanned, was also used. This was described previously in chapter 2, section 2.3.1.

3.3 Initial experimental procedure and results

3.3.1 Experimental description

In this section a description of how I set up the z-scan experiment is given. A Spectra Physics Hurricane system was used to pump an optical parametric amplifier (OPA) to produce 1.32µm 130fs pulses at 5kHz. The apparatus was arranged as in figure 3.1.

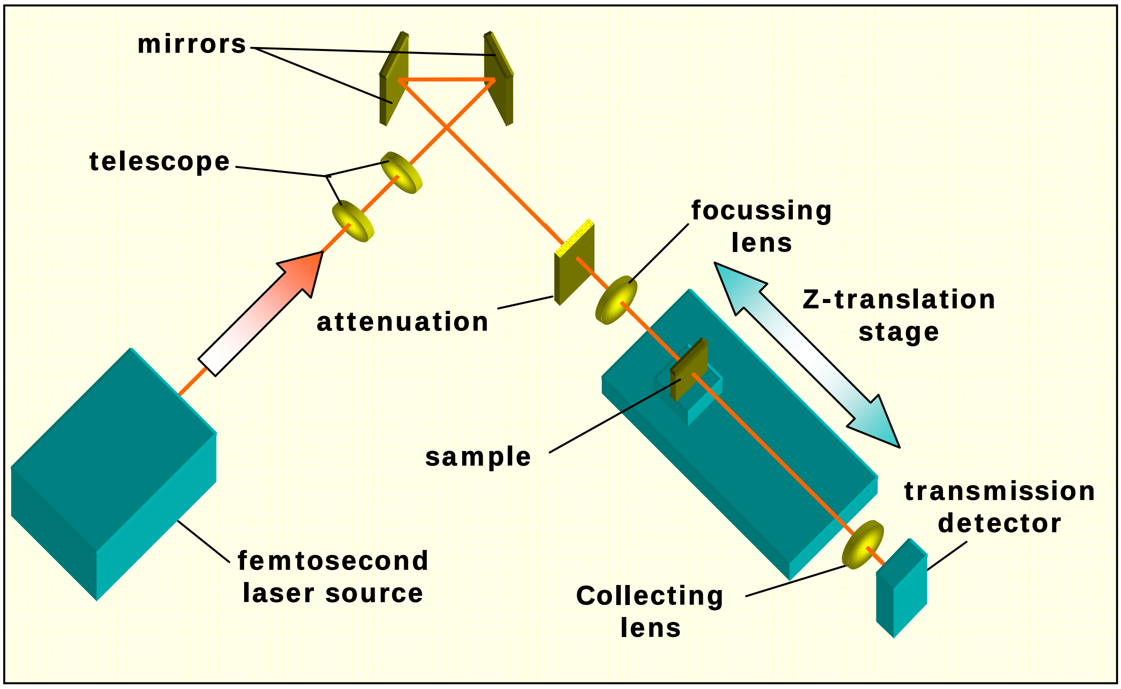
mirrors
telescope
focussing lens
Z-translation stage
attenuation
sample
transmission detector
femtosecond laser source
Collecting lens

Figure 3.1: Experimental apparatus for femtosecond open-aperture z-scans

The first two lenses were used as a telescope. This allowed the size of the beam entering the z-scan focussing lens to be altered, so that the speed of the focus onto the translation stage could be optimised, allowing the entire range of motion of the stage to be used.

The final lens was used to collect light transmitted by the sample for focussing onto the detector, ensuring that the total transmitted beam energy was measured. This lens was used because of the possibility of nonlinear refraction occurring within the sample, causing the beam to diverge (or converge). If this was to occur then some of the light would miss the detector so the measured transmission drop would be larger than from nonlinear absorption alone, so β would be calculated to be higher than it actually is.

The indium phosphide sample was mounted on a computer controlled Aerotech translation stage. The germanium photo-detector was connected to a Stanford Research Systems lock-in amplifier, which in turn was connected to a computer. This allowed the transmitted energy to be measured via computer every time the stage moved the sample into a new position. A calibrated Laser Probe power meter was used to measure the energy of the incident beam.

The attenuators were characterised to allow the voltage reading from the detector to be converted into an intensity or energy. This was done by measuring the energy transmitted by different combinations of attenuators in the beam path, corresponding to the combinations to be used in the experiment. The same energies were then measured on the detector to enable a conversion factor to be calculated.

Next, the spatial profile of the beam was measured by scanning a pinhole across the x and y axes of the beam and measuring the energy transmitted. This was done at focus and 21cm in front of focus, allowing the beam radius at focus to be determined and the beam quality to be estimated.

Finally, the open aperture z-scans were performed. For each of the different energies measured above, the sample was moved from approximately 15cm in front of focus to approximately 15cm behind it, in steps of 2mm. The transmitted energy was recorded along with the corresponding sample position. The plotted data can be found in the results section, below.

3.3.2 Experimental results

Power calibration

Figure 3.2 below is a plot of the same signal measured on both the power meter (y-axis) and the photo-detector (x-axis). The points lie on a curve, showing that either the detector or the power meter (or both) has a slightly nonlinear response. The power meter was rated to higher powers than those used suggesting that the nonlinearity lies with the photo-detector. In hind-sight, this is not surprising considering the range of powers measured. At lower powers the response appears to be linear (see fig. 3.2 inset).

Due to the TPA the powers transmitted through the sample when it is at focus are relatively small. Therefore it is more accurate to use a fit of the points at low powers to calculate the conversion factor. The dashed line represents this.

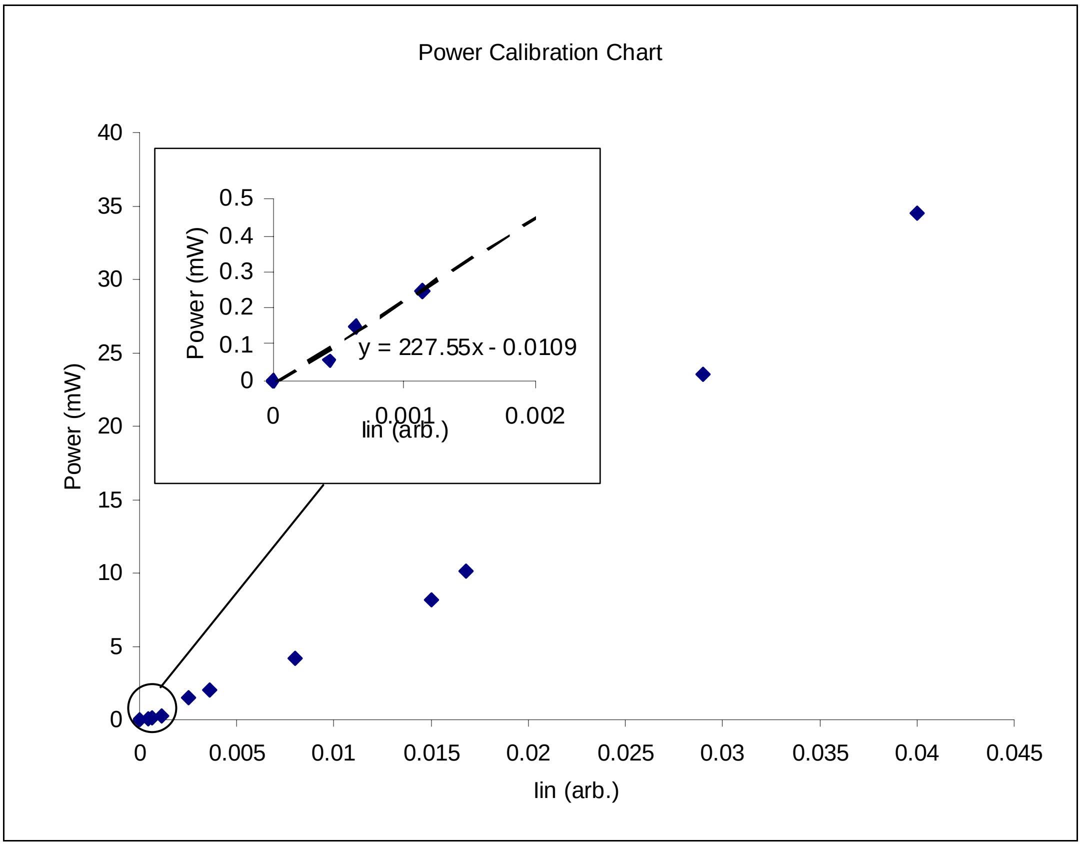

Figure 3.2: Power calibration for the detectors. The points lie on a curve suggesting the detector response was nonlinear. The inset chart shows a fit to the low power data, where the detectors were behaving linearly.

Beam spatial profile

The spatial profile of the beam was measured by scanning a pinhole across the beam and measuring the energy transmitted through it. The pinhole was small (approximately 10µm) in comparison to the diameter of the beam. The profile displayed in figures 3.3 and 3.4 shows that the beam was slightly elliptical in shape. The $1/e^2$ radius was calculated to be approximately 280µm. Unfortunately there was a lot of noise on the data that was taken 21cm in front of focus due to the beam being less intense. This made the data unusable and, in retrospect, a larger diameter pinhole should have been used.

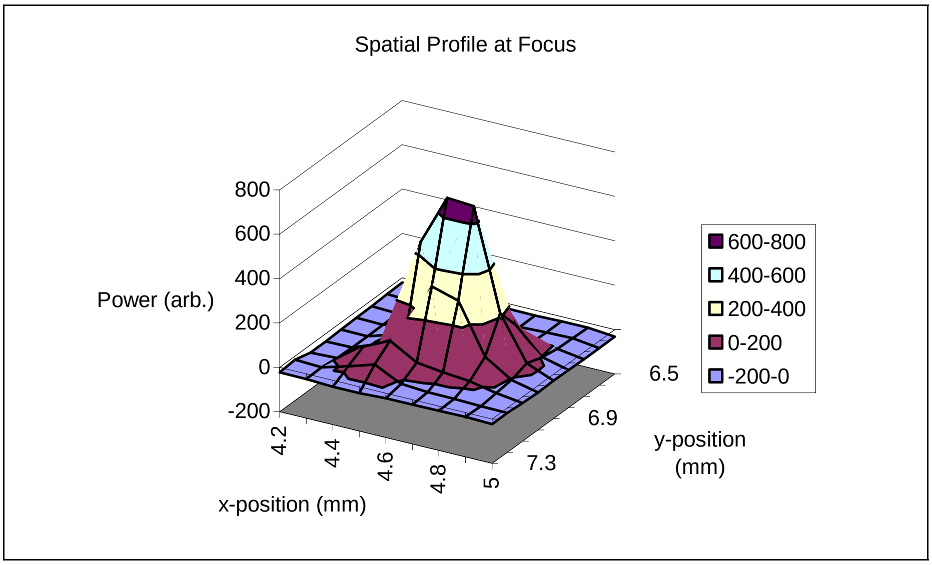

Figure 3.3: 3D spatial profile of the focal point of the laser beam.

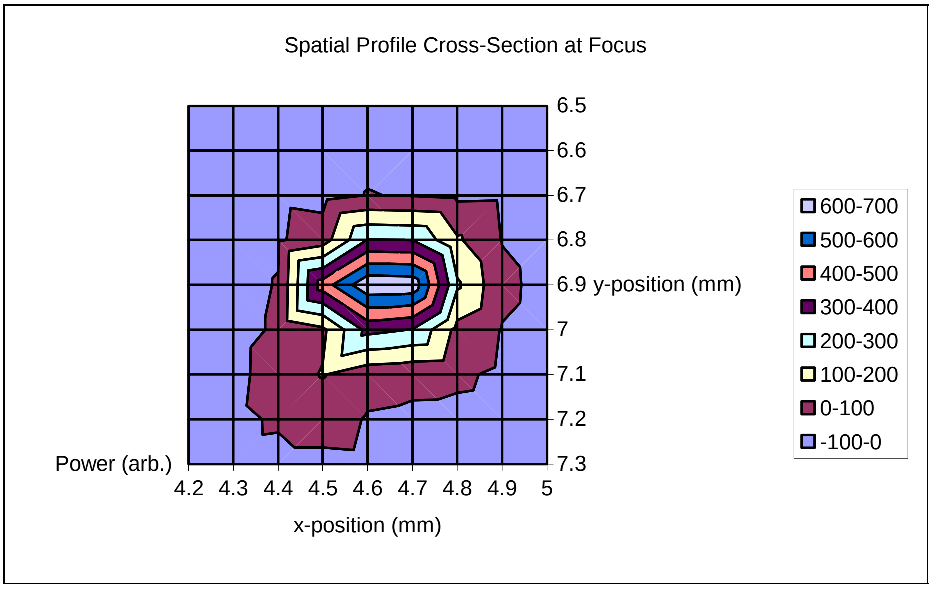

Figure 3.4: Cross-section of the focal point of the laser beam.

Nonlinear transmission

Figure 3.5 shows the results of plotting the input intensity (I_{in}) divided by the output intensity (I_{out}) (the inverse transmission) vs $I_{in}*L$, where L is the sample thickness (1mm), when the sample is at focus. In all cases the intensities were average intensities.

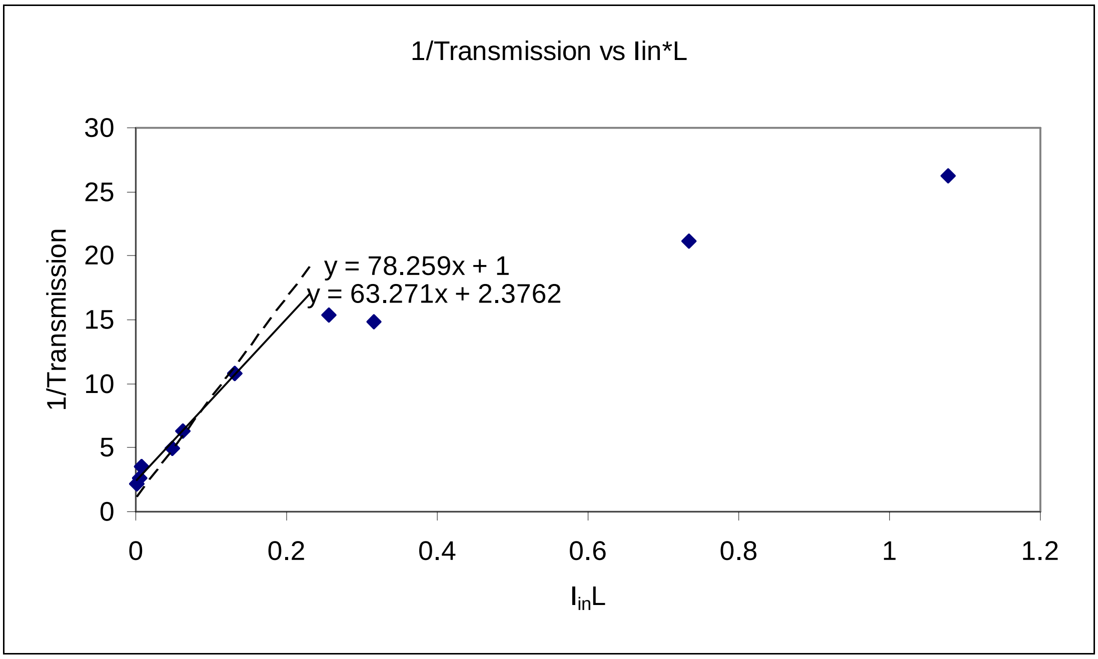

Figure 3.5 – Plot of 1/*T* vs I_{in}L*, used to calculate *β*.**

The data points were collected by looking at the open aperture z-scans and choosing the minimum transmitted intensity points i.e. when the sample was at the focal point of the laser. In each case the minimum occurred at the same or within 1 step of the same sample position (144 ± 2mm) showing that the data sets are consistent with each other. According to equation 40 the graph should be linear, with the gradient of the line equal to *β*, and the intercept with the y-axis having a value of 1. The data does not agree with this however as the graph is curved. The best fit line gives a value of 63cm/GW for *β*, but the intercept is 2.4. If the intercept is forced to 1 then a value of 78cm/GW is obtained but the line is a worse fit to the points.

Open aperture z-scans

Figure 3.6 shows all of the open aperture z-scans taken with input energies ranging from 0.01μJ to 6.9μJ (points) and the fits generated from theory (lines). It should be noted that there was an experimental error with the 0.05μJ data resulting in the measured transmission decreasing beyond focus. Before and around the focus the data is correct.

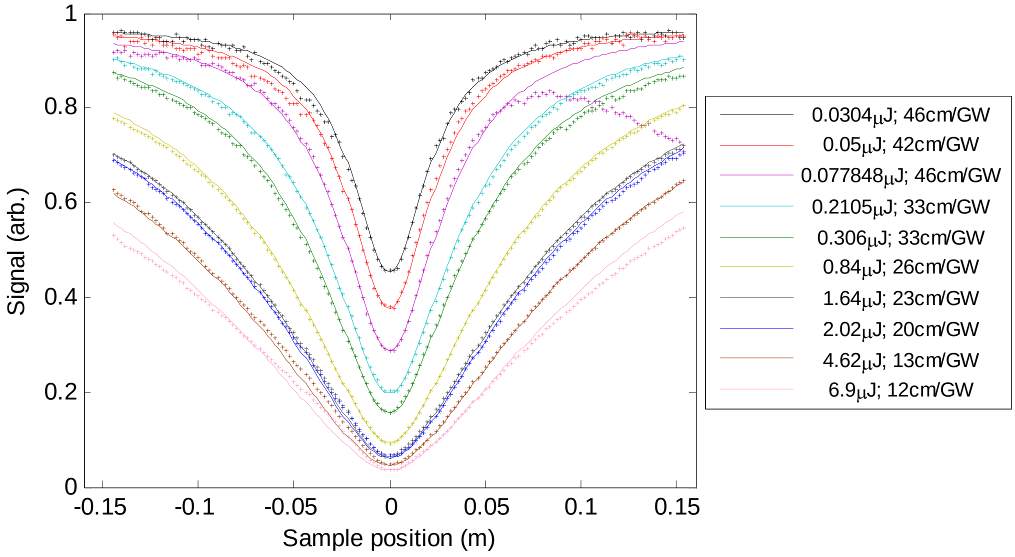

Figure 3.6: Open aperture z-scans performed on InP with various input energies (points) and their fits generated from theory (lines).

As the sample approached focus the absorption increased. The absorption then decreased as the sample moved away from focus. This is because the two photon absorption is intensity dependent. As the sample approached focus, the beam diameter decreased so the intensity, and hence the absorption, increased. Similarly, at higher energies the magnitude of the transmission drop was larger, again due to the increase in intensity. At the highest energies used, the transmission drop was so large that the range of motion of the stage was not large enough to capture the point at which the transmission returned to 100%.

To generate the fits, transmission values calculated from equation 40, described in chapter 2, section 2.3.1, were plotted against the experimental data. The only unknown parameter was β. This was altered until a good fit to the data was obtained. Table 3.1 shows the results of fitting all the data points at each of the energies. The first three results performed at the lower energies produce similar β values of approximately 45cm/GW. This is of the same order as the theoretical value of 25cm/GW. It also compares well with a number of recent experimental measurements. My colleagues and I have been collaborating with Heriot Watt University and Raytheon investigating optical nonlinearities in InP[2]. Both groups have measured β independently to be 20-35cm/GW at 1.245μm and 1.515-1.600μm using femtosecond z-scan experiments. This is in agreement with Vignaud et al.[3], who measure β to be 24-33cm/GW in doped InP substrates at 1.55μm. It is lower and in better agreement with theory than the results of

Tiedje et al.[4], who report a value of 70cm/GW at 1.305μm and Dvorak and Justus[5], who report β to be 90cm/GW at 1.064μm.

Energy (μJ)	**0.0304**	**0.05**	**0.0778**	**0.21**	**0.306**	**0.84**	**1.64**	**2.02**	**4.62**	**6.9**
Beta (cm/GW)	46	42	46	33	33	26	23	20	13	12

Table 3.1: Two-photon absorption coefficients determined by fitting all data points for each of the energies.

At higher energies the results seem to indicate that β varies with energy. According to theory β should be independent of energy. It is unknown what effect causes the observed variation, especially as the fits remain good, ruling out higher order multi-photon absorption, which would cause the fit near focus to be incorrect. Most of the possible experimental errors result in an increase of the measured β value as the energy is increased. For instance, if it was an energy detection problem, it would most likely be due to one or more detectors saturating at high energies. The detector would measure a lower energy value than in reality resulting in a higher value for β being required to generate a good fit – the opposite of what is observed. Possible unaccounted nonlinear effects occurring include free-carrier absorption and refraction and the Kerr effect. However, femtosecond pulses were used precisely to remove the free-carrier effects, so they are unlikely. In addition, these nonlinearities all result in an increase in the β value required as the energy increases. In any case, a closed z-scan was performed to check for refractive effects and none were observed, although it's much easier to see a negative result than a positive result in this case. Finally, and seemingly most likely, it's possible that the two-photon absorption was saturating through some physical process. For example, if the free electron transition states in the material filled up due to the amount of carriers being generated, it would not be possible for electrons to traverse the bandgap without increasing the photon energy. This would result in the TPA becoming constant even though the energy is increasing, resulting in the required β value decreasing.

Measuring the uncertainty in the result is fairly difficult due to fitting the results 'by-eye'. A reasonable method would be to vary the beta value to the maximum and minimum extremes of when the theoretical data still fitted the experimental data. The uncertainty in the energy and beam size measurements also needs to be included. Overall assuming an error of ± 10cm/GW would appear to be reasonable.

3.4 Conclusions

The results from the z-scans suggest that the two-photon coefficient has a value of approximately 45 ± 10cm/GW. This is of the same order as the 25cm/GW predicted by theory [1] and the results of other recent measurements[2-5]. However β was found to vary with energy at higher energies. The reason for this observation is unknown, although the most likely explanation appears to be some sort of saturation of the nonlinear absorption, possibly due to conduction band filling.

3.5 References

1. E.W. Van Stryland, M.A. Woodall, H. Vanherzeele, M.J. Soileau, “Energy band-gap dependence of two-photon absorption” *Opt. Lett.* **10** p490 (1985)
2. T.J. Sloanes, P.K. Milsom, K.J. McEwan, M.B. Haeri, T.O. Clatterbuck, J. McCartney, H. Bookey, A.K. Kar, “Two-photon induced free-carrier absorption and refraction in indium phosphide”, *To be submitted to J. Appl. Phys.*
3. D. Vignaud, J.F. Lampin, F. Mollot,”Two-photon absorption in InP substrates in the 1.55µm range” *Appl. Phys. Lett.* **85(2)** p239 (2004)
4. H.F. Tiedje, H.K. Haugen, J.S. Preston, “Measurement of nonlinear absorption coefficients in GaAs, InP and Si by an optical pump THz probe technique” *Opt. Comm.* **274** p187 (2007)
5. M.D. Dvorak, B.L. Justus, “Z-scan studies of nonlinear absorption and refraction in bulk, undoped InP” *Opt. Comm.* **114** p147 (1995)

4 Nanosecond Measurements on Indium Phosphide

4.1 Introduction

The aims of the experiments described in this chapter are to measure the absorption and refraction of the two-photon absorption-generated free-carriers in indium phosphide (InP). This is done by performing open and closed aperture z-scans with nanosecond pulses. Such relatively long pulse-lengths are used because the effects of the free-carrier nonlinearities are readily observable on this timescale.

Unfortunately, the two-photon absorption used to generate the carriers also contributes to the measured absorption. In order to find the free-carrier coefficients, the two-photon absorption (TPA) coefficient, β, must be determined and accounted for. This was done using the femtosecond experiments described in chapter 3.

The first section of this chapter shows the characterisation of the piece of indium phosphide and the beams used in the z-scans. Next, the z-scans performed at 1.064μm are described followed by the results and analysis of those experiments. This is repeated for the 1.534μm z-scans. Finally, the main conclusions of the experiments are given, followed by a list of references at the end of the chapter.

4.2 Beam and material characterisation

The mathematical models used to extract the nonlinear coefficients from the experimental data rely on assumptions of Gaussian beams. Therefore, it is important to characterise the laser beams in use to determine whether these approximations are valid. This section of the chapter describes how these measurements were performed.

4.2.1 Measurement of 1.064μm beam waist and M^2-value

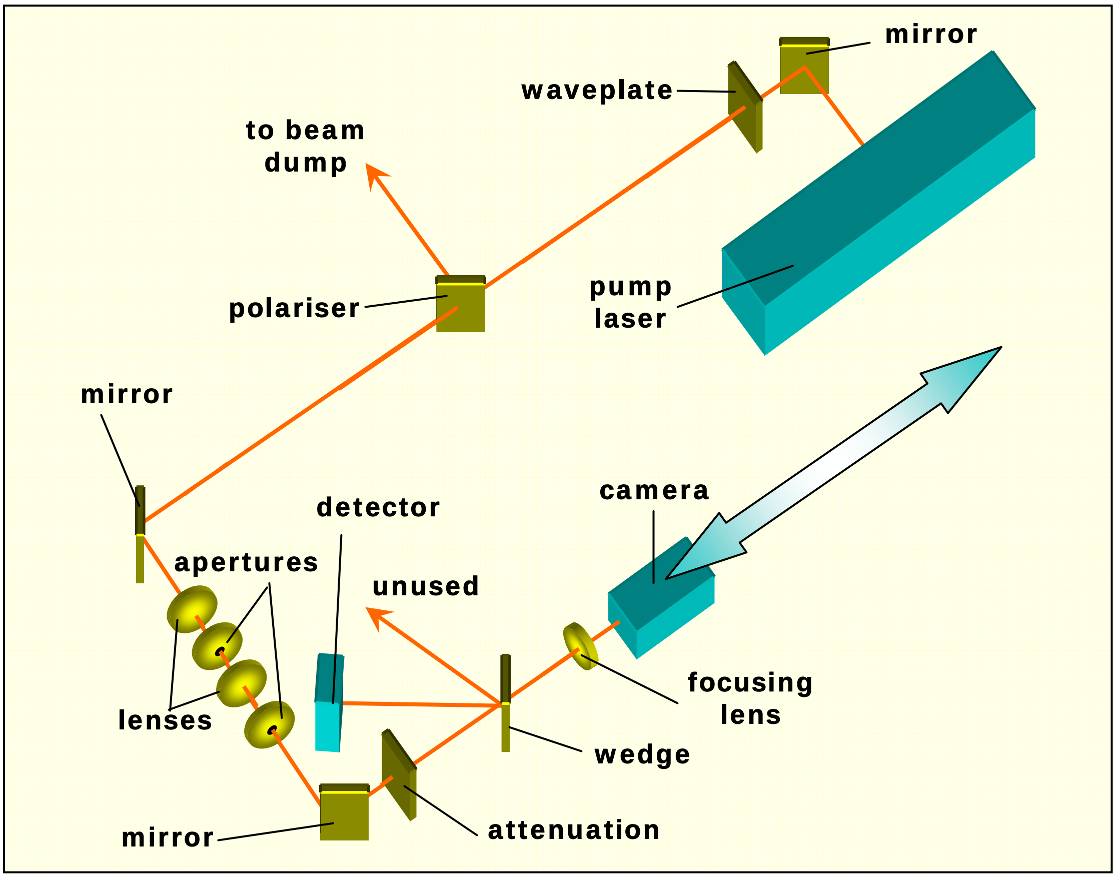
mirror
waveplate
to beam dump
polariser
pump laser
mirror
camera
detector
apertures
unused
lenses
focusing lens
wedge
mirror
attenuation

Figure 4.1: Experimental set-up for characterising the 1.064μm laser.

Figure 4.1 shows how I set up the experimental apparatus to enable the laser to be characterised. Essentially, the layout was the same as that used for the z-scan experiments described later, but with an infra-red sensitive camera placed where the translation stage and sample mount would normally be positioned.

The source laser was a 1.064μm Nd:YAG laser producing Q-switched pulses of 16.1ns (FWHM) duration at a repetition rate of 10Hz. It had a maximum energy output of

400mJ, although only a few mJ at most were used in these experiments. Most of the energy was dumped using a 1% reflecting mirror, and a rotating waveplate and polariser were used to control the energy in the transmitted beam. The beam passed through a spatial filter to improve the beam quality before being attenuated further via the use of neutral density filters. A wedge was used to produce two reflections offset slightly from each other. One of the reflections was monitored on a detector to give a reference measurement whilst the second was unused in the characterisation process. The main beam was focused with a 20cm lens that had an effective length of 16cm. A video camera was placed where the sample translation stage would normally be positioned so that the beam size could be measured at various positions along the beam's z-axis.

First, the camera was used to measure the $1/e^2$ beam radii at and around focus, so that the beam waist could be determined as accurately as possible. This was found to be 49μm, which corresponds to a confocal parameter of 14mm. This is much larger than the thickness of the sample (1mm) verifying that the sample is thin (external self-action[1,2]) and approximations made with respect to the beam not changing in size through the sample (see chapter 2) are valid.

Next, an M^2 measurement of the beam was made. This is a measure of how closely a beam approximates a Gaussian. In order to do this more easily and accurately, the focusing lens was replaced with one of longer focal length (40cm, 37cm effective). Using the longer focal length lens meant that the system had a larger f-number, so the beam diameter and hence intensity varied more slowly with z-position. This made the measurements easier because the attenuators used to protect the camera from damage did not need to be changed as often. Also, the beam waist was larger meaning that the beam covered more pixels, improving the accuracy of the measurement.

Beam diameter measurements were collected at various positions along the beam's axis. The data was squared, and a least-squares fit was used to extract the M^2 and $f^{\#}$ of the beam. A description of the technique follows.

The beam radius at any z-position, $\omega(z)$, is given by:

$$\omega(z) = \omega_0 \sqrt{1 + \left(\frac{z - z_0}{z_r} \right)^2} \tag{1}$$

where

$$z_r = \frac{\pi \omega_0^2}{\lambda M^2} \tag{2}$$

and ω_0 is the beam radius at focus, λ is the wavelength, z is the measurement position, z_0 is the focal position and M^2 is the beam quality factor.

Substituting eqn. 2 into eqn. 1 and rearranging gives:

$$\omega(z)^2 = \omega_0^2 + (z - z_0)^2 \frac{\lambda^2 M^4}{\pi^2 \omega_0^2}$$

Expanding the squared bracket yields:

$$\omega(z)^2 = \left(\omega_0^2 + z_0^2 \frac{\lambda^2 M^4}{\pi^2 \omega_0^2} \right) - 2 z z_0 \frac{\lambda^2 M^4}{\pi^2 \omega_0^2} + z^2 \frac{\lambda^2 M^4}{\pi^2 \omega_0^2}$$

Hence

$$\omega(z)^2 = a z^2 + b z + c \tag{3}$$

where

$$a = \frac{\lambda^2 M^4}{\pi^2 \omega_0^2} \tag{4}$$

$$b = -2 z_0 \frac{\lambda^2 M^4}{\pi^2 \omega_0^2} \tag{5}$$

$$c = \omega_0^2 + z_0^2 \frac{\lambda^2 M^4}{\pi^2 \omega_0^2} \tag{6}$$

i.e. a is the z^2-term, b is the z-term and c is the constant term.

Substituting eqn. 4 into eqn. 5 yields:

$$b = -2 z_0 a$$

Hence:

$$z_0 = \frac{-b}{2a} \tag{7}$$

Substituting eqn. 4 into eqn. 6 yields:

$$\omega_0 = \sqrt{c - z_0^2 a} \tag{8}$$

then substituting eqn. 7 into eqn. 8 yields:

$$\omega_0 = \sqrt{c - \frac{b^2}{4a}} \tag{9}$$

Rearranging eqn. 4 in terms of M^4 and taking the square-root gives:

$$M^2 = \frac{\pi \omega_0}{\lambda} \sqrt{a} \tag{10}$$

then substituting eqn. 9 into 10 gives:

$$M^2 = \frac{\pi}{\lambda} \sqrt{ac - \frac{b^2}{4}} \tag{11}$$

The $f^{\#}$ of an optical system is given by:

$$f^{\#} = \frac{\pi\omega_0}{2M^2\lambda} \tag{12}$$

Substituting eqn. 4 into eqn. 12 yields:

$$f^{\#} = \frac{1}{2\sqrt{a}} \tag{13}$$

Hence, the focal position, z_0, the beam waist, ω_0, the M^2 of the beam, and the $f^{\#}$ have all been expressed in terms of the polynomial coefficients obtained from a parabolic least-squares fit to the experimental data.

Figure 4.2 shows the least-squares fit to the experimental data. Data regression is used to extract the *a*, *b* and *c* terms. Inserting them into the above equations yields an M^2 of 1.12, a beam waist of 106μm and an $f^{\#}$ of 140. This is with a f=40cm lens (effective 37cm) whereas the z-scan experiments use a f=20cm (effective 16cm). Therefore, the actual experimental $f^{\#}$ is 16/37*140 = 60.2.

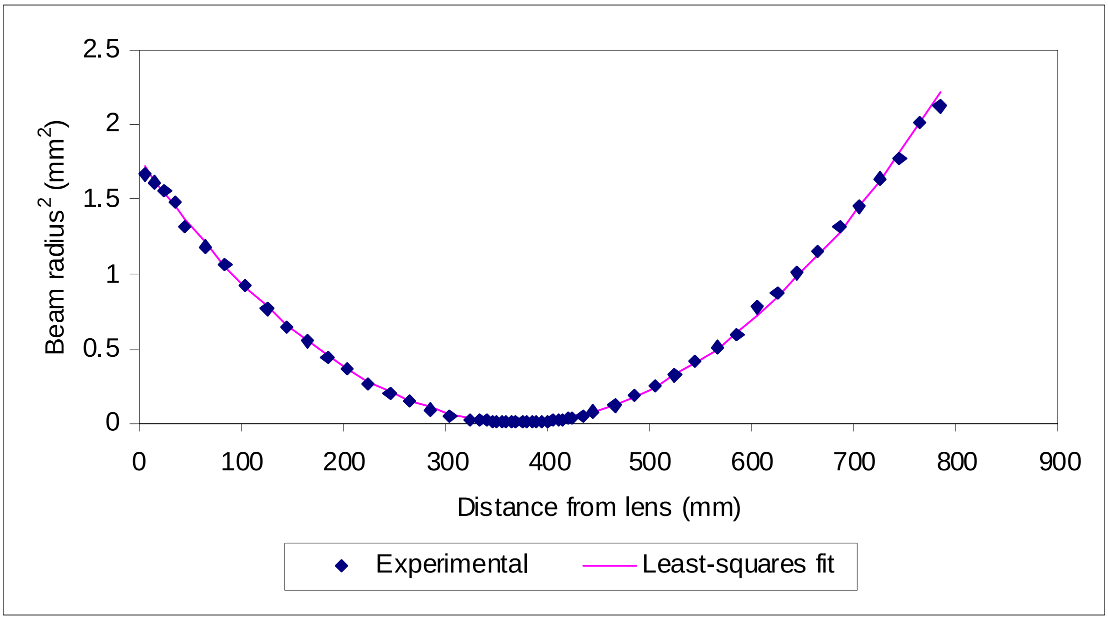

Figure 4.2: M^2-value measurement for the 1.064μm beam used in the z-scan experiments. A least-squares fit gives an M^2 of 1.12.

4.2.2 Measurement of 1.534µm beam waist and M^2-value

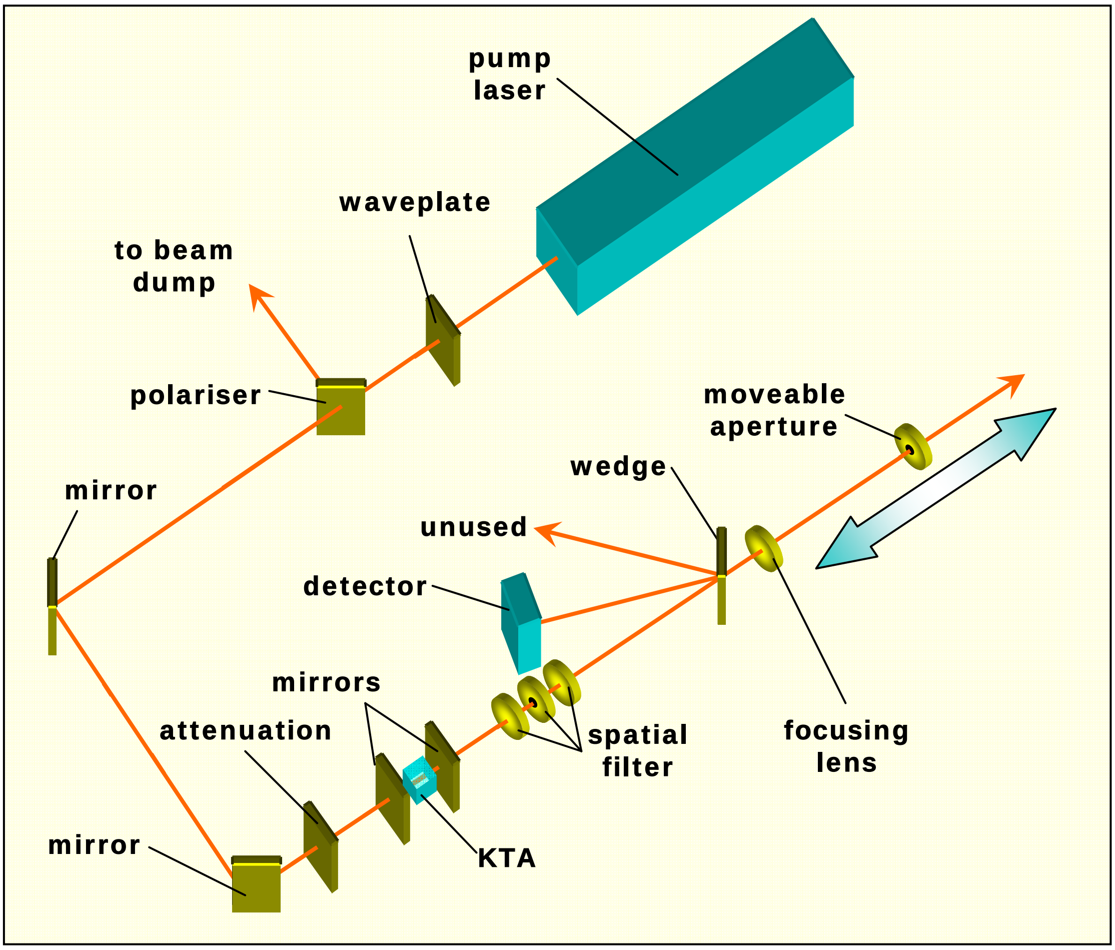
pump laser
waveplate
to beam dump
polariser
moveable aperture
wedge
mirror
unused
detector
mirrors
attenuation
spatial filter
focusing lens
mirror
KTA

Figure 4.3: Experimental set-up for characterising the 1.534µm laser.

The experimental set-up used for characterising the 1.534µm beam, shown in fig. 4.3, was very similar to that used for the 1.064µm beam. The main difference being that an optical parametric oscillator (OPO) is present, which is used to convert some of the 1.064µm to 1.534µm light.

The OPO consisted of a 20mm long potassium titanyle arsenate ($KTiOAsO_4$, or KTA) crystal cut for non-critical phase matching and AR coated for the signal (1534nm), idler (3473nm) and pump (1064nm) wavelengths. The crystal was situated between two mirrors spaced 35mm apart to form a plane-plane cavity, as shown in figure 4.4. One of the mirrors was highly reflective at 1534nm, the other only transmitted approximately 40% of the 1534nm light generated in the crystal. The pump beam was relatively small at the OPO (1.5mm $1/e^2$ diameter) to give a low threshold and to discriminate against higher order spatial modes. The OPO threshold was ~10mJ so typically it was operated at a pump-energy of 15mJ, giving an output energy of ~1mJ at 1534nm. The FWHM pulse duration was measured as 10.1ns on a fast detector connected to a digitising oscilloscope. The signal was separated from the pump and idler using dichroic mirrors and filters. The beam quality was measured and found to be quite poor, having an M^2 of ~2. A spatial filter was added to improve the beam, reducing the M^2 to 1.2, as will be shown. Unfortunately no camera suitable for measuring the beam at 1.534μm accurately was available, so a different technique had to be employed. It was based on the fact that a circular aperture, of known diameter, will transmit a known proportion of a Gaussian if the beam and aperture are centred relative to each other.

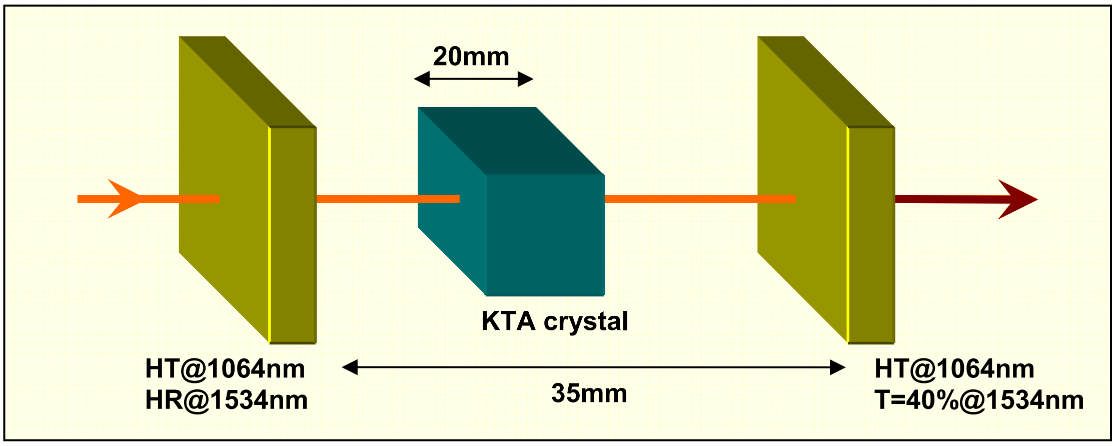

Figure 4.4: OPO configuration for 1.534μm generation.

If the aperture has a diameter, a, and the fraction of light transmitted by the aperture is T, then the beam diameter, ω, is given by:

$$\omega = \frac{a}{\sqrt{-\frac{1}{2}\ln(1-T)}} \tag{14}$$

Placing apertures in the beam at various z-positions and measuring the amount of light transmitted allowed an M^2 for the beam to be measured.

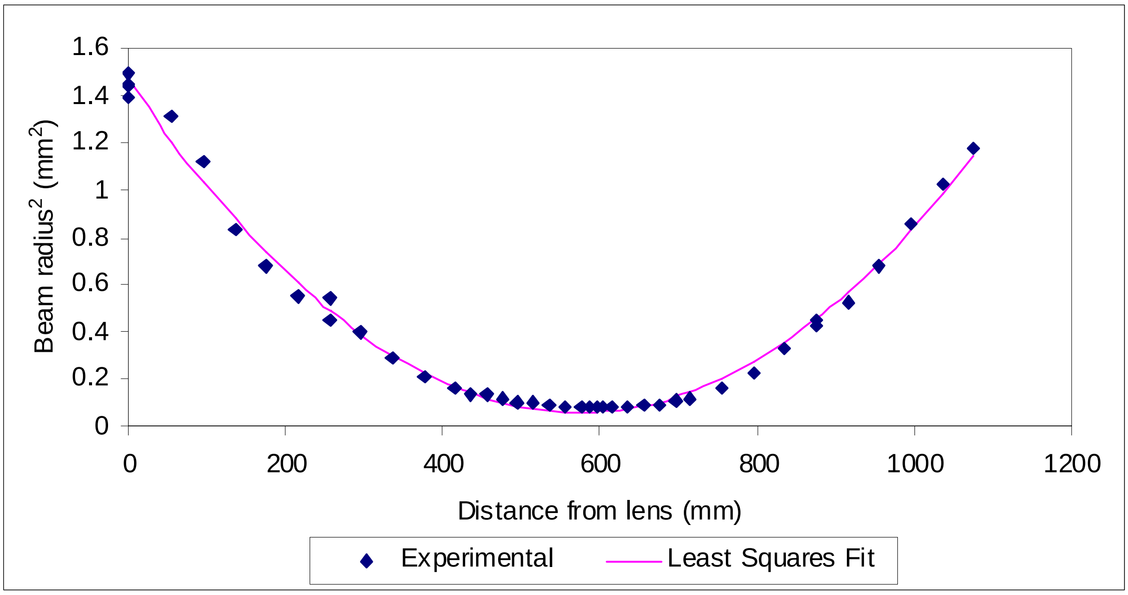

Figure 4.5: M^2 measurement using least squares fit method.

As before, this M^2 was determined using a least-squares fit, shown in figure 4.5. This method produced a value of 1.03 with a waist of 244µm. The $f^{\#}$ was 64. Although the M^2 is better than in the previous case with the 1.064µm beam, the least-squares fit to the experimental data is actually worse. It's probable that this is because the aperture method has more opportunities for experimental error to occur; for example dust in the pinholes, pinholes not centred on the beam correctly etc.

4.2.3 Indium phosphide characterisation

Before any nonlinear effects were investigated, the linear properties of the material were measured. The piece of InP used in each of the following experiments was bought from Wafertech as 1mm thick wafers of diameter 5cm. The sample was cut along the [100] axis by the manufacturer and both sides of the wafer were optically polished. The wafers were then cut into 1cm^2 squares and anti-reflection coated. The transmission characteristics of the sample were measured by placing it inside a PerkinElmer Lambda-9 spectrometer and scanning from 800nm to 2000nm

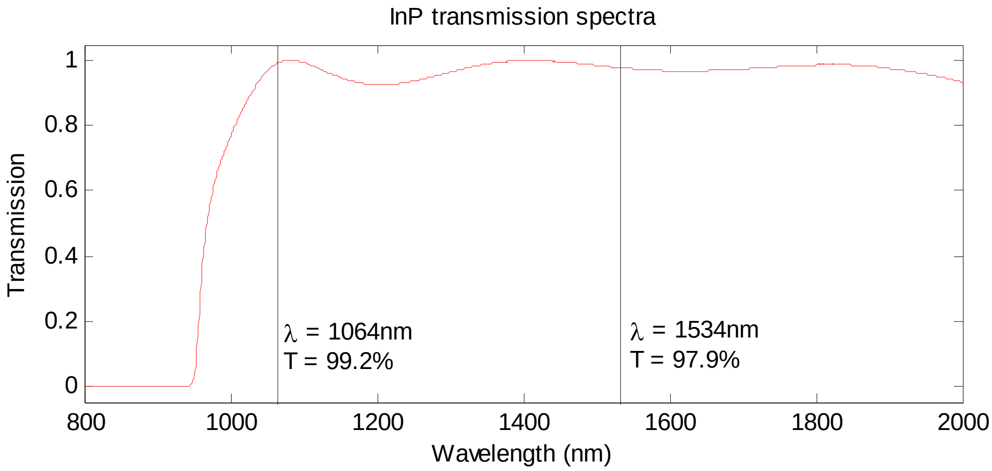

Figure 4.6: Transmission spectrum of anti-reflection coated 1mm thick InP.

Figure 4.6 shows the transmission characteristics of the sample. The graph shows that there is very high transmission at 1.064μm and 1.534μm, which are the wavelengths being used in the experiments.

As mentioned in chapter 2, an expression for β exists which is dependent only on the linear refractive index, n_0, and the energy gap of the material, E_g[3]:

$$\beta(2\omega') = K\frac{\sqrt{E_p}}{n_0^2 E_g^3} F_2\left(\frac{2\hbar\omega'}{E_g}\right) \tag{15}$$

where K is a material-independent constant having a value of $3.1\text{x}10^3$ (in units such that E_p and E_g are in eV and β is in cm/GW[6]), E_p, which is related to the Kane momentum parameter, is nearly material independent and possesses a value of ~21eV for most direct-gap semiconductors. F_2 is a function of the form:

$$F_2(x) = \frac{(x-1)^{3/2}}{(x)^5} \tag{16}$$

As can be seen, knowing the refractive index and the energy gap allows the two-photon absorption coefficient to be estimated. These quantities were obtained as described below.

Examining the transmission spectrum in figure 4.6, the onset of absorption occurs at 950nm. This corresponds to a photon energy of 1.305eV. However, this is probably an inaccurate way of measuring the bandgap, as it is difficult to define how much transmission is required before one can definitely say the bandgap has been reached i.e. is it best to choose the wavelength where absorption just begins (as above) or the wavelength of maximum transmission? It will also depend on other factors, such as the thickness of the material. Instead of using this technique, an empirical formula proposed by Varshni[4] was used:

$$E_g(T) = E(0) - \frac{aT^2}{T + b}$$

Hang et al[5] determined these parameters, and their results agree approximately with earlier workers. The parameters are E(0) = 1.432eV, a = 4.1×10^{-4}eV/K and b = 136K. Assuming a room temperature of 300K gives an energy gap of 1.347eV.

The variation of the refractive index with wavelength was measured by Pettit and Turner[6]. They obtained an empirical formula to describe this:

$$n = \sqrt{A + \left(\frac{B\lambda^2}{\lambda^2 - C^2} \right)}$$

where A = 7.255, B = 2.316 and C^2 = 0.3922μm, and λ is the wavelength in microns.

Using this equation, n_0 = 3.29 at 1.064μm and 3.17 at 1.53μm. Inserting the energy gap and refractive indices into eq. 15, β is 22cm/GW for 1.064μm and 20cm/GW for 1.53μm light.

4.3 Free-carrier lifetime measurements

As part of an MSc project conducted by the author, the free-carrier lifetime of InP had previously been measured. For the sake of completeness, a description of the experiment and the results obtained are included below.

4.3.1 Experimental procedure

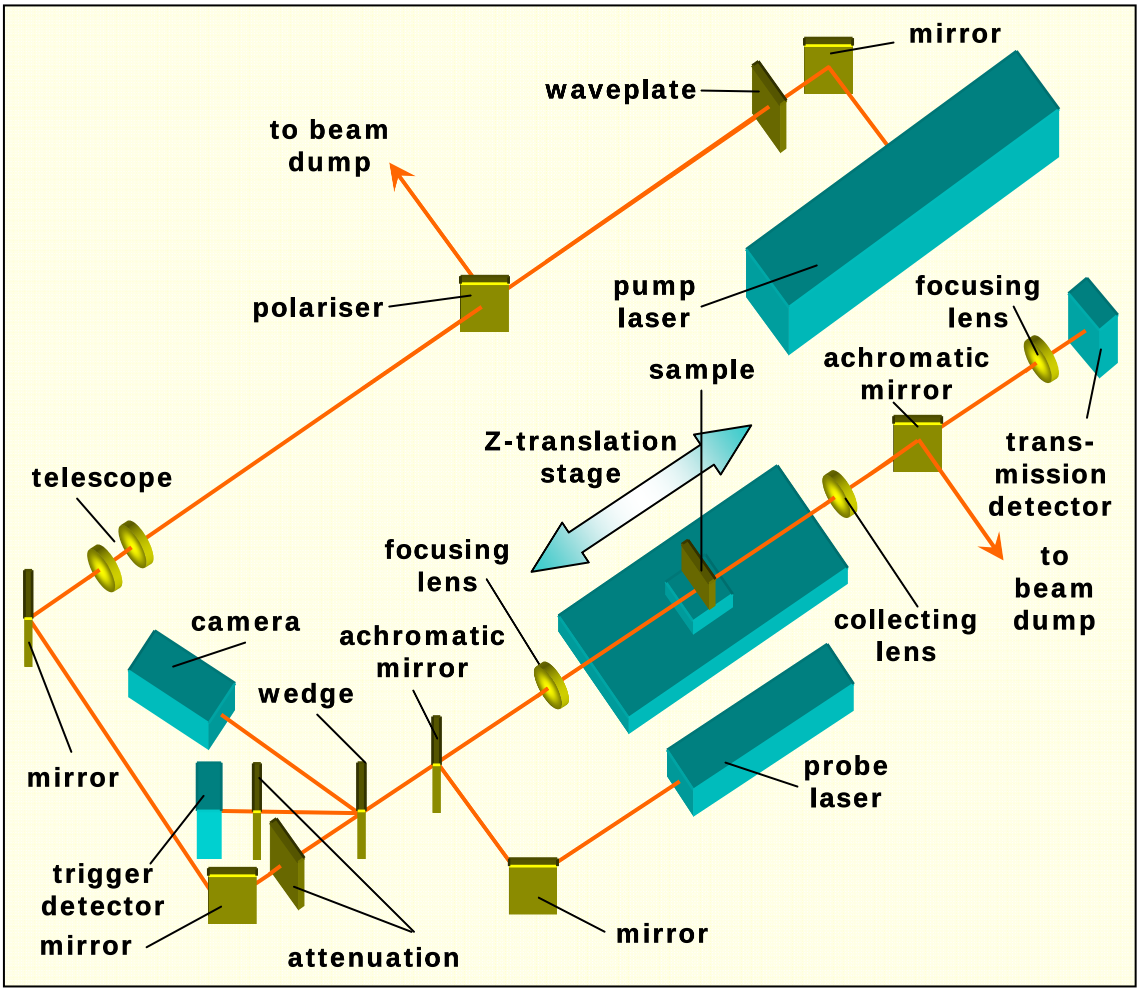
mirror
waveplate
to beam dump
polariser
pump laser
focusing lens
sample
achromatic mirror
Z-translation stage
trans-mission detector
telescope
focusing lens
to beam dump
camera
achromatic mirror
collecting lens
wedge
mirror
probe laser
trigger detector
mirror
attenuation
mirror

Figure 4.7: Pump-probe experimental arrangement for measuring nonlinear transmission through a semiconductor sample.

Figure 4.7 shows the pump-probe experimental arrangement used for measuring the nonlinear transmission of the InP sample that I set up under the supervision of Dr. Ken McEwan. The pump beam was a 1.064μm *Nd:YAG* laser with a pulse duration of 16.1ns (FWHM) at a repetition rate of 10Hz. The probe beam was a 1.550μm cw diode laser, with its output coupled into a fibre. The pump beam could be variably attenuated by rotating a waveplate situated in front of a polariser to control the amount of energy in the reflected beam.

Two lenses were used as a X0.5 telescope to reduce the beam diameter. This was done so that the beam would be focused more weakly to ensure that the diameter of the pump beam at the sample was much greater than that of the probe beam. It needed to be larger so that the pump evenly excited the entire region of the sample being probed.

The beam was attenuated by neutral density filters before passing through an optical wedge, which produced two reflections. One of the wedge reflections went to a reference detector (all detectors were *Thorlabs DET210* models) via additional attenuation and was used to trigger the oscilloscope connected to the transmission detector (*Tektronix TDS680B*). The other reflection was monitored on a camera.

The straight-through beam and the probe beam were aligned along the same optical path. The beams then entered the sample focusing lens (f=10cm). This focused them to approximately the same place, above the translation stage where the sample was mounted. The exact focus was determined by observing the energy of the pump beam transmitted by the sample and noting when the signal reached a minimum. The minimum occurred at the point of highest intensity and, hence, smallest beam size. A lens was placed directly behind the sample in order to collect any light that may have been refracted by free carriers produced in the sample and focus it towards the detector.

The pump beam was filtered from the transmitted beam using an achromatic mirror that reflected at 1.064µm but transmitted at 1.550µm. Ideally a wavelength selective filter would have been used instead but none were available. The probe beam continued on to the second focusing lens, which focused the beam onto the transmission detector. A calibrated energy detector and energy meter (*Molectron Detector Inc. JD2000 Joulemeter ratiometer*) were used to accurately measure the energy of the beam.

The nonlinear transmission of the sample was determined by measuring the transmission of the sample with and without pumping of the material. Additional measurements were taken to remove any unreflected pump beam or electrical noise on the signal. The experiment was repeated at different pump energies.

4.3.2 Pump-probe experimental results

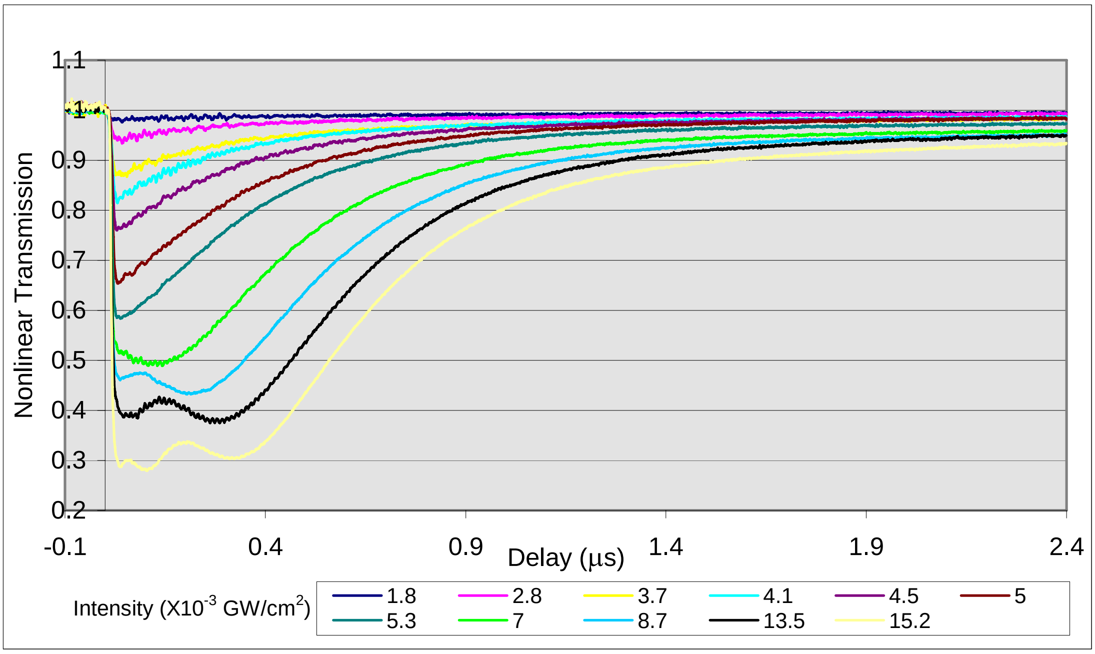

Figure 4.8: Nonlinear transmission of probe beam (1.55µm) through InP whilst being pumped at various intensities with 15ns 1.064µm pulses.

Figure 4.8 shows the results of the pump-probe experiment performed at a number of different energies. As can be seen, at each energy there was initially high transmission. The moment the pump beam hit the sample of indium phosphide the transmission reduced to a minimum. The magnitude of this reduction was highly dependent on the intensity of the pump beam. The greater the incident intensity, the larger the reduction. This is because the intensity is effectively the number of photons incident on the sample in a given area. Therefore, at higher intensities, more TPA could occur so more free carriers were produced. These in turn absorbed (and refracted) the beam, adding to the measured effect.

At higher intensities an unusual effect occurred. The measured transmission appeared to oscillate with time. It is suspected that a diffractive effect was occurring within the beam due to the large amounts of absorption and refraction, possible due to a ‘dark’ spot appearing at the high-absorption area.

As the free carriers recombine, the absorption decreases and the transmission returns to normal. According to the integral in eqn. 37 in chapter 2, which describes the change in the number of carriers with time, the decay is exponential. Therefore, it is expected that the nonlinear transmission curve will be exponential as well. Figure 4.9 shows experimental data and an exponential fit. The best fit appears to be with two exponential curves as follows:

$$\text{Fit} = 1 - 0.34e^{(-t/0.5)} - 0.063e^{(t/2.0)}$$

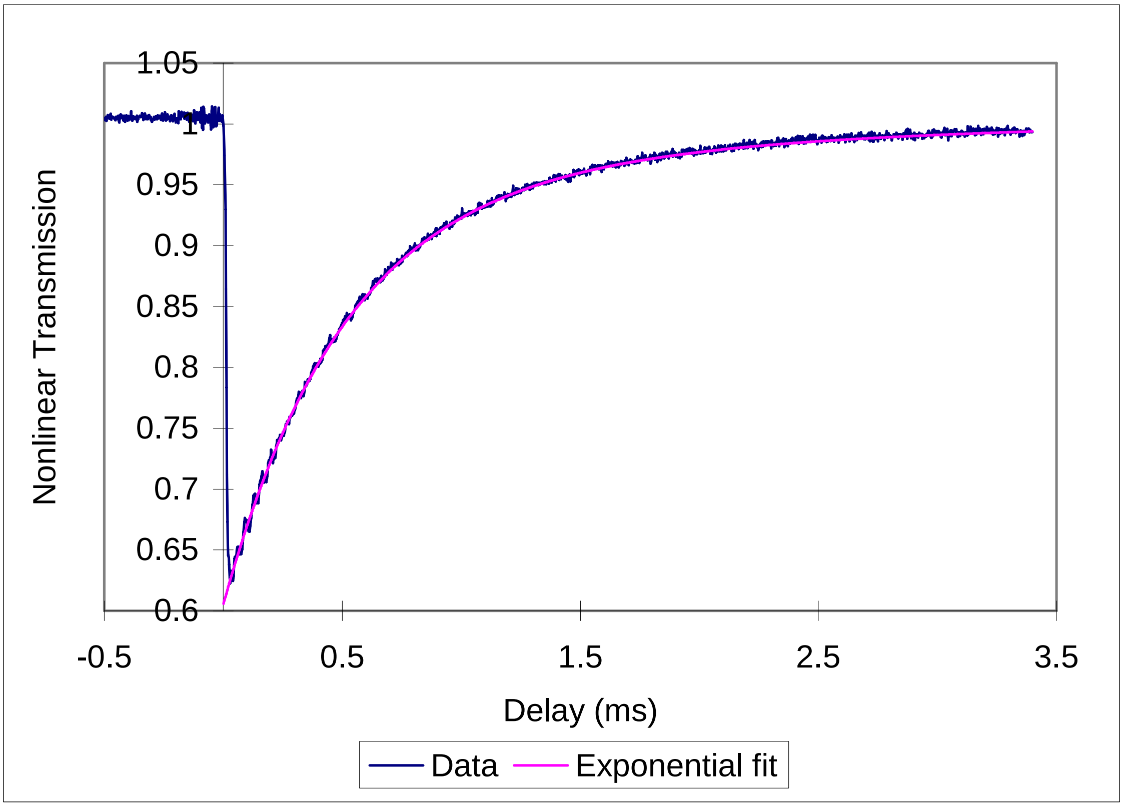

Figure 4.9: Nonlinear transmission of probe beam (1.55µm) through InP whilst being pumped at 4.8x10-3 GW/cm^2 with 15ns 1.064µm pulses.

This would suggest two different recombination mechanisms occurring over different timescales. It is unknown why this is the case and more work is required to understand fully what is happening. It should be noted that the free-carrier lifetime is much longer than the Q-switched pulse duration (~10ns) of the laser used in the experiments. Therefore free-carrier recombination can be neglected. Unfortunately, the pump-probe method does not give any idea of the amount of nonlinear refraction occurring in the sample. As it is expected that this will have a significant effect on the beam, it is important that the refraction is quantified. This was done in the z-scan experiments described in the next sections.

4.4 1.064µm and 1.534µm z-scan description and results

The following sections describe the z-scans performed on the indium phosphide at two different wavelengths – 1.064µm and 1.534µm. The results are analysed so that the two-photon absorption coefficient, free-carrier absorption coefficient and free-carrier refractive index cross-section can be extracted from the data. Finally, the main conclusions of the work are presented.

4.4.1 Experimental procedure for 1.064µm z-scans

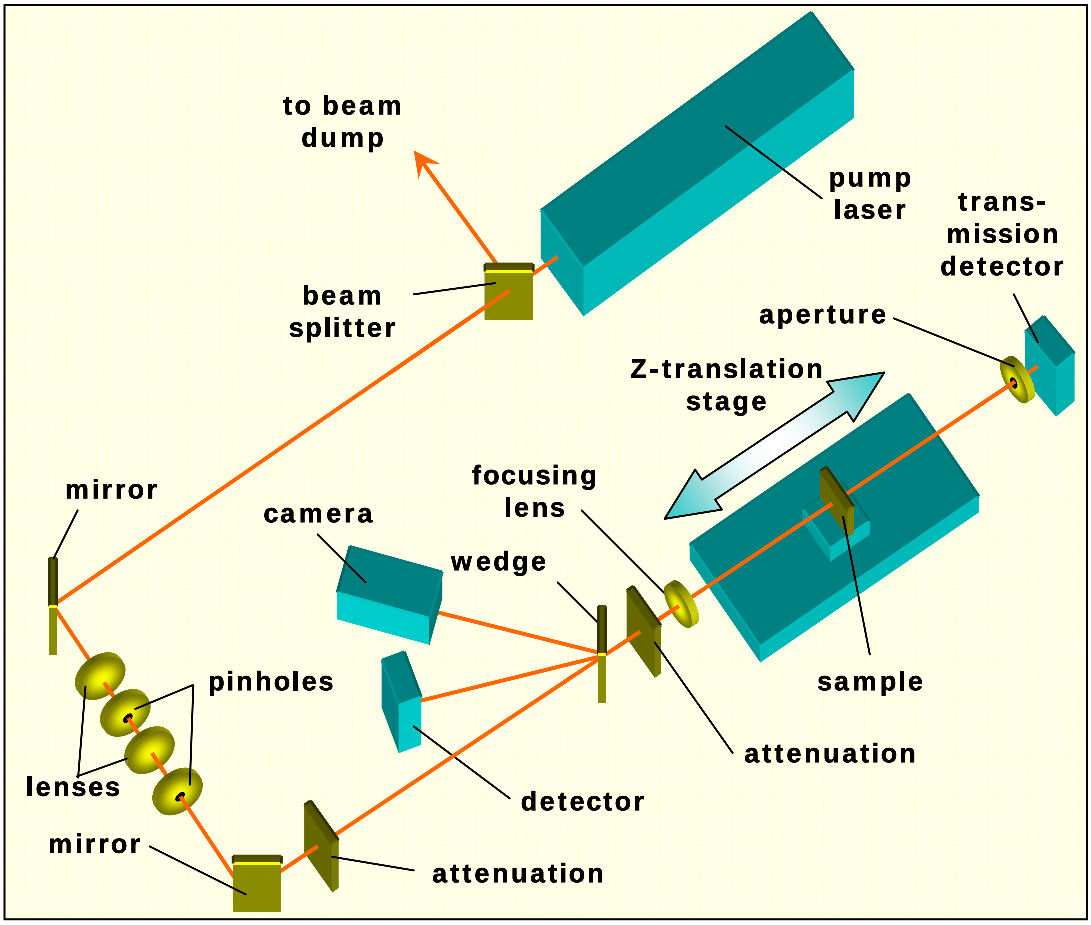
to beam dump
pump laser
trans-mission detector
beam splitter
aperture
Z-translation stage
mirror
camera
focusing lens
wedge
pinholes
sample
lenses
attenuation
detector
mirror
attenuation

Figure 4.10: Experimental apparatus for nanosecond z-scan measurements at 1.064µm.

The z-scan technique can be used to quickly determine the sign of the change in refractive index. It can also be used to determine the magnitude of this change, and, depending on the experimental conditions, the free-carrier absorption coefficient, σ_{fca}, and the two-photon absorption coefficient, β. The method requires a focused Gaussian beam arrangement and an aperture transmitting a known fraction of the incident energy.

Approximately 50% is typical, as the beam changing intensity over the aperture results in a relatively large transmission change.

Figure 4.10 shows the apparatus used for performing such a z-scan experiment. The set-up is essentially the same as that used in the characterisation experiment. Most of the energy in the beam was dumped using a beam splitter. A spatial filter was used to remove a large amount of the spatial noise on the beam. It consisted of an f=40cm lens, a 200μm pinhole and an f=30cm lens in series. The aperture was placed at the focus of the lens. A second aperture was used as an additional filter.

The beam was attenuated with a neutral density filter before passing through an optical wedge, which created two reflections. The first reflection was attenuated before going to a *Cohu 4700* camera, which was used for observing the beam. This was necessary because the beam position moved across the pinhole in the spatial filter as the laser warmed up. The image from the camera could therefore be used to ensure the beam was correctly aligned through the pinhole. The second reflection was sent to a detector*,* which was connected to an energy-meter (*Molectron Detector Inc. Opti-MUM 4001*). This acted as a reference beam.

The straight-through beam was attenuated further before being focused by an f = 20cm lens. The beam entering the lens was not collimated correctly, so the focal point of the beam was actually 16cm away from the lens. The sample was placed in a translation stage that allowed approximately 25mm of movement away from focus in either z-direction. The transmitted beam passed through a variable aperture in front of the transmission detector. For an open aperture, or full energy, z-scan, the aperture was opened fully so that the beam did not impinge on it. For a closed aperture scan the aperture was closed until approximately half of the light was transmitted. This controlled whether the experiment was sensitive to refractive effects.

Z-scans were performed at a number of different energies. In each case 16.1ns pulses of 1.064μm light were used. The indium phosphide sample was placed in the translation stage at the 0mm position. The aperture in front of the detector was closed so that it was ~2.5mm in diameter. This gave a transmission of approximately 50% each time. The InP was moved through focus and the energies of the input and transmitted pulses recorded on the detectors (the average of 100 pulses was taken). The signal data was then normalised against the reference data to remove the effect of any energy fluctuations.

When the sample had been moved through the full range of positions, an open aperture z-scan was performed by fully opening the aperture and moving the sample back along the z-axis. In this set up the detector was insensitive to any refractive effects and only the nonlinear absorption was measured.

4.4.2 Results of 1.064µm z-scans

Open z-scans:

The open z-scans were analysed first so that a value for the free-carrier absorption coefficient could be obtained. In order to do this, however, the two-photon absorption had to be known. This was measured in chapter 3 to be approximately 45cm/GW. However theory suggests a value of 22cm/GW[6] (see section 4.2.3), whilst recent measurements suggest a value of 20-35cm/GW[7,[8]]. Due to the ambiguity in the value of β values of 22, 30 and 45cm/GW were used and the results compared.

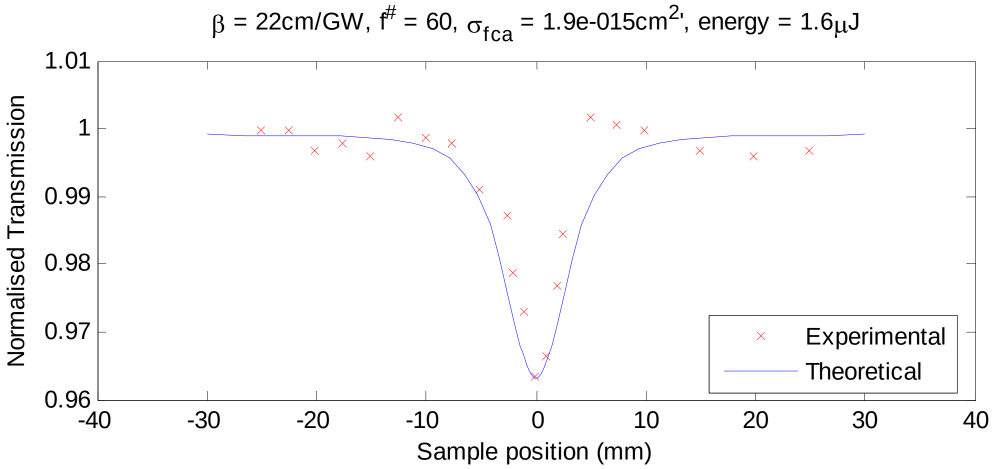

Figure 4.11: Example of a theoretical fit to the experimental data. This scan was performed on the InP sample at an energy of 1.6µJ. The fit was produced assuming a value of 22cm/GW for β, and gave a value of $19\text{x}10^{-16}\text{cm}^2$ for σ_{fca}.

In order to fit a theoretical curve to the experimental data, the known experimental parameters were entered into the modelling program (described in chapter 2) along with the value chosen for β. σ_{fca} was then adjusted until the generated curve was a close fit to the experimental data. Figure 4.11 shows an example of such a fit. This procedure was repeated at each energy level. Table 4.1 contains a summary of the findings for the 3 different βs.

Energy (µJ)	**1.29**	**1.60**	**1.82**	**2.10**	**2.34**	**2.70**
Beta = 22 cm/GW	20	19	26	41	45	68
Beta = 30 cm/GW	14	13	18	29	33	48
Beta = 45 cm/GW	9	8.3	12	19	22	32

Table 4.1: Summary of the free-carrier absorption coefficients, σ_{fca} ($x10^{-16}cm^2$), found by fitting theoretical data to experimental data produced by z-scans at different energies.

For small changes in β, the resulting change in σ_{fca} is almost inversely proportional. Hence a halving of the two-photon absorption coefficient results in an approximate doubling of the free-carrier absorption coefficient.

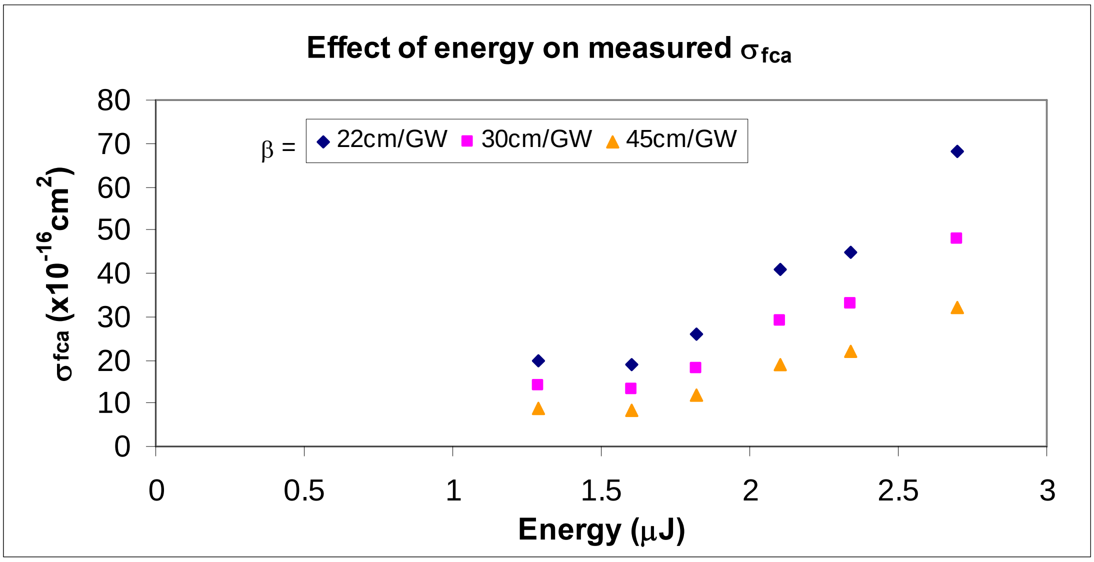

Figure 4.12: A plot of σ_{fca} vs. energy assuming three different two-photon absorption coefficients.

Figure 4.12 is a plot of the free-carrier absorption coefficients vs. energy for each of the different β values. There should be no energy dependence so the value obtained for σ_{fca} should be constant at each energy, i.e. three horizontal lines for the three β values. The graph, however, indicates otherwise as the value for σ_{fca} increases with energy. Assuming a two-photon absorption coefficient of 22cm/GW, as predicted by theory, leads to the σ_{fca} varying from a low of $19x10^{-16}cm^2$ to a high of $68x10^{-16}cm^2$ – an increase of more than 3 times. There are a number of possible explanations for this behaviour, such as detector saturation or material damage i.e. anything that leads to the assumption of an increase in absorption. The most likely explanation, however, is that the detector wasn't collecting all of the transmitted light due to nonlinear refraction in the sample causing the beam to spread. Although care was taken to avoid this by moving the detector as close to the sample stage as possible, recent work done on InAs[9] suggests that even a loss of a fraction of 1% can lead to significant fitting problems. Further evidence to suggest that this is occurring comes from the fact that as the energy is increased, the σ_{fca} increases at an increasing rate. This might be expected because an increase in energy means more free-carriers are generated which can then interact with the beam.

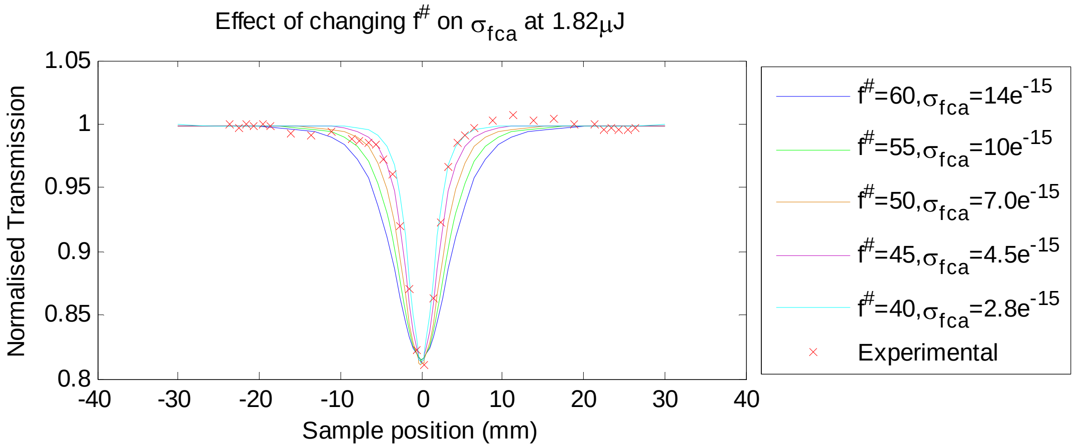

Figure 4.13: Effect of varying the $f^{\#}$ on the fits generated. As the $f^{\#}$ is reduced, the fit becomes better and the σ_{fca} required reduces.

In addition, the fits aren't perfect. The trough of the theoretical curve is consistently broader than the experimental data. The only way to correct for this is to alter the $f^{\#}$ of the optical system, as demonstrated in figure 4.13. Varying the $f\#$ effectively changes the beam size and, hence, the intensity. The $f^{\#}$ needs to be reduced to 2/3rds of its measured value in order to produce a good fit. If instead, the $f^{\#}$ is kept at its measured value, and the free carrier absorption coefficient is varied so that the theoretical and experimental curves drop at the same points, as shown in figure 4.14, the absorption coefficient required is found to be lower, at $10\text{x}10^{-16}\text{cm}^2$, as opposed to $26\text{x}10^{-16}\text{cm}^2$ obtained by fitting to the minimum of the trough. Whilst in no way does this account for any losses due to refraction, it does indicate that to obtain a good fit near the edges of the absorption dip, the free-carrier absorption coefficient must be lowered.

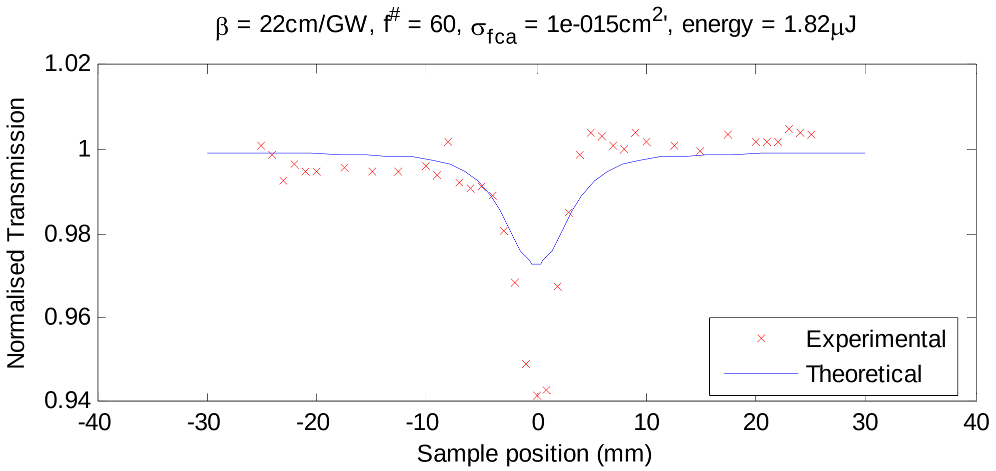

Figure 4.14: Example of fitting to the edges of the absorption dip, rather than the minimum. The required σ_{fca} is lower.

Modelling the detector as an aperture

A method was devised for checking whether the detector was collecting all of the transmitted light. The model used for calculating the closed z-scan theoretical data (see the next section) was altered so that the nonlinear absorption was zero whilst still maintaining the nonlinear refractive contribution to the transmission change. The aperture size was set to the detector-window radius (5mm) and the aperture distance was set to the focus-detector distance (205mm in the case of the 1µm data, 110mm for the 1.5µm data). The aperture transmission was set to 100% because when no refraction is occurring in the sample, the detector collects all of the light. Essentially, the detector was modelled as though it were an aperture with a diameter larger than the beam diameter at the detector.

As explained previously, the two-photon absorption coefficient was unknown, so three different values were used – 22cm/GW (20cm/GW for 1.5µm), 30cm/GW and 45cm/GW for generating the theoretical data. These were then plotted on the same chart against experimental data, for comparison purposes. This was done for each energy, an example of which is shown in figure 4.15.

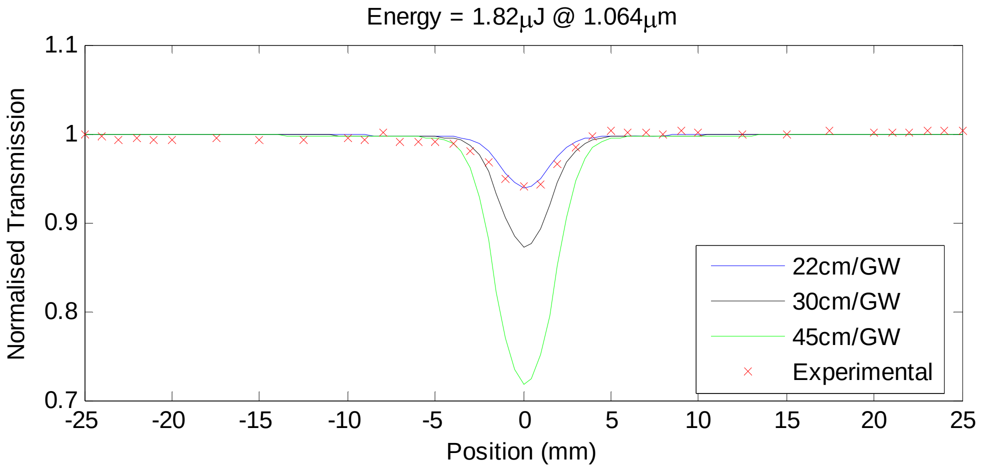

Figure 4.15: A modelled closed-aperture z-scan plotted against open-aperture data taken at 1.82μJ with 1.064μm light. The detector was modelled as though it were a 10mm diameter aperture.

The figures clearly show that there is a change in transmission. As the effects of absorption have been removed from the model, this must be due to refraction in the sample. In fact, it appears to be far stronger than the effect of the two photon and free-carrier absorption, and accounts for all of the transmission loss observed.

The only issue is that the transmission loss due to the refraction is actually too high. For example, comparing the data produced at β=22cm/GW for different energies shows that initially, the curve shows a smaller drop than the experimental data. However, as the energy is increased, the drop matches then becomes greater than the experimental drop. At 2.34μJ and 2.7μJ, the drop is actually higher than the experimental data, suggesting there is a problem somewhere. It is possible that the M^2 is affecting the results as the model assumes an M^2 of 1 (a perfect Gaussian), even though the beam was measured to have an M^2 larger than this value. It's also possible that the refractive index cross-section used, $-1\text{x}10^{-20}\text{cm}^3$, was too high. This number was used as it is what is predicted by theory (see next section).

Taking these points into consideration, an exact value of σ_{fca} cannot be determined from these results. However, the non-collection of the light results in an increase in the measured σ_{fca}, so an upper limit of $1\text{x}10^{-15}$ cm^2 can be estimated. Unfortunately there seems to be very little information reported in the literature to compare this value against. Dvorak and Justus[10] assume a value of $1\text{x}10^{-17}\text{cm}^2$, which seems reasonable considering the measured values are overestimates and are slightly larger than this. In addition, colleagues have measured the damage level in the sample of InP and, assuming the damage is due to melting caused by a temperature increase from free carrier absorption, also measure a value of the order of 1x10^{-17}cm^2[7]. Either way, the value is small and, therefore, its effect on the nonlinear refraction measurements is negligible.

Closed Z-Scans:

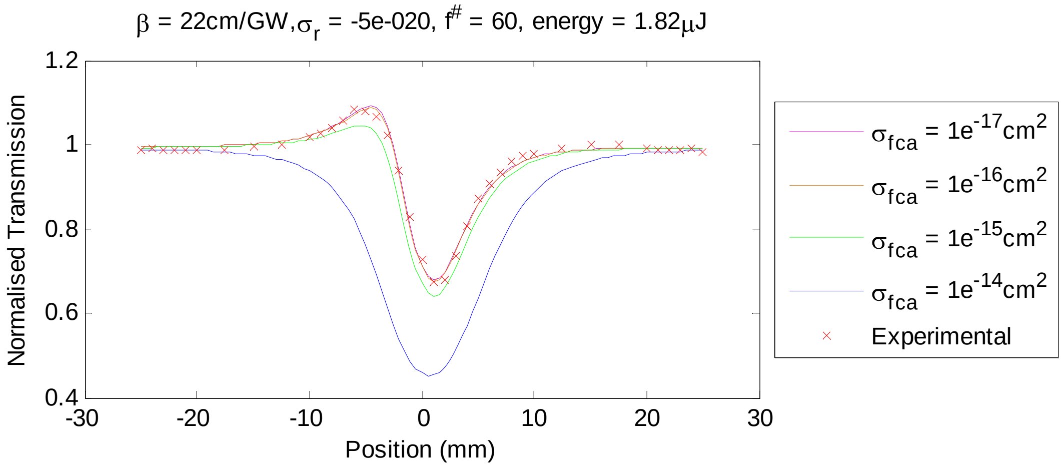

Figure 4.16: Demonstration of the effect of σ_{fca} on the experimental fits. The experimental data was taken at an energy of 1.82μJ. The fit assumes a β of 22cm/GW.

As the open scans did not produce a definitive value for the σ_{fca}, the effect of σ_{fca} on the theoretical fits generated was investigated to see how it affected the shape of the curve produced. Values of 1x10^{-14}, 1x10^{-15}, 1x10^{-16} and 1x10^{-17}cm^2 were used to generate 4 different curves. As can be seen in figure 4.16, there is very little difference between the curves generated with σ_{fca} = 1x10^{-17} and 1x10^{-16}cm^2. Only when σ_{fca} ~ 1x10^{-15}cm^2 does it have a significant effect on the fit. However, if this value is used it is difficult to generate an accurate fit to the experimental data, as the peak of the curve does not rise as high as the experimental data, and the trough is also deeper. No matter which variables are altered, this cannot be corrected. At 1x10^{-14}cm^2 the situation is even worse and it is completely impossible to generate a theoretical fit that resembles the experimental data in any way. This strongly suggests that these values are higher than the true value. Therefore, a value of σ_{fca} = 1x10^{-16} cm^2 was chosen for generating the theoretical curves. This is still higher than what is predicted by theory, but is also close to the upper limit measured in the open z-scans.

As before, the correct value for β was uncertain. So once again 3 different values for β were used – 22, 30 and 45cm/GW. Figure 4.17 shows an example of an experimental fit taken assuming β = 22cm/GW and σ_{fca} = 1x10^{-16}cm^2. It is immediately evident that the nonlinear refractive index change is negative due to the characteristic peak-valley shape (as opposed to the valley-peak shape associated with a positive change).

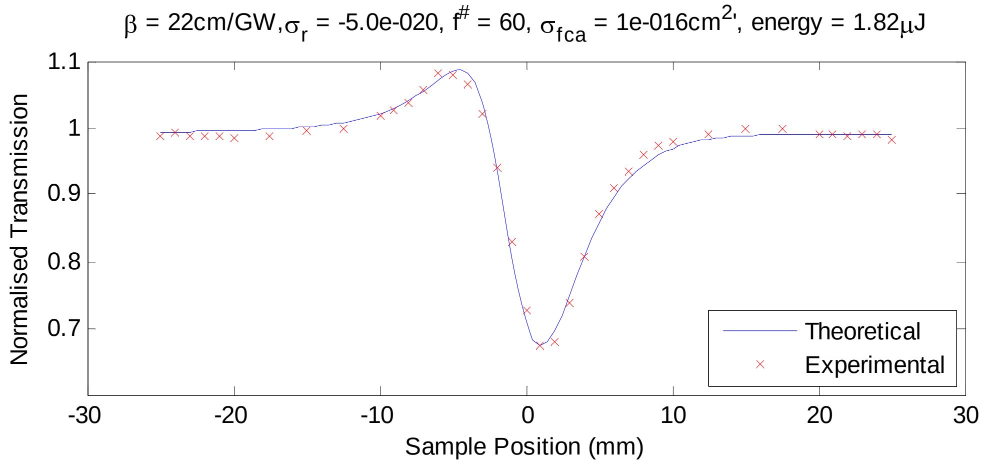

Figure 4.17: Example of a fit to a closed aperture z-scan. The energy was 1.82μJ and β and σ_{fca} were assumed to be 22cm/GW and 1x10^{-16}cm^2 respectively. The resulting σ_r is -5.0x10^{-20}cm^3.

Table 4.2 shows a summary of all of the fits to experimental data. The values obtained for σ_r are consistent suggesting that the results are independent of energy, as expected. As β is increased the σ_r decreases by a proportionate amount, suggesting that $\beta\sigma_r$ is a constant, at ~-113x10^{-20}cm^4/GW. This is because if β is increased, more charge carriers are generated for a given intensity, so each carrier needs to contribute less to produce the same total refractive change.

Energy (μJ)	**1.29**	**1.6**	**1.82**	**2.1**	**2.34**	**2.7**	**Average**
Beta = 22 cm/GW	-5.3	-5.0	-5.0	-5.5	-5.0	-5	-5.13
Beta = 30 cm/GW	-4.1	-3.5	-3.6	-3.5	-3.7	-4	-3.73
Beta = 45 cm/GW	-2.8	-2.5	-2.4	-2.4	-2.5	-2.5	-2.52

Table 4.2: Summary of the free-carrier refractive index, σ_r (x10^{-20}cm^3), cross-sections found by experimental data produced by z-scans at different energies. σ_{fca} was assumed to be 1x10^{-16}cm^2.

At β = 22cm/GW (from theory), the values obtained are approximately 6 times those predicted by Auston's equation (-0.8x10^{-20}cm^3)[11] and approximately 5 times those predicted by Wherrett's (-1.2x10^{-20}cm^3)[12]. If a higher β is used, the measured σ_r

values approach the values obtained from theory, suggesting that β might by higher than predicted by theory.

As with the femtosecond measurements the uncertainty is difficult to measure. However, following the same principles, and taking into account the variation of the measurements with energy, an error of ± 1 x 10^{-3}cm^3.

The theoretical values are approximations with their accuracy determined by how many carrier effects are included. Some of the main contributions to the refractive index change come from the plasma (free carrier) effect, thermal effects and band filling. The Auston formula assumes that most of the refractive change comes from the plasma effect (Drude formula) but a modification to account for the effect of band filling near resonance is included, which fails when the photon energy is very close to the bandgap energy. Wherrett's formula is valid over all photon energies, but tends to give higher values than the other formulae.

4.4.3 Experimental procedure for 1.534µm z-scans

In order to investigate the nonlinear effects at a longer wavelength, an OPO was constructed to generate light at 1.534µm (see fig. 4.18). The pump source was the same 1.064µm Nd:YAG laser used in the previous measurements.

As before a wedge was used to create two reflections, one for monitoring the beam on a camera, the other for monitoring the beam on an energy meter. This would act as a reference during the z-scans.

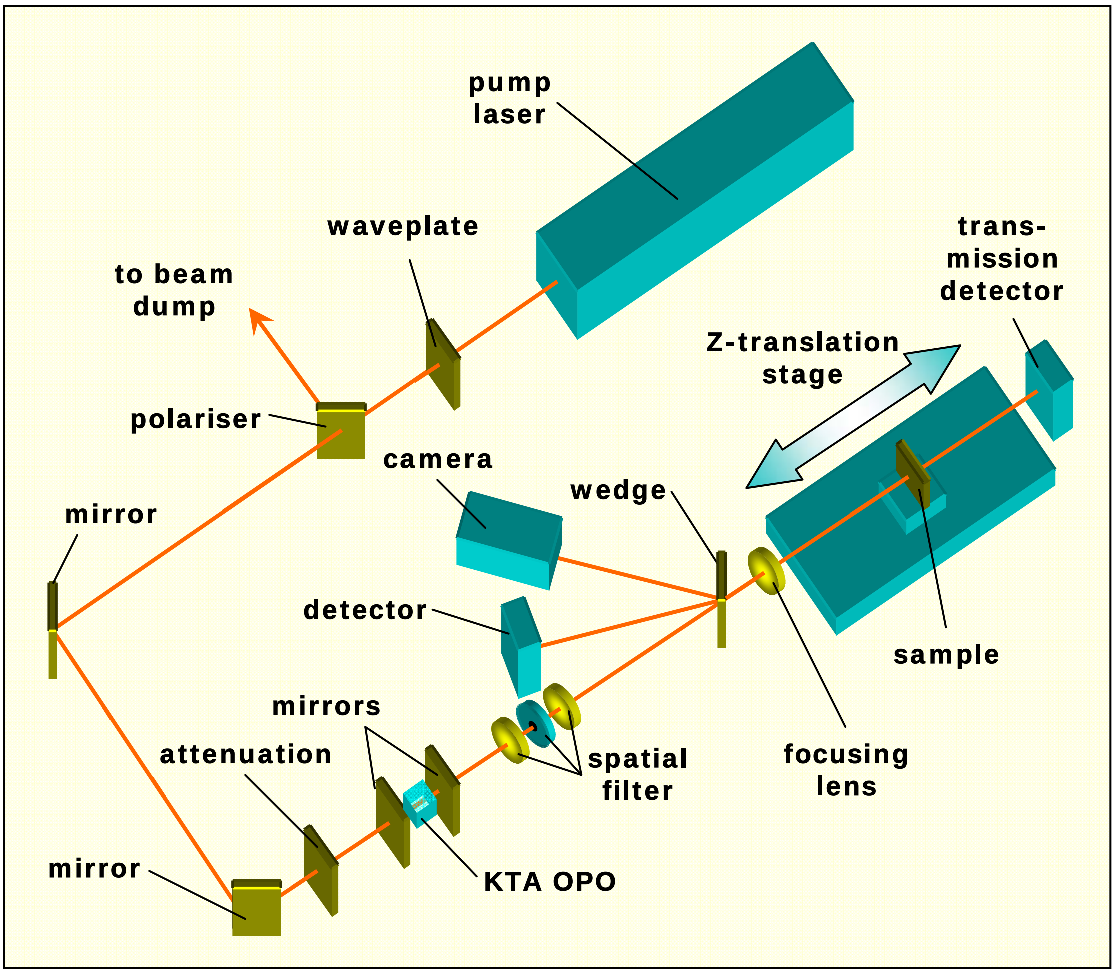
pump laser
waveplate
to beam dump
trans-mission detector
Z-translation stage
polariser
camera
wedge
mirror
detector
sample
mirrors
attenuation
spatial filter
focusing lens
mirror
KTA OPO

Figure 4.18: Experimental apparatus for nanosecond z-scan measurements at 1.534µm.

Open and closed aperture z-scans were conducted at various energies by scanning the sample along the z-axis of the beam and measuring the transmitted energy. Neutral density attenuators were used to vary the input beam energy.

For the closed scan experiments, the energy was measured with the aperture fully-open and approximately half-closed. This gave the aperture transmission, which would be necessary for the fitting program. Once again the transmission detector was placed as close as possible to the translation stage, so that any refracted light would be collected.

4.4.4 Results of 1.534µm z-scans

Open and closed z-scans were performed at various energies at 1.534µm. The results of these experiments are described below.

Open Z-Scans

As with the 1.064µm data, the open z-scans were analysed first in order to try to determine the σ_{fca}. Figure 4.19 shows a fit to the experimental data taken at 4.36µJ, and a summary of the results obtained by fitting the other data sets is shown in table 4.3.

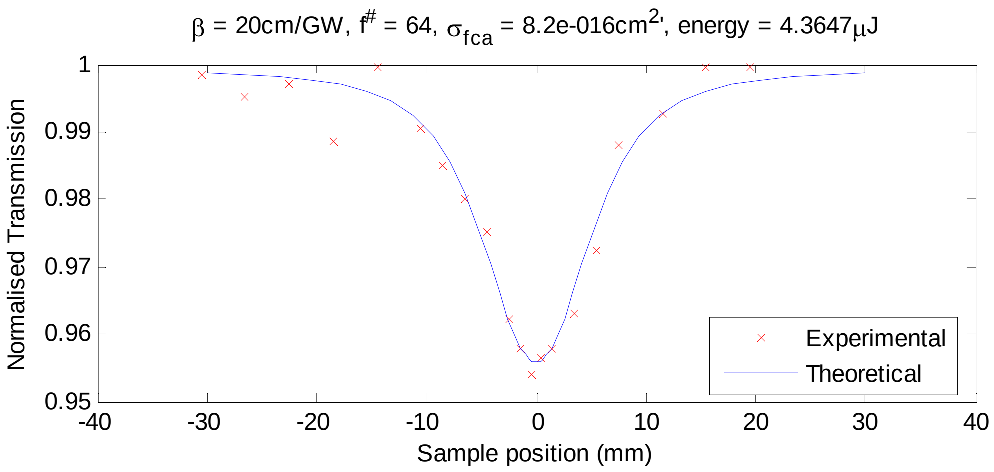

Figure 4.19: A typical fit to the experimental data collected with an input energy to the sample of 4.36µJ. Assuming a β of 20cm/GW produces a σ_{fca} of 8.2x10^{-16}cm^2.

Energy (µJ)	**4.36**	**5.61**	**6.44**	**8.22**
Beta = 20 cm/GW	8.2	8.6	11	12.5
Beta = 30 cm/GW	5.2	5.6	7	8
Beta = 45 cm/GW	3.2	3.6	4.4	6

Table 4.3: Summary of all σ_{fca} (x10^{-16}cm^2) obtained from the 1.534µm open z-scan measurements.

As seen with the 1.064µm data, σ_{fca} appears to increase with energy. Doubling the energy causes the σ_{fca} to increase by approximately 50%. The σ_{fca} is lower overall, with a minimum of 3.2 x 10^{-16}cm^2 at β = 45cm/GW.

Closed Z-Scans

The closed z-scan data was analysed in the same way as the closed scan data taken at 1.064μm. Figure 4.20 shows an example fit and table 4.4 shows a summary of the fits to all of the z-scans. In general the fits were not as good as those obtained with the 1.064μm data. This is most likely due to the poorer beam quality associated with the pulses generated by the OPO. The theoretical curve sits higher than the experimental data and the centres of the peak and trough are not aligned. This can be alleviated somewhat by increasing the $f^{\#}$ slightly along with a small increase in σ_r. Obviously this is a deviation from what was measured experimentally; but it nevertheless suggests that beam quality may be an issue.

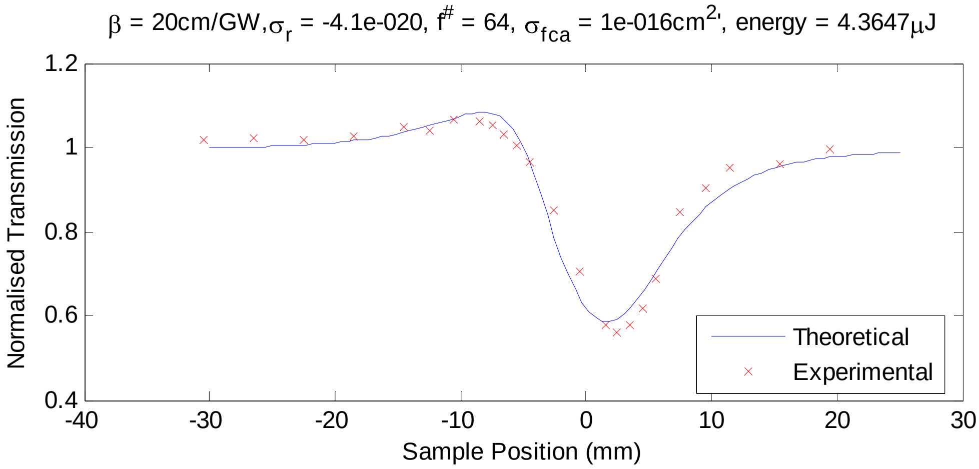

Figure 4.20: Example of a closed aperture z-scan fit at 4.36μJ. β and σ_{fca} were assumed to be 20cm/GW and $1\text{x}10^{-16}\text{cm}^2$ respectively. The best fit occurs with a σ_r of $-4.1\text{x}10^{-20}\text{cm}^3$.

Energy (μJ)	2.89	4.36	5.61	6.59	7.72	Average
Beta = 20 cm/GW	-4.4	-4.1	-4	-4	-4.2	-4.14
Beta = 30 cm/GW	-2.7	-2.7	-2.8	-2.8	-3	-2.8
Beta = 45 cm/GW	-1.8	-1.9	-1.8	-1.8	-2	-1.86

Table 4.4: Summary of all σ_r ($\text{x}10^{-20}\text{cm}^3$) obtained from the 1.534μm closed z-scan measurements.

Table 4.4 contains a summary of all of the closed aperture results. Once again the numbers generated are consistent for different energies, suggesting there is no energy dependence as was observed with the open scans. As before, if the value chosen for β is increased, the σ_r required for a good fit decreases. Again, $\beta\sigma_r$ is a constant; this time at ~-83.5x10^{-20}cm^4/GW. Assuming a value of 20cm/GW for β gives a σ_r of ~-4x10^{-20}cm^3. This is 5-6 times the theoretical value of Auston's formula (-0.7x10^{-20}cm^3) and 3-4 times that of Wherrett's formula (-1.0x10^{-20}cm^3). Following the same principles as before, the uncertainty in $\beta\sigma_r$ is estimated to be ± 30x10^{-20}cm^4/GW. This gives an error in σ_r of ~1x10^{-20}cm^3 assuming a β of 30cm/GW.

Comparing between the two wavelengths, the theoretical values at 1.064μm (-0.8x10^{-20}cm^3 for Auston and -1.2x10^{-20}cm^3 for Wherrett) are 1.2 and 1.24 times the theoretical values at 1.534μm. The experimental values scale almost perfectly to this, with the 1.064μm value of -5.13x10^{-20}cm^3 being 1.24 times the 1.534μm value of -4.14 x10^{-20}cm^3. The values are represented in figure 4.21.

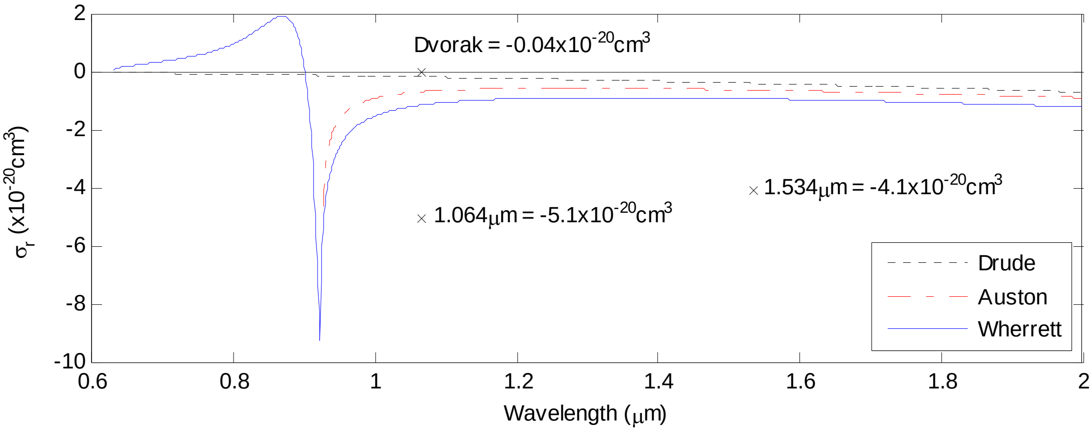

Figure 4.21: σ_r values determined experimentally at 1.064μm and 1.534μm plotted against a value from the literature[10] and theoretical estimates[11,12].

4.5 Conclusions

This chapter has described the measurement of the free carrier absorption coefficient, σ_{fca}, and the free-carrier refractive index cross-section, σ_r, in a sample of 1mm thick bulk indium phosphide at 1.064µm and 1.534µm.

The free-carrier refractive index cross-sections were found to be -5.1x10^{-20}cm^3 at 1.064µm and -4.1x10^{-20}cm^3 at 1.534µm, assuming a β of 22cm/GW and 20cm/GW respectively, as suggested by theory. Both these values are ~5 times the values predicted by an approximate theoretical model, but they scale with wavelength in the same way as the theoretical predictions. This suggests that the predicted value for β may be lower than in reality.

A major problem was encountered whilst analysing the open aperture data in that σ_{fca} was found to vary with energy. It is strongly suspected that this is due to refraction in the sample spreading the beam so that not all of the light is collected by the detector. This lost light appears as a transmission drop and cannot be distinguished from the transmission drop associated with two-photon absorption and free-carrier absorption in the sample. Therefore, higher σ_{fca} values are required in order to generate theoretical data that fits the experimental data, making the measured σ_{fca} much higher than predicted.

Future work may involve bonding the InP directly to the detector. This should eliminate the problem of not collecting all of the light so that refraction can be ignored. However, this technique may introduce problems of its own. One example would be that the detector would have to be scanned through the focal point of the beam. Therefore the detector would have to be resistant to high-intensity damage, whilst being sensitive enough to measure the beam energy away from focus keeping noise to a minimum. It would also have to be able to cope with the beam size varying over the detector area.

4.6 References

1. A.E. Kaplan, “External self-focusing of light by a nonlinear lens” *Radiophys. Quantum Electron.* **12** p692 (1969)
2. S.A. Akhmaanov, R.V. Khoklov, A.P. Sukhorukov, *Laser Handbook,* **2**, p1151 Eds. F.T. Arecchi and E.O. Shultz-Dubois, (North-Holland, Amsterdam, 1972)
3. E.W. Van Stryland, M.A. Woodall, H. Vanherzeele, M.J. Soileau “Energy band-gap dependence of two-photon absorption” *Opt. Lett.* **10** p490 (1985)
4. Z. Hang, H. Shen, F.H. Pollak, “Temperature-dependence of the E0 and E0 + delta-0 gaps of InP up to 600-degrees-C” *Solid-State Commun.* **73** p15 (1990)
5. Y.P. Varshni, *Physica (Netherlands)* **34** p149 (1967)
6. G.D. Pettit, W.J. Turner, “Refractive index of InP” *J. Appl. Phys.* **36** p2081 (1965)
7. T. Sloanes, P.K. Milsom, K.J. McEwan, M.B. Haeri, T.O. Clatterbuck, J. McCartney, H. Bookey, A.K. Kar, “Two-photon induced free-carrier absorption and refraction in indium phosphide”, *To be submitted to J. Appl. Phys.*
8. D. Vignaud, J.F. Lampin, F. Mollot,”Two-photon absorption in InP substrates in the 1.55µm range” *Appl. Phys. Lett.* **85(2)** p239 (2004)
9. M.B. Haeri, S.R. Kingham, P.K. Milsom, “Nonlinear absorption and refraction in InAs” *J. Appl. Phys.* **99** 013514 (2006)
10. M.D. Dvorak, B.L.Justus, “Z-scan studies of nonlinear absorption and refraction in bulk, undoped InP” *Optics comms.*, **114** p147 (1995)
11. D.H. Auston, S McAffee, CV Shank et al., "Picosecond spectroscopy of semiconductors" *Solid State Electron,* **21** p147 (1978)
12. B.S. Wherrett, A.C. Walker, F.P. Tooley, *Optical Nonlinearities and Instabilities in Semiconductors*, Ch10. Ed. Hartmut Haug (Academic Press, 1998)

5 Nanosecond Measurements in Cadmium Mercury Telluride

5.1 Introduction

This chapter details my attempts to measure the free-carrier absorption and refraction in CMT, and compares the results to estimates from theory. To do this, two different samples of CMT are investigated using z-scans, which allow the nonlinear refraction and absorption to be measured. The compositions of the samples were unknown initially, so the material was characterised before any experiments took place. This is shown in section 5.2, along with calculations of estimates from theory. The characterisation of the laser used in the z-scan experiments is also described in this section. Next, section 5.3 details the z-scan experiments followed by the results and analysis of those experiments in section 5.4. This is done for both samples. Finally, the main conclusions of the experiments are discussed in section 5.5, and a list of references concludes the chapter in section 5.6.

5.2 Beam and material characterisation

This section of the chapter contains characterisation details of the laser beam used in the z-scans and of the CMT itself. The same 1.534µm beam used for measuring the nonlinearities in the piece of indium phosphide was used here, so it did not need to be re-characterised. However, for the sake of readability, the results are summarised here.

5.2.1 Beam characterisation

The beam was previously characterised in chapter 4, section 4.2.2, where full details of the characterisation can be found. The M^2 was determined to be 1.03 and the $f^{\#}$ of the system was 64.

5.2.2 Cadmium mercury telluride characterisation

The CMT samples were obtained from Selex, Southampton (UK). They were then optically polished and given a broadband anti-reflection coating at Qinetiq, Malvern (UK). The sample thicknesses were measured using a vernier calliper to be 0.60 ± 0.05mm for CMT1 and 1.05 ± 0.05mm for CMT2.

Little was known about the optical specifications of the samples, other than that their bandgaps were quoted as 1.4µm (which will be referred to as CMT1 from here-on) and 1.5µm (CMT2) by the manufacturer. To ensure that this was the case their transmission spectra were measured using the same spectrometer as that used for measuring the InP transmission spectrum. Figure 5.1 shows the spectra produced. The change from absorbing to transmitting is gradual. The transmission of the first sample, CMT1, changes between 1420nm and 1475nm whilst for the second piece the change occurs between 1520nm and 1580nm. As discussed with the indium phosphide it is difficult to use this data to measure the actual bandgap. In that case, the onset of transmission occurred approximately 25nm beyond the bandgap measured by others in the literature[1,2]. If the same is assumed here, then the bandgaps would correspond almost perfectly to what was quoted by the manufacturers, i.e. 1.4µm and 1.5µm. Therefore, those values will be assumed to be correct in the following analysis to determine the x fraction and the linear refractive index.

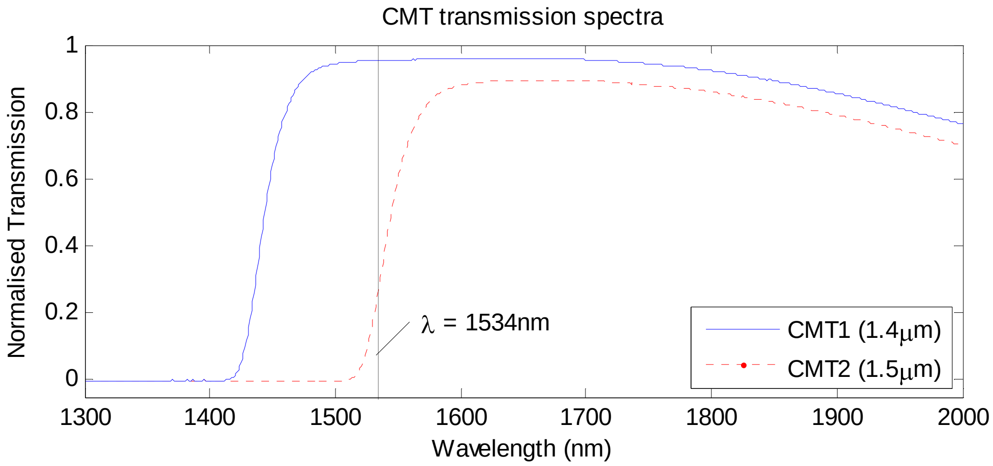

Figure 5.1: Transmission spectra of the two CMT samples. Sample 1 has its absorption edge at ~1420nm (0.873eV) whilst the absorption edge of sample 2 is at ~1520nm (0.816eV).

The wavelength of the laser beam used in the experiments was 1534nm. In the case of CMT1, this was sub-bandgap, so no linear absorption occurred. For the second sample, however, the laser wavelength lay directly on the band-edge, so a combination of linear and nonlinear absorption occurred. Although this made it difficult to extract any nonlinear parameters from the measurements, the experiments were, nevertheless, useful as they suggest a technique for enhancing the nonlinear absorption and refraction processes.

In order to determine theoretical values for the two-photon absorption coefficient, β, and the free-carrier refractive index cross-section, σ_r, in the $Cd_xHg_{(1-x)}Te$, the linear refractive index, $n(\lambda)$, has to be known. An empirical formula exists[3] relating x to $n(\lambda)$. However, the compositions of the two samples are also unknown. Fortunately, various formulae exist for determining how the energy gap varies with temperature and composition, allowing the composition to be calculated. Ref. 4 contains a review of these studies.

The most widely used formula is that of Hensen et al.[5]. It is:

$$E_g(\mathrm{eV}) = -0.302 + 1.93x - 0.81x^2 + 0.832x^3 + 5.35(1.2x)10^{-4}T \tag{1}$$

This equation was tested for $x = 0.0 - 0.6$, and $x = 1.0$.

A more recent study was conducted by Laurenti et al.[6] for x values of 0.5 – 1.0. Their formula is:

$$\begin{aligned} &E_g(\text{eV}) = -0.313(1-x) + 1.606x - 0.132x(1-x) + \\ &\left[6.3(1-x) - 3.25x - 5.92x(1-x)\right]\left(10^{-4}T^2\right)/\left[11(1-x) + 78.7x + T\right] \end{aligned} \tag{2}$$

Legros and Triboulet[7] performed measurements using material with similar x values (0.7 – 1.0) and obtained:

$$E_g(\text{eV}) = -0.313 + 1.984x - 0.654x^2 + 0.579x^3 + \left(5.5 - 13.92x + 5.84x^2\right)10^{-4}T \tag{3}$$

According to the manufacturers and the transmission spectra in figure 5.1, the two samples of CMT have their band-edges at 1400nm and 1500nm, or 0.878eV and 0.818eV respectively. Using these bandgaps, the x compositions of the two CMT samples can be determined using eqs. 1-3, assuming a temperature of 300K (see table 5.1).

With the x compositions known, the formula in ref. 3 (eqs. 4 & 5) allows the linear refractive indices of the two samples to be determined at a given wavelength, λ (µm).

$$n(\lambda)^2 = A + \frac{B}{1-(C/\lambda)^2} + D\lambda^2 \tag{4}$$

with

$$\begin{aligned} A &= 13.173 - 9.852x + 2.909x^2 \\ B &= 0.83 - 0.246x - 0.0961x^2 \\ C &= 6.706 - 14.437x + 8.531x^2 \\ D &= 1.953\text{x}10^{-4} - 0.00128x + 1.853\text{x}10^{-4}x^2 \end{aligned} \tag{5}$$

Table 5.1 shows a summary of the calculated x values and refractive indices. There is a difference of 7-8% between the x values calculated using the Laurenti and Hansen formulae, which corresponds to a 2-3% difference in the refractive indices. Legros' formula produces a value close to the average of the other two. Because of this it was decided that the average values should be used. This yields $n = 2.95$ and $x = 0.683$ for sample 1 (1.4μm), and $n = 3.00$ and $x = 0.649$ for sample 2 (1.5μm).

		Bandedge = 1.40μm		Bandedge = 1.50μm	
Author	**Equation**	**x**	**n**	**x**	**n**
Hansen	1	0.707	2.91	0.672	2.96
Laurenti	2	0.656	2.99	0.626	3.04
Legros	3	0.685	2.94	0.650	3.00
Average	-	0.683	2.95	0.649	3.00

Table 5.1: Summary of the x compositions and refractive indices of $Cd_xHg_{(1-x)}Te$ determined by bandgap at 300K.

Using the above parameters in equation 1 in ref. 8 gives $\beta = 87$cm/GW at 1.4μm and $\beta = 91$cm/GW at 1.5μm. This agrees fairly well with values measured by John McCarthy, a student on placement at Dstl from Heriot-Watt university. He measured the two-photon absorption coefficient to be approximately 70cm/GW [9], although this value was determined by scaling

Before σ_r can be estimated, the effective electron and hole masses need to be determined. These can be estimated now that the composition of the material is known.

An excellent review of research on these parameters can be found in chapter A6.3 of ref. 4. Unfortunately, most of the carrier masses are measured with x values between 0 and 0.3, and at temperatures <100K. However, Laurenti et al report results calculated using an empirical formula based on a simple 3-band **k**.**p** perturbation theory, which is valid over all x values and temperatures. Their results are reported in Table V of ref 6. Reading from this table at 300K for $x = 0.68$ (CMT1) gives a conduction band electron effective mass of $0.059m_0$. Similarly, at $x = 0.65$ (CMT2) the effective mass is reported as $0.055m_0$ (where m_0 is the free electron mass).

According to Kane's theory the light-hole effective mass is predicted to be the same as the electron mass. This is discussed by Long and Schmit[10], and the measurements of Weiler[11] seem to confirm this.

The heavy-hole effective mass has been measured by many workers (again see ref. 4). Unfortunately most of the measurements were made at low x values (0.15-2.0) and there is a large dispersion between the reported values, ranging from $0.28m_0$ to $0.7m_0$. The author of ref. 4 is of the opinion that the results of Weiler [11] are the most accurate as they used magneto-optical techniques (requiring no assumptions of E_g) to measure m_{hh} values of $0.40m_0$, $0.49m_0$ and $0.53m_0$ for the [001], [110], [111] crystal orientations respectively (x = 0.175-0.269). Gold and Nelson[12] later determined that the ratio of the above results to the light-hole effective mass agreed well with the ratio expected from elementary semiconductor theory.

As with the indium phosphide, the formulae of Auston [13] and Wherrett [14] (see chapter 2) were used to calculate σ_r. For CMT1, σ_r was found to be $-4.1\text{x}10^{-20}\text{cm}^3$ and $-5.3\text{x}10^{-20}\text{cm}^3$ respectively, assuming the heavy-hole effective mass to be $0.4m_0$.

Similarly, for CMT2, the values were found to be $-31\ \text{x}10^{-20}\text{cm}^3$ and $-14\ \text{x}10^{-20}\text{cm}^3$. This is significantly larger than the other sample because the photon energy is extremely close to the material bandgap, where both formulae predict the refractive cross-section to increase rapidly. It should be noted however that Auston's formula fails as the photon energy becomes very close to the bandgap energy, and so it's questionable whether it should actually be used in this case. Table 5.2 shows a summary of all the material parameters of the two CMT samples.

Sample	CMT1	CMT2
x	0.683	0.649
E_g(μm)	1.4	1.5
E_g(eV)	0.878	0.819
n	2.94	3
m_c	0.059	0.055
m_{hh}	0.4	0.4
m_{lh}	0.059	0.055
β (cm/GW)	87	91
Auston σ_r ($\text{x}10^{-20}\text{cm}^3$)	-4.1	-31
Wherrett σ_r ($\text{x}10^{-20}\text{cm}^3$)	-5.3	-14

Table 5.2: Summary of the material parameters of the two CMT samples used in the z-scans.

5.3 Z-Scan description and results

The following sections explain how the nonlinearities in the CMT were measured using z-scans, and the results that were obtained are analysed.

5.3.1 Experimental procedure

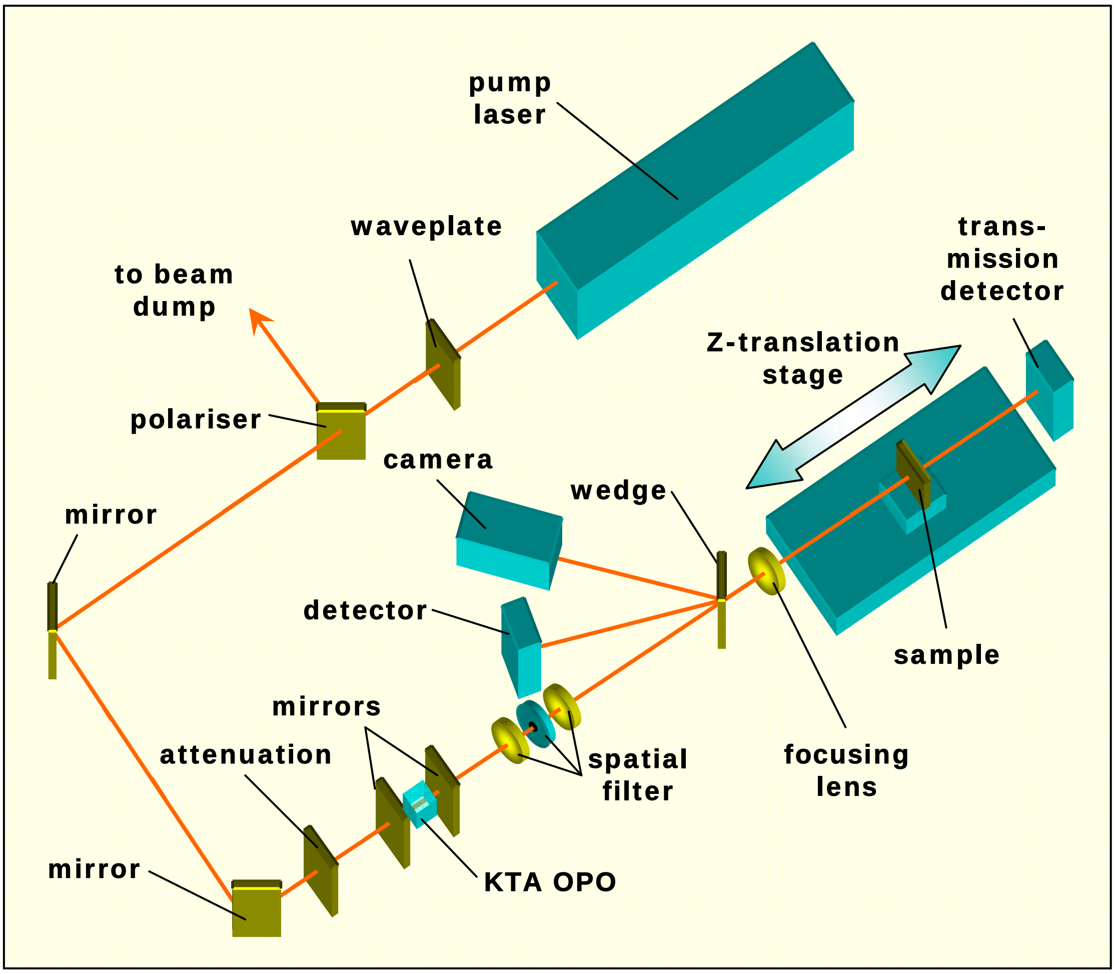
pump
laser
waveplate
to beam
dump
polariser
mirror
camera
wedge
trans-
mission
detector
Z-translation
stage
detector
sample
mirrors
attenuation
spatial
filter
focusing
lens
mirror
KTA OPO

Figure 5.2: Experimental apparatus for nanosecond z-scan measurements at 1.534µm.

As with the indium phosphide experiments at 1.534µm, open and closed aperture scans were conducted at various energies. For the open scans the energy incident on the detector with no sample present was measured with the aperture fully open to allow the z-scan data to be normalised. For the closed scans the energy was also measured with the aperture transmitting ~50% of the energy. This allowed the transmission of the aperture to be measured. The sample was then inserted and the z-scan carried out. The half-closed aperture with no sample measurement allowed the closed z-scan data to be normalised.

The z-scans were repeated for both pieces of CMT. The results of the z-scans on CMT1 are described and discussed in section 5.3.2 and the experiments performed on the second piece, CMT2, in section 5.4.

5.3.2 Results of z-scans on CMT1 (1.4µm band-edge)

Both open and closed z-scans were performed on the piece of CMT with its bandgap at 1.4µm (CMT1). The open z-scan results are discussed first and the closed z-scan results follow.

Open Z-Scans

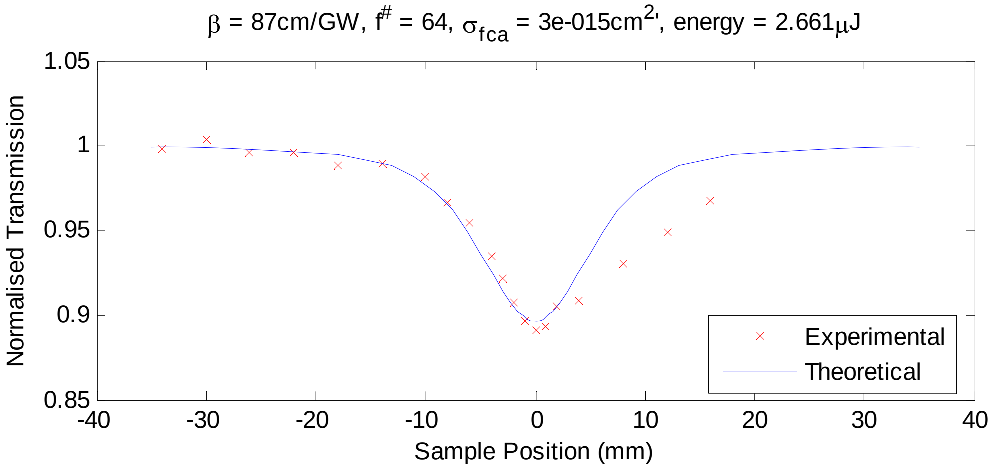

Figure 5.3: Example of a fit (line) to open z-scan experimental data (x's).

Figure 5.3 shows a typical fit to the experimental data. The fit was generated using the Matlab program described in chapter 2. The experimental and material parameters were input into the program and the generated data was plotted alongside the experimental data. This was repeated at a number of different energy levels. In general the fits weren't as good as with the indium phosphide experiments using the same 1.534µm beam. This is partly because the pulse energies used were lower (apart from the 6.19µJ data), so detector noise became more pronounced.

Energy (µJ)	**2.51**	**2.66**	**3.82**	**6.19**
σ_{fca} (x10^{-15}cm^{2})	1	3	1	9

Table 5.3: Summary of all σ_{fca} found by fitting to open z-scan experimental data at all energies.

Table 5.3 shows a summary of all the σ_{fca} values obtained from the fits at different energies. As seen with the indium phosphide experiments, the values found for σ_{fca} are very high. Again this is almost certainly due to refraction occurring within the sample, causing the beam to spread until its diameter is larger than the detector window. Because part of the beam is not collected, the measured energy is lower giving the impression of an absorptive effect. This effect would be expected to increase with energy, because at higher energies more free-carriers are generated so more free-carrier absorption and refraction can occur. This is evident in the table above, with the highest energy scan having the highest measured σ_{fca}.

Because of this, the value of ~$3\text{x}10^{-15}\text{cm}^2$ obtained above is almost certainly an overestimate, and should be considered as an upper limit.

Closed z-scans

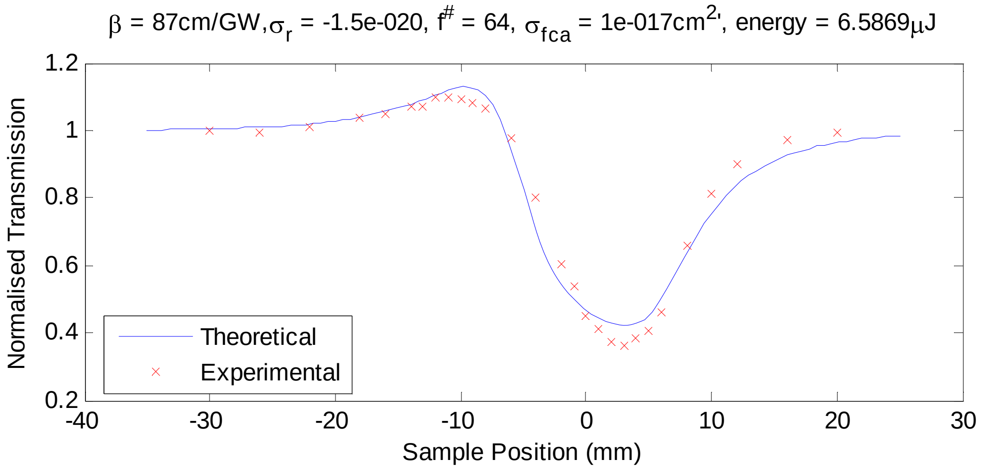

Figure 5.4: Example of a fit to closed aperture z-scan data taken at 6.59μJ.

Figure 5.4 shows an example of a closed aperture z-scan and the fit produced by the modelling program described in chapter 2. β was assumed to be 87cm/GW, which was obtained from theory[6] earlier in this chapter. σ_{fca} was assumed to be $1\text{x}10^{-17}\text{cm}^2$. This is lower than the overestimates obtained from the analysis of the open z-scans, but agrees with the value estimated for other semiconductors, such as InP[15]. As shown in the case of the indium phosphide, σ_{fca} actually has very little effect on the fit because the beam spreading associated with the nonlinear refraction dominates the transmission changes measured.

Energy (μJ)	**4.36**	**5.61**	**6.59**	**7.72**	**Average**
σ_r (x10^{-20}cm^3)	-2	-1.5	-1.5	-1.7	-1.7

Table 5.4: Summary of all σ_r found by fitting to closed z-scan experimental data taken at all energies.

Table 5.4 contains a summary of all of the σ_r values found from fitting the closed aperture z-scans performed at each energy. The uncertainty is estimated at ± 0.7x10^{-20}cm^3. There is reasonably close agreement between the values measured at different energies, with the average value being -1.7x10^{-20}cm^3. As shown earlier, theory predicts values of -4.1x10^{-20}cm^3 and -5.3x10^{-20}cm^3 so the experimental value obtained is 2-3 times smaller than the theoretical ones. Whilst not ideal, this is fairly close. It's possible that the value for β is incorrect as no experimental values could be found at this particular x value. If the value used was too high, σ_r would have to be increased to compensate.

The next section describes the experiments performed on the second piece of CMT.

5.4 Results of z-scans on CMT2 (1.5µm band-edge)

It was intended that the above experiments would be repeated on the second piece of CMT with its band-edge at 1.5µm. Unfortunately, the strong linear absorption (~75%) meant that the transmitted signal was very low – close to the sensitivity limits of the detector. Because closed z-scans require the presence of an aperture that reduces the energy even further, it was difficult to perform them without the noise becoming too great, so only one scan was performed. However it was possible to perform open z-scans over a range of energies. The linear absorption also meant that the fitting programs had to be modified before being used to fit the experimental data. The reason for this is that the linear absorption generates free-carriers in the material, in much the same way as the two-photon absorption does. To account for this a linear absorption coefficient, determined from the linear transmission, was added to the carrier generation equations in the models.

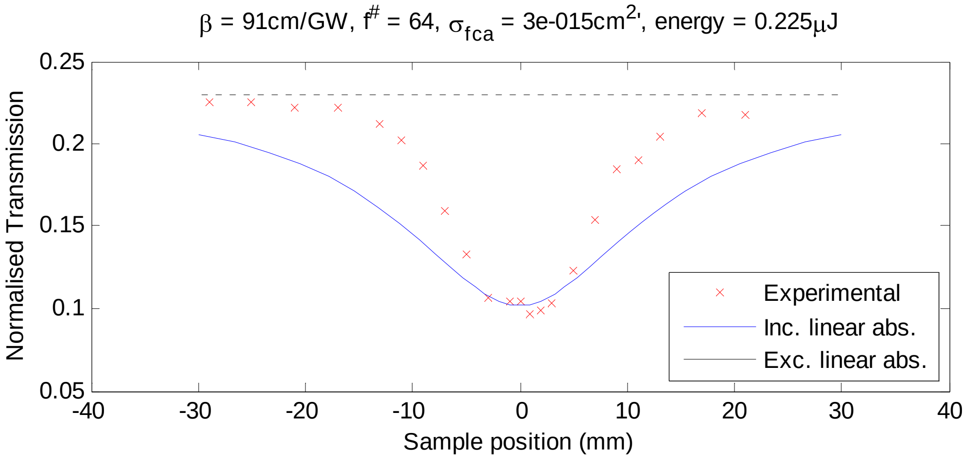

Figure 5.5: Example of an open aperture z-scan on sample CMT2. The beam energy was 0.22µJ. The data was fitted with and without linear absorption present.

Figure 5.5 shows a fit to an open z-scan performed at 0.22µJ. The transmission drop is relatively large, at just over 50%. In comparison, fig. 5.3, which shows the results of an open z-scan performed on the CMT1 sample at a higher energy (2.66µJ), shows a transmission drop of around only 10%. All of the experimental parameters other than the energy were kept the same. Therefore the transmission drop due to nonlinear processes is five times as strong at only a tenth of the energy. Using the updated model, σ_{fca} was found to be $3\text{x}10^{-15}\text{cm}^2$, which is of the same order of magnitude as seen with the other materials. Generating a fit assuming no linear absorption, the model did not show a transmission drop at the energy used in the scan, again suggesting that the linear absorption has a large effect on the resulting nonlinear processes. Table 5.5 shows a summary of all the σ_{fca} values found using different energies.

Energy (μJ)	**0.225**	**0.45**	**1.6**	**2.5**
σ_{fca} (x10^{-15}cm^2)	3	4	6	8

Table 5.5: Summary of all σ_{fca} values.

As seen with the indium phosphide and the other CMT sample, σ_{fca} varies with energy. As discussed earlier, this is most likely because nonlinear refraction is contributing to (and even dominating) the transmission loss associated with the absorption measured in the z-scans. However, it's obvious that this sample gives a much stronger nonlinear effect than the previous CMT sample at a given energy.

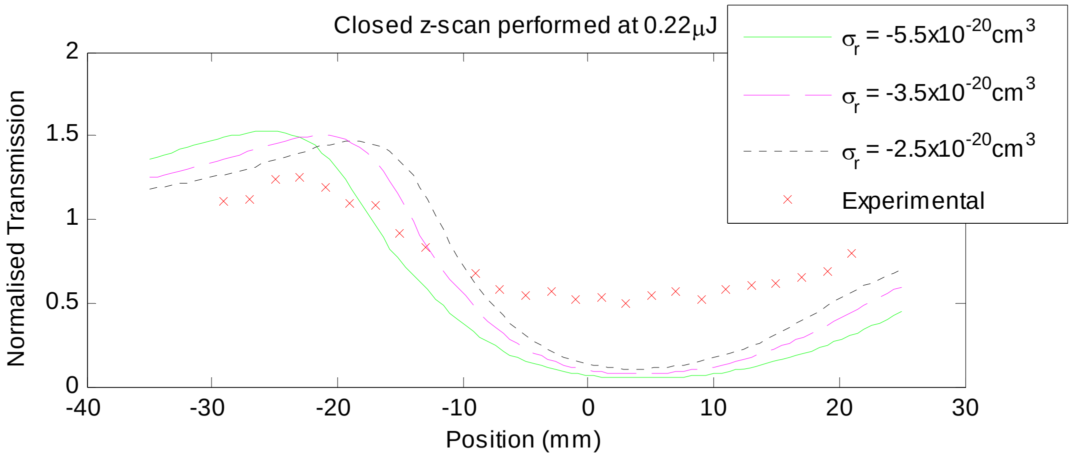

Figure 5.6: Example of a closed aperture z-scan on sample CMT2. As in figure 1.5, the beam energy was 0.22μJ. Due to the poor fit, a number of σ_r variations have been plotted.

A better idea of the enhancement can be obtained by comparing the closed z-scans performed on the two materials, as they fully take account of the absorption and refraction occurring. Figure 5.6 shows the results of a closed z-scan at the same energy as that used in the open z-scan in fig. 5.5. The data has been normalised to remove the transmission loss associated with the linear absorption. The scan is rather spread out compared to the CMT1 scans (see fig. 5.4). This is due to refraction occurring further away from focus, which could only be caused by either the intensity or the nonlinear refraction being stronger than in the previous case. Since the experimental parameters were kept the same between the two samples, it must be the refraction that has increased. Comparing to the fit in fig. 5.4, the energy used is 30 times less, yet the transmission change from maximum to minimum is about the same at 60%. Again this suggests that there has been an enhancement of the nonlinear refraction in the material. The significant difference between the two samples is the energy gap. In the CMT2 experiments, the laser wavelength lies directly on the bandgap. Therefore, as discussed earlier, a combination of linear and nonlinear absorption occurs. This means that a greater population of free carriers can be generated at a given intensity, which can then absorb and refract the beam, just as occurs with the two-photon generated carriers.

The updated model was used to generate a fit to the experimental data because of the linear absorption. However, it proved difficult to get a good fit, so a number of fits were plotted with σ_r values ranging from -2.5 to -5x10^{-20}cm^3. These values give curves similar in shape to the experimental one, but the magnitude of the transmission change is larger. It may be that the model is not accounting for the effect of the linearly generated carriers correctly. For the closed z-scan experiments, the model treats the sample as a ‘thick slice’, and averages the number of carriers generated over the width of the material. In reality, the number of carriers will vary throughout the sample, with more being generated near the front surface than at the back because the intensity is stronger there.

The values calculated using the formulae of Auston and Wherret (-14 and -31x10^{-20}cm^3 respectively – see section 5.2.2) are approximately 6 and 12 times larger than the experimental value. As CMT is an alloy semiconductor, it’s possible that the material is not homogenous, instead containing areas of varying concentrations of Cd and Hg (i.e. the x value changes). If this was the case, the largest effect would be near the bandgap, where the theoretical formulae vary rapidly with x composition. It’s also possible that the bands are no longer parabolic, instead having tails due to defects in the crystal.

This significant increase in the nonlinear effects resulting from the linear absorption is useful in regards to transmission controlling applications, where nonlinear processes are used to reduce peak intensities, preventing damage to optical components or suppressing energy spikes. For example, nonlinear processes in semiconductors have been used to improve the stability of a passively mode-locked laser[16]. Another application might be in an OPO for reducing the pulse duration – if the CMT is placed in an OPO cavity, once the power level inside reaches a certain threshold, the nonlinear absorption and refraction will increase reducing the Q of the cavity and stopping the OPO from working.

One negative aspect is that the high linear absorption would result in high insertion losses if placed in an optical system, reducing the energy of any transmitted pulses. Also, the material only works for a small range of wavelengths (±10nm). Fortunately, the bandgap of CMT can be altered by changing the composition of the material. Therefore the material composition could be optimised so that only a small amount of linear absorption occurred for a specific wavelength source, whilst still generating enough carriers to produce a large nonlinear effect. It is planned to investigate what amount of linear absorption is required to produce a significant improvement in the nonlinear absorption and refraction, whilst keeping linear losses to a minimum. This will be done using a tuneable laser, rather than obtaining lots of CMT samples having slightly different compositions, as tuning the wavelength offers more control of where the laser wavelength lies relative to the band-edge.

5.5 Conclusions

The nonlinear free-carrier effects in cadmium mercury telluride ($Cd_xHg_{(1-x)}Te$, or CMT) have been investigated using open and closed z-scans at 1.534µm. Two samples with different compositions were studied – one with a band-edge at 1.4µm (CMT1), the other at 1.5µm (CMT2). With CMT1, the laser wavelength is sub-bandgap so the only free-carrier generation mechanism is two-photon absorption. The generated free carriers then absorb and refract the beam. In the second sample the laser wavelength lies directly on the band-edge, so a combination of both linear absorption and two-photon absorption occurs. The linear transmission is only around 22%, so significant linear absorption occurs. Because of this, more free-carriers are generated, leading to an enhancement of the nonlinear refraction.

As was the case with the indium phosphide measurements, the free-carrier absorption coefficient could not be measured accurately due to refractive effects causing the beam diameter to become larger than the transmission detector. The non-collection of the light results in a reduction in the measured transmission, leading to the incorrect deduction that the absorption has increased. An upper limit of around $1x10^{-15}cm^2$ can be assumed, but the actual value is probably much lower than this, at around $1x10^{-17}cm^2$.

The nonlinear refractive index cross-section of the first CMT sample was measured to be $-1.7x10^{-20}cm^3$. This compares reasonably well with the $-4.1x10^{-20}cm^3$ and $-5.3x10^{-20}cm^3$ calculated from theory.

When the sample of CMT with its band edge at 1.5µm was illuminated with the 1.534µm laser, a combination of linear and nonlinear absorption was observed. The linear absorption produced more free carriers than in the case of the 1.4µm band-edge material leading to an increase in the amount of refraction seen at a given energy. This improvement obviously came at the expense of linear transmission, but because the composition of CMT can be altered, it should be possible to optimise the bandgap to produce a significant improvement in the nonlinear processes at a transmission loss that would be acceptable for fixed line applications.

5.6 References

1. Y P. Varshni, *Physica (Netherlands)* **34** p149 (1967)
2. Z. Hang, H. Shen, F.H. Pollak, "Temperature-dependence of the E0 and E0 + delta-0 gaps of InP up to 600-degrees-C" *Solid-State Commun.* **73** p15 (1990)
3. K. Liu, J. H. Chu, and D. Y. Tang, "Composition and temperature dependence of the refractive index in $Hg_{(1-x)}Cd_xTe$", *J. Appl. Phys.* **75** p4176 (1994)
4. P. Capper (Ed), Properties of Narrow-Gap Cadmium-Based Compounds, Institution of Engineering and Technology, London (1994), ISBN 0-85296-880-9
5. GX. Hansen, JX. Schmit, T.N. Casselman, "Energy gap versus alloy composition and temperature in $Hg_{1-x}Cd_xTe$", *J. Appl. Phys.* **53** p7099 (1982)
6. J.P. Laurenti, J. Camassel, A. Bouhemadou, B. Toulouse, R. Legros, A. Lusson, "Temperature dependence of the fundamental absorption edge of mercury cadmium telluride", *J. Appl. Phys.* **67** p6454 (1990)
7. R. Legros, R. Triboulet, "Photoluminescence of Cd-rich $Hg_{1-x}Cd_xTe$ alloys (0.7<x<1)", *J. Cryst. Growth* **72** 264-269 (1985) with erratum in *J. Cryst. Growth* **74** p468 (1986)
8. E.W. Van Stryland, M.A. Woodall, H. Vanherzeele, M.J. Soileau "Energy band-gap dependence of two-photon absorption" *Opt. Lett.* **10** p490 (1985)
9. J McCarthy, "Nonlinear optical effects in Bulk InP and CMT semiconductors and organic molecules", *Unpublished MSc. dissertation* University of St. Andrews (2007)
10. D. Long, J.L. Schmit, Semiconductors and Semimetals Vol. 5, Academic. Press (1970)
11. M.H. Weiler, Semiconductors and Semimetals Vol. 16, Academic Press (1981)
12. M.C. Gold, D.A. Nelson, "Variable magnetic field Hall effect measurements and analyses of high purity, Hg vacancy (p-type) HgCdTe", *J. Vac. Sci. Techno A.* **4** p2040 (1986)
13. D.H. Auston, S. McAffee, C.V. Shank, E.P. Ippen, O. Teschke," Picosecond spectroscopy of semiconductors " *Solid State Electron* **21** p147 (1978)
12. B.S. Wherrett, A.C. Walker, F.P. Tooley, *Optical Nonlinearities and Instabilities in Semiconductors*, Ch10. Ed. Hartmut Haug (Academic Press 1998)
15. M.D. Dvorak, B.L. Justus, "Z-scan studies of nonlinear absorption and refraction in bulk, undoped InP" *Optics Comms.* **114** p147 (1995)

16. P. Černý, G. Valentine, D. Burns, and K. McEwan, “Passive stabilization of a passively mode-locked laser by nonlinear absorption in indium phosphide” *Opt. Lett.* **29** p1387 (2004)

6 Nonlinearities in Photonic Crystal Fibres

6.1 Chapter summary

This chapter describes frequency conversion of a mode-locked Nd:YVO_4 laser in nonlinear photonic crystal fibres. Nonlinear frequency conversion of efficient near-infrared laser sources is of interest for many applications. However the motivation behind this work is the generation of a multi-wavelength or broadband laser source that can be used for the spectral identification of objects of military interest.

Frequency conversion in photonic crystal fibres (PCFs) can occur through nonlinear optical processes that depend on the fibre length, design, laser power and pulse duration. Different effects become dominant as the fibre and laser properties are changed. In the experiments described in this chapter, Stimulated Raman Scattering, self-phase modulation, four-wave mixing and other nonlinear effects have been observed.

By exploiting four-wave mixing within the fibre, a power transfer efficiency of 14% from 1064nm to 894nm, and 9% from 1064nm to 1314nm has been demonstrated. An investigation of the spectral output of the fibre showed that many nonlinear processes occurred within the fibre. The optimum length was found to be approximately 30m for four-wave mixing. Beyond this length the four-wave mixing conversion efficiency did not increase significantly, with most of the power being transferred into a supercontinuum.

Under certain conditions frequency conversion of the laser source into the supercontinuum was an efficient process. Approximately 70% of the input power could be transferred to a wavelength range spanning 1100-1380nm. The supercontinuum was spectrally very flat and the laser-fibre system was very stable with regard to spectral-power output. The discovery of the supercontinuum led to a similar fibre being used in an out-door trial to remotely identify different materials.

6.2 Introduction

This chapter describes the use of nonlinear processes in photonic crystal fibres (PCFs) as a means of shifting radiation at 1064nm into wavebands not available with standard laser sources. This is of interest to the UK MoD for a number of applications. These include near-infrared target illumination for use with image intensifiers, eye-safe laser operation for target ranging / designation and broadband illumination for multi-spectral imaging. In addition, the MoD has an interest in techniques that will enable multi-function laser-sources to be developed.

The majority of optical fibres are made of silica, which has low nonlinear coefficients so is a poor material for nonlinear conversion processes. However, because fibres (and, therefore, interaction lengths) can be very long, it is possible to observe relatively strong frequency conversion effects.

In the experiments described here, PCFs are used rather than standard fibres. PCFs have a larger refractive index difference between the cladding and core so a greater proportion of light is confined to the core than would be with a standard telecommunication fibre. This increases the radiation intensity and makes PCFs particularly useful for observing nonlinear effects. More importantly, the zero-group-velocity dispersion (ZGVD) point can be designed to match the laser wavelength by tailoring of the PCF structure. The laser pulses propagate without broadening temporally, which enhances the nonlinear optical effects by maintaining the high intensity along the length of the fibre. These effects contribute to producing a larger effective nonlinear coefficient, allowing strong frequency conversion with either shorter fibres with lower loss, or longer fibres pumped at lower power levels.

Most of the previous work on frequency conversion in PCFs has used pulses of femtosecond duration due to the very high intensities that can be obtained. In this study, however, pulses having durations of 10s of picoseconds are used. This is advantageous because these laser systems are generally more compact, stable and are more easily scaled to higher power levels.

The fibres used are detailed in the next section and the nonlinear processes that are observed are explained in section 7.3. The experimental design and laser sources used are described in detail in the experimental section, 7.4. The results with fibres designed for four-wave mixing and supercontinuum generation are described in section 7.5. Finally the summarised results and conclusions are presented in section 7.6 with suggestions for further work. The detailed spectra from the four-wave mixing experiments are included in appendices 6-A to 6-D.

6.3 Photonic crystal fibres

There are two major types of photonic crystal fibre – one has a solid core as shown in fig. 6.1 and the other has a hollow core. The structure of a hollow core fibre leads to a photonic bandgap being formed that confines the light to the core, guiding it. Since the core generally contains either air or is evacuated, nonlinear effects are extremely small. This makes these fibres very useful for applications where high powers or ultrashort pulses need to be guided without nonlinear effects.

In the experiments described here, photonic crystal fibres with solid cores are studied[1]. These fibres are fabricated by stacking a series of capillaries inside an outer jacket as a preform. This is reduced to small dimension using a standard fibre pulling tower. The central solid core is formed using a solid glass rod rather than a capillary at the centre. The holes give the cladding layer an effective refractive index that is much lower than the core and light is strongly confined within through total internal reflection. The high degree of confinement increases the intensity of the light compared to if the same light was travelling through a standard fibre. Consequently, these fibres readily exhibit strong nonlinear effects that include self-phase modulation (SPM), four-wave mixing (FWM) and stimulated Raman scattering (SRS). All of these effects are described in detail in the next section.

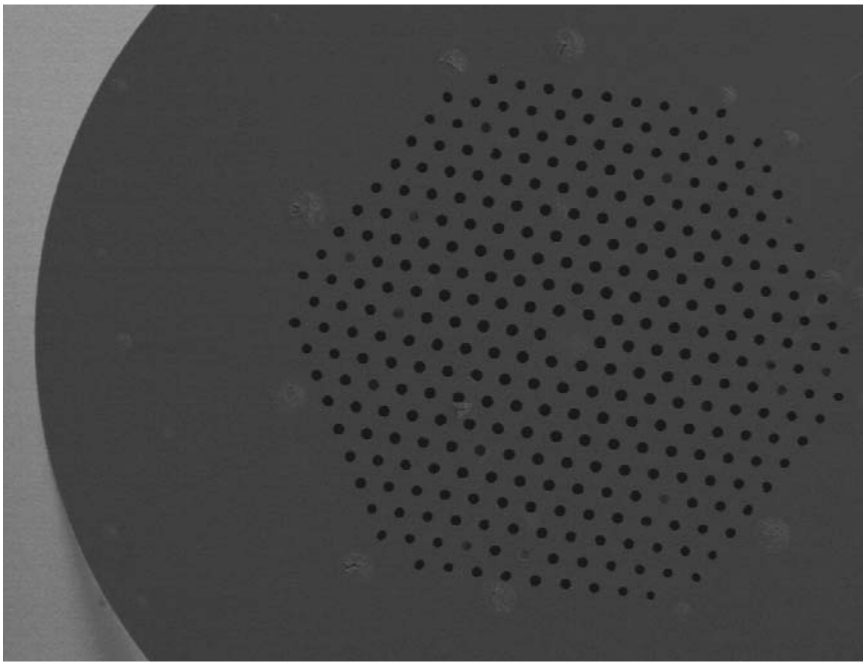

Figure 6.1: Scanning electron micrograph of the fibre used for supercontinuum generation.

A further benefit of micro-structured fibres is the ability to control the zero dispersion wavelength. As mentioned above, the nonlinearities in the fibre are dependent upon the intensity of the light passing through the medium. Chromatic dispersion reduces this intensity so it is desirable to minimise it, especially at the pump wavelength. In standard fibres the zero-group velocity dispersion point (ZGVD) cannot be shifted below 1270nm – the ZGVD of bulk silica. In PCFs, however, by careful design of the cladding structure the ZGVD can be shifted to much shorter wavelengths and even into the visible spectral region.

In this report two different PCF fibres having ZGVDs at 810nm and 1070nm are studied. The pump wavelength at 1064nm is in the normal dispersion region for one fibre (ZGVD = 1070nm) and in the anomalous dispersion region for the other fibre (ZGVD = 810nm).

Figure 6.2 shows the attenuation and dispersion profiles of the 1070nm ZGVD fibre. The large absorption peak around 1380nm is due to absorption by the OH-bond in water molecules present in the fibre.

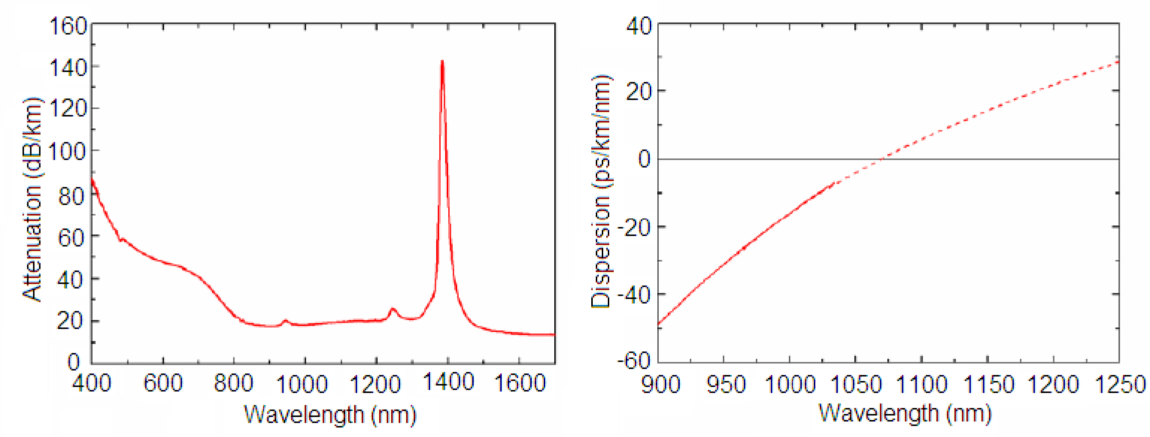

Figure 6.2: Fibre losses and dispersion profile[2].

6.4 Frequency conversion in PCFs

There are a number of frequency conversion processes possible in PCFs. Those observed in this work include self-phase modulation, four-wave mixing (FWM) and stimulated Raman scattering and the subsequent cross-coupling between these effects.

Self-phase modulation leads to spectral broadening of pulses and supercontinuum generation. It is a manifestation of the fibre material's intensity-dependent refractive index. The front edge of an optical pulse experiences a refractive index that is increasing (positive n_2) and the wavelength is red-shifted. The trailing edge of the pulse experiences a refractive index that is dropping and the wavelength is blue shifted. It occurs when short, intense laser pulses interact with the fibre material, in this case silica. It is thought that this will be less important with the picosecond pulses studied here than with the inherently more intense femtosecond pulses used in most literature studies.

Four-wave mixing (FWM) is a parametric process which occurs when photons from one or more waves are annihilated and new photons are created at different frequencies, such that the net energy and momentum are conserved [3]. This is illustrated in equations 1 and 2.

$$2k_{pump} = k_{signal} + k_{idler} + 2P\gamma \tag{6}$$

$$2\omega_{pump} = \omega_{signal} + \omega_{idler} \tag{7}$$

where k_j are the wavevectors of the modes, ω_j are the frequencies of the signal and idler waves, P is the peak pump power and γ is the nonlinear coefficient of the fibre, given by:

$$\gamma = \frac{2\pi n_2}{\lambda A_{eff}} \tag{8}$$

where n_2 is the nonlinear refractive index, λ is the pump wavelength and A_{eff} is the effective area of the fibre.

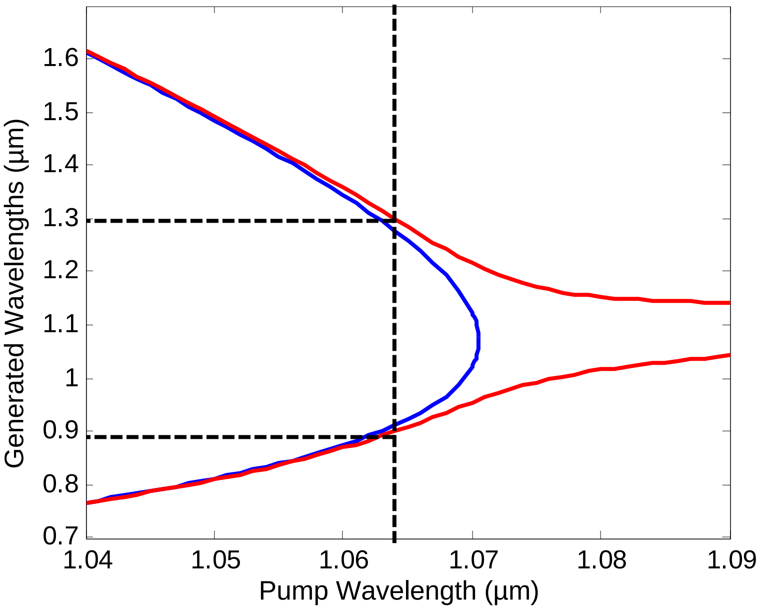

Figure 6.3: Phase-matching diagram calculated for P = 0 (blue curve) and for P = 500W (red curve).

Figure 6.3 shows the phase-matching diagram for pump powers of 0 and 500W. This was calculated using the material parameters by Laurent Michaille. At the pump wavelength, 1064nm, the fibre used in the experiments described below (ZGVD = 1070nm) is phase-matched to parametrically generate wavelengths at ~900nm and ~1310nm. Therefore it is expected that new signals will be generated at these wavelengths as power is transferred from the pump through FWM. The new signals build up spontaneously from noise, but the conversion process can be enhanced by seeding the fibre at one of the generation wavelengths. This is expected to improve the efficiency and is studied as part of this work.

Stimulated Raman Scattering [4] is a process that transfers power from one optical field to another and can occur in any molecular medium. It can be described quantum mechanically as the scattering of a photon by a molecule to a lower energy photon, leaving the molecule in an excited state. It is normally associated with vibrational excitation modes. The new-frequency radiation is called the Stokes wave with the shift in frequency being determined by the medium. In the case of fused silica the shift is

~13THz, but because the material is amorphous the Raman-gain peak is quite broad. With a pump wavelength of 1064nm, this would correspond to a Raman-shifted peak occurring at 1115nm.

Finally, if the fibre is pumped in the anomalous dispersion regime (i.e. where the chromatic dispersion, β_2 is negative), as is the case for the supercontinuum fibre with ZGVD = 810nm, then soliton formation can occur as the pulses are inhibited from spreading spectrally. The soliton can then undergo self-frequency shifting[5,6] to longer wavelengths resulting in a broadened pulse and leading to supercontinuum generation.

6.5 Experimental method

A large number of photonic crystal fibre (PCF) experiments reported in the literature use femtosecond pulses to generate supercontinua through self-phase modulation. See, for example, refs. 7-10. The work reported here concentrates on the study of a PCF with a ZGVD at 1070nm pumped with 27ps pulses at 1064nm (peak power ~1kW). The aim of the experiment was to exploit four-wave mixing within the fibre, generating new wavelengths above and below the pump wavelength.

The experimental set-up is shown in figure 6.4 below. The Nd:YVO_4 laser generates a train of mode-locked pulses at 250MHz at a wavelength of 1064nm. These were used to pump the PCF and the output was measured using an optical spectrum analyser (OSA). The maximum average power available was approximately 7W, resulting in a peak power of approximately 1kW. The optical isolator / polariser pair and quarter waveplates were used to prevent back-reflections that may otherwise have disrupted the mode-locking or damaged the laser and also to control the power entering the fibre. In addition, a diode laser was used to seed the fibre with approximately 30μW of laser radiation at 1310nm in order to enhance the four-wave mixing process occurring within the fibre.

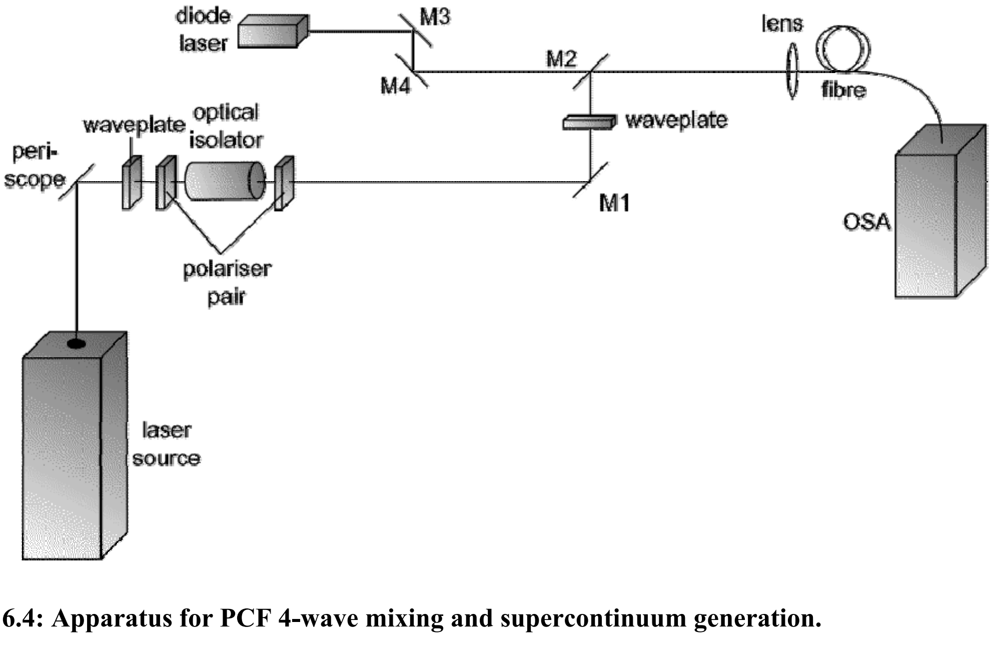

Figure 6.4: Apparatus for PCF 4-wave mixing and supercontinuum generation.

Both lasers were coupled into the fibre using a common microscope objective lens (N.A. of 0.3). A maximum coupling efficiency of 60% for the pump was achieved. The output of the fibre being pumped was then coupled via free-space into a single-mode fibre for input into the OSA.

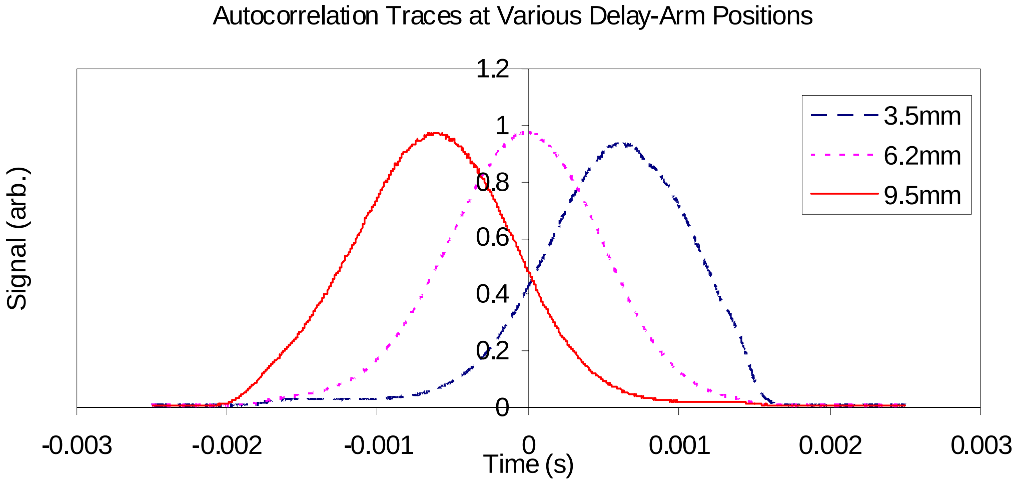

Figure 6.5: Autocorrelation trace for the pump beam.

The pulse duration was measured using a commercial autocorrelator (Femtochrome) and the result is reproduced in figure 6.5. The multiple traces show the signal measured at the extremes of the autocorrelation delay. The multiple traces are used to calibrate the temporal response and thereby extract the pulse duration. The following relation is used:

$$T / t = 2x / 0.3s \text{ (ps/ms)} \tag{9}$$

where T is the trace pulse-width, t is the physical pulse duration, x is the delay-arm displacement in mm and s is the time displacement in milliseconds, which equals 32ps/ms. Assuming a sech^2 pulse-shape [11] then the laser has a pulse duration of 27ps (FWHM).

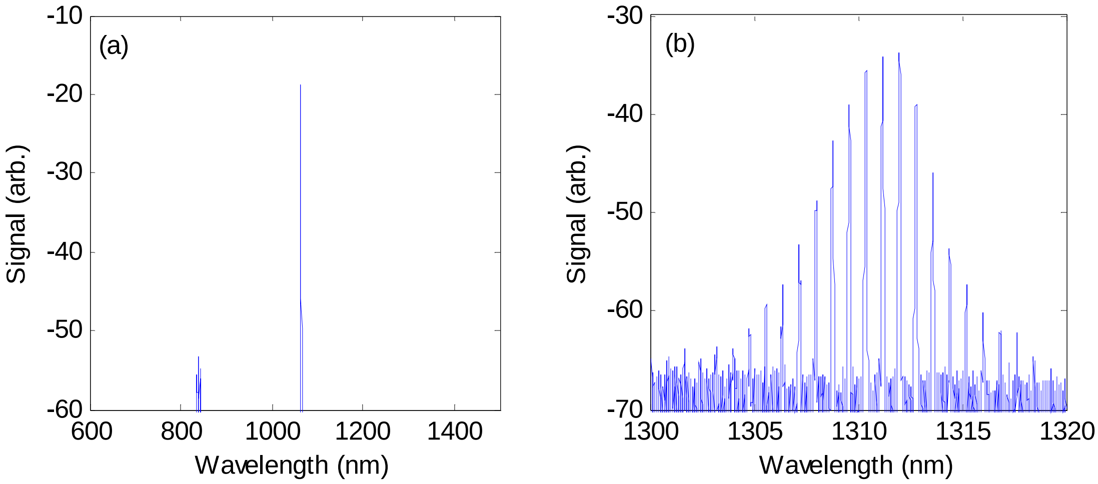

Figure 6.6: Spectra of (a) the pump and (b) the seed beams.

Figure 6.6 shows the pump (a) and seed (b) spectra measured before entering the fibre. The pump spectrum has a high intensity peak at 1064nm but also a smaller peak near 840nm due to the diode laser used to pump the Nd:YVO$_4$ laser. In figure 6.6b the spikes correspond to the longitudinal modes of the diode laser. It was discovered that the spectral position of the diode laser could be controlled to some extent by externally controlling the temperature of the laser. This effect was used to optimise the seed wavelength.

6.6 Results

6.6.1 Preliminary investigations with 10m fibre

The FWM PCF was fabricated by Crystal Fiber and had its zero group velocity dispersion wavelength (ZGVD) at 1070nm. Initially, a 10m length of fibre was used to verify that FWM did indeed occur within the fibre. The fibre was pumped with increasing power and the conversion efficiency and output spectra were monitored. The results are shown in figure 6.7 below. At a pump power of 1W no conversion occurs. However, as the power is increased to 5.8W, the conversion efficiency increases to ~1.8% for the 900nm peak and to ~0.4% for the 1310nm peak. Thereby confirming that FWM occurs in the fibre as predicted.

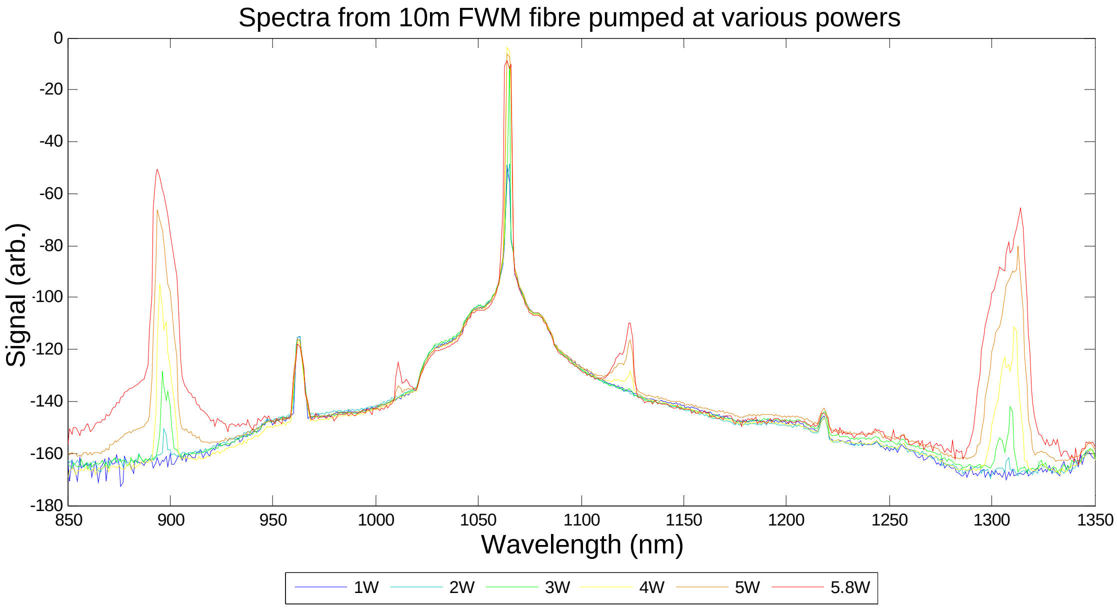

Figure 6.7: Output spectra from a 10m piece of four-wave mixing photonic crystal fibre when pumped at various powers.

The maximum output power of the laser had been reached so to increase the conversion efficiency further, a longer piece of fibre was tested, which provided a longer interaction length. A 150m piece was obtained and the experiment repeated.

To further enhance the conversion efficiency of the fibre, a diode laser at 1310nm was used to seed the four-wave mixing process. It is estimated that approximately 30μW was coupled into the fibre. The spectra were recorded for input powers ranging from

100mW to 7W, again to show the evolution of new wavelength generation within the fibre with power. For each of these powers it was necessary to realign both the input and output coupling as thermal and/or other effects caused the alignment to drift.

In initial test experiments the 150m fibre was pumped at 7W - the maximum power available. The power exiting the fibre was 1.86W. Laser power is lost through the fibre coupling, which was about 60% efficient, and also because of fibre losses as the light travelled through the fibre. Figure 6.8 shows the output spectrum obtained from the fibre with the 1310nm seed beam present. The linear plot is shown on the left and the logarithmic plot, which shows more of the spectral detail, on the right.

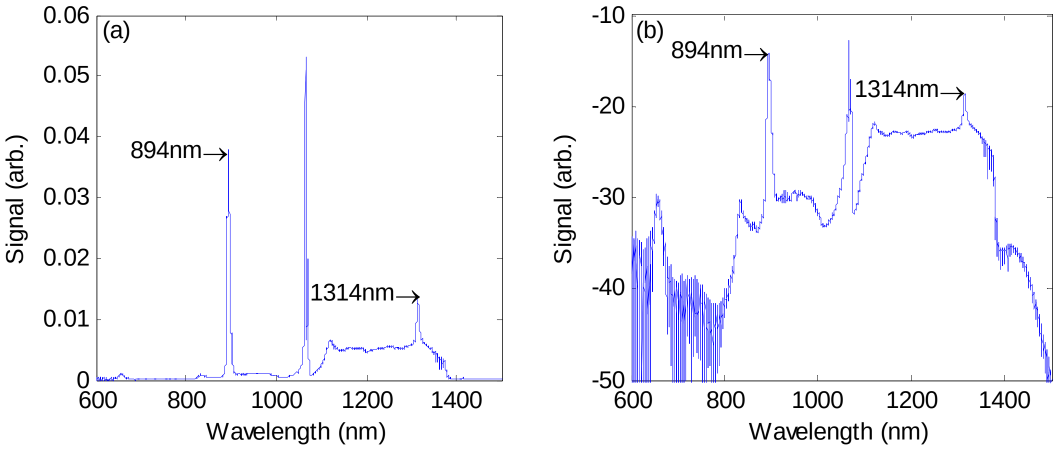

Figure 6.8: 1310nm seeded output spectra from 150m fibre pumped at 7W. a) shows power on a linear scale, b) shows a logarithmic scale.

The spectrum is very complex compared to the spectrum of the input beam, shown previously in figure 6.6a. This complexity arises due to the nonlinear effects occurring within the fibre. There are clear peaks at 894nm and 1314nm containing ~14% and ~9% of the output power respectively. These are generated parametrically through the FWM occurring within the fibre.

The pump beam is still clearly present. The peak has broadened and another weaker peak has formed at 1070nm, due to self-phase modulation (SPM). The peak has not broadened to the extent that femtosecond pulses would have. This type of response is discussed in detail by Wadsworth *et al* [12], who argues that SPM is not the main contribution to supercontinuum generation with picosecond pulses.

The majority of the radiation (~70% including the 1314nm peak) emitted from the fibre is present in a broadband continuum output between 1100nm and 1380nm. The continuum is very flat, varying in power by just 2-3dBm. A much weaker continuum containing ~20% of the light (including the 894nm peak) can be seen between 820nm and 1040nm.

There is also a fairly broad peak centred on 658nm. This increased with the four-wave mixing signals when the seed was present suggesting that it is related to the four-wave mixing process in some way. It is possible to conjecture that the 658nm signal arises from frequency doubling of the 1314nm signal, but this is unexpected in a non-centrosymmetric material such as silica. No second harmonic generation signal is observed at 532nm. To understand the complexity exhibited by the output spectrum the effects of both pump power and fibre length on the evolution of the spectrum were investigated.

6.6.2 Spectral output dependence on input power with 150m fibre

The spectra obtained by pumping the fibre at a range of input powers are shown in figure 6.9 (no seed) and figure 6.10 (diode seed at 1310nm). These are plotted on a logarithmic scale to display the spectral detail. The individual spectra plotted on a linear scale can be found in appendices 6-A (unseeded) and 6-B (seeded).

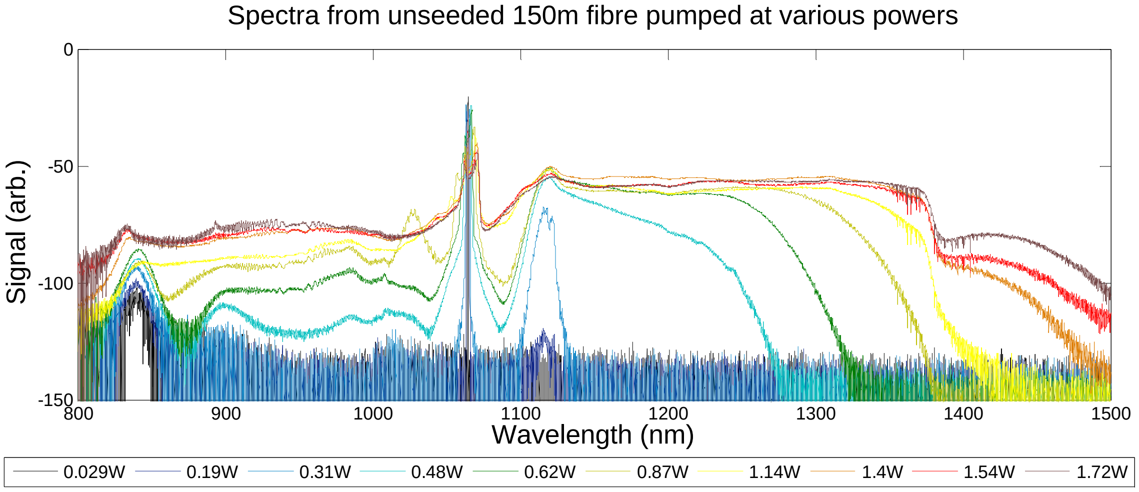

Figure 6.9: The output spectra from the 150 m fibre pumped at various power levels. A logarithmic scale is used to display the spectral detail. Appendix 6-A shows all of the individual spectra on a linear scale.

Output spectra were measured at input power levels of 100mW, 600mW, 1W, 1.5W, 2W, 3W, 4W, 5W, 6W and 7W. The corresponding output power levels are shown in the figure legends. No frequency conversion was observed at the lowest power level of 100mW (black) as illustrated in figure 6.9. However, as the power was increased to 600mW (indigo) the beginnings of a new peak formed at 1115nm. The magnitude of this peak increased dramatically as the power was increased to 1W (blue). The wavelength shift from 1064nm corresponds to the Raman-Stokes shift for silica. At higher power levels the Raman peak rapidly broadened, forming a supercontinuum (SC). At 1.5W the SC extended out to ~1275nm. At 2W it extended to 1325nm and to 1375nm by 3W. At an input power of 4W (yellow) the spectral extent of the SC stopped broadening. At higher power levels the SC became flatter as more power was transferred to the longer wavelengths. The power in each of the wavelengths varied by just ~2dBm between 1115nm and 1311nm resulting in a very flat SC over that region. The results indicate that the supercontinuum process is initiated by Raman shifting light into the anomalous dispersion region, where the supercontinuum process dominates.

There was some power transferred between 1380nm and >1500nm, the limit of the OSA, although this was weaker than the flat part of the SC. The reduction in generated power at 1380nm is believed to be due to OH absorption in the fibre, as shown in figure 6.2. It can also be seen that a broad continuum of much weaker power light (~20dBm down at 7W) was generated below the pump wavelength between ~840nm and ~1μm.

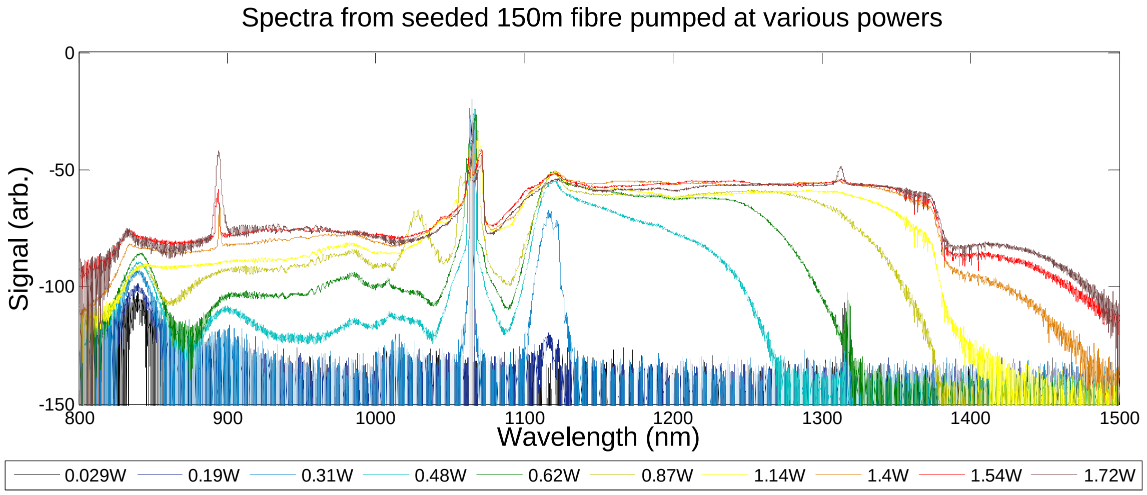

Figure 6.10: The output spectra from the 150 m fibre pumped at various power levels with a diode seed laser at 1310 nm. A logarithmic scale is used to display the spectral detail. Appendix B contains all of the individual seeded spectra on a linear scale.

With no seed beam present the FWM peaks at 894nm and 1315nm only became apparent at the highest powers (figure 6.9). The FWM requires high-peak powers – almost the maximum provided by the laser. The results obtained at equivalent power levels when the FWM process is seeded by the diode laser are shown in figure 6.10. It is clear that for this long length of fibre the FWM wavelengths only account for a small fraction of the transmitted power.

6.6.3 Spectral output dependence on fibre length

To investigate the effect of length on the evolution of the output spectrum the fibre was cut into various lengths and pumped at maximum power. Figure 6.11 shows the spectra generated both with and without the seed laser and table 1 shows the distribution of power to the various wavelength regions. For each measurement the coupling into the fibre was re-optimised. Therefore, in each case slightly different powers were coupled into the fibre. From experience, however, the difference should have been no greater than ~5%.

The spectra show that as the fibre length decreases the extent of the supercontinuum also decreases, along with the total power contained within it. Reducing the length from 150m to 100m results in less power being transferred to longer wavelengths. Further reducing the length, from 100m to 50m, sees the power drop by a larger amount. Comparing the 50m spectra to that from the 30m fibre sees the same pattern, with the power dropping even further. The SC is no longer as broad, either. This would suggest that when the length of the fibre is between 30m and 50m, the SC stops broadening. Instead, power is transferred from the pump to the longer wavelengths at a decreasing rate, flattening out the SC.

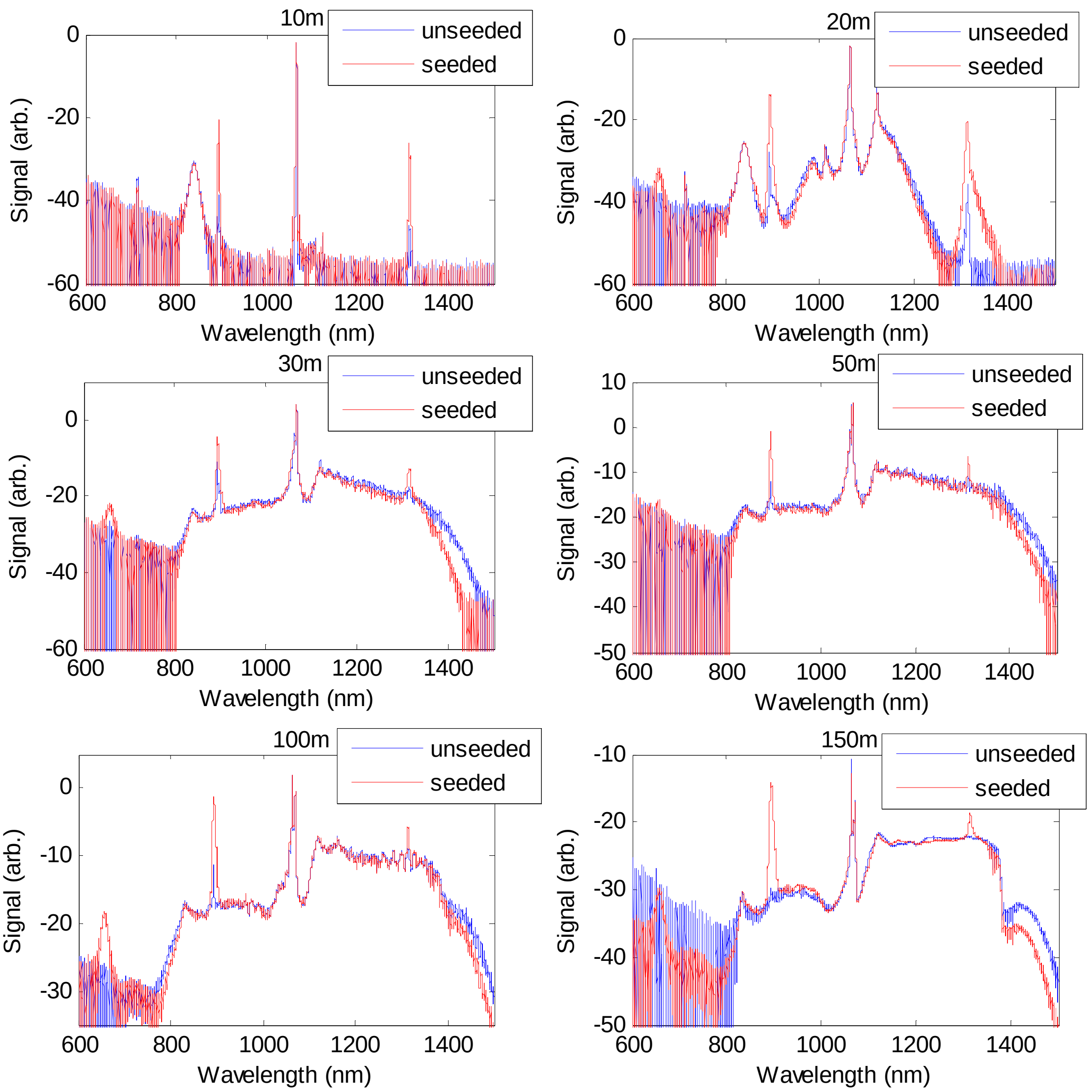

Figure 6.11: Output spectra of various lengths of fibre pumped at maximum power. The fibre length is displayed at the top of each chart. Each of the spectra can be found plotted on a linear scale in Appendices 6-C (unseeded) and 6-D (seeded). Due to different output coupling efficiencies only relative comparisons can be made between charts.

It does not appear as though using a longer fibre would have any benefit on the extent of the SC unless it is assumed that the SC stops at 1380nm due to OH absorption, then this could be masking the broadening of the SC until it extends beyond the wavelength absorption range. Indeed, looking at the 150m spectra it appears as though there is a broad peak of low power between 1400nm and 1500nm. This could be the continuation of the SC but there is insufficient data to make a firm conclusion about this.

It is also interesting to note that the signal at 658nm is observed in all the spectra where the 1314nm signal is clearly present, confirming its association with the four wave mixing process.

Fibre length	**Input Power (W)**	**Output Power (W)**	**894nm Peak**		**1064nm Peak**		**1314nm Peak**		**Supercontinuum**	
			Power (mW)	**%**	**Power (mW)**	**%**	**Power (mW)**	**%**	**Power (mW)**	**%**
150m	7	1.81	160	13.7	10	8.2	130	8.7	1200	70.7
100m	7.4	2.3	150	10.2	140	16.2	73	4.8	1300	66.3
50m	7.4	3	110	7.5	450	31.7	39	3.5	650	52.1
30m	7.35	3.6	310	12.8	670	41.1	90	4.1	520	37.6
20m	7.3	3	82	4.1	1970	78.7	15	1.3	140	14.2
10m	6.9	2.9	26	1.3	2600	96.4	7	0.5	0	0.5

Table 8.1: The power distribution of output spectra from different lengths of fibre when seeded with the diode laser. The plotted spectra can be found in Appendices 6-C (unseeded) and 6-D (seeded).

When the fibre is reduced in length from 30m to 20m the SC drops off rapidly. In fact at 20m the SC only extends from ~1110nm to ~1180nm. With only 10m of fibre no SC is present at all. This suggests that the fibre needs to be at least 30m for the continuum to broaden to its furthest extent with the power available.

The four-wave mixing generally seems to be more efficient with the longer fibre lengths. It is strange that with 30m of fibre the FWM generation is also very good however. This is either due to competing mechanisms within the fibre, or more likely the coupling of power into the fibre was particularly good for this experiment. The total output power is larger than with 20m, even though the power emitted by the laser has increased only slightly. This would confirm that the coupling was better than average in this case.

6.6.4 Supercontinuum fibre

Finally, a 30m long supercontinuum fibre purchased from Crystal Fibre was tested in a similar manner to the previous experiments. The ZGVD of the fibre is at 1040nm, so the pump wavelength of 1064nm lies within the anomalous dispersion regime.

The fibre was pumped with powers of 100mW, 1W, 1.5W, 2W, 2.5W, 3W, 4W and 4.5W. Coupling efficiency was around 33%. Figure 6.12 shows the output spectra obtained.

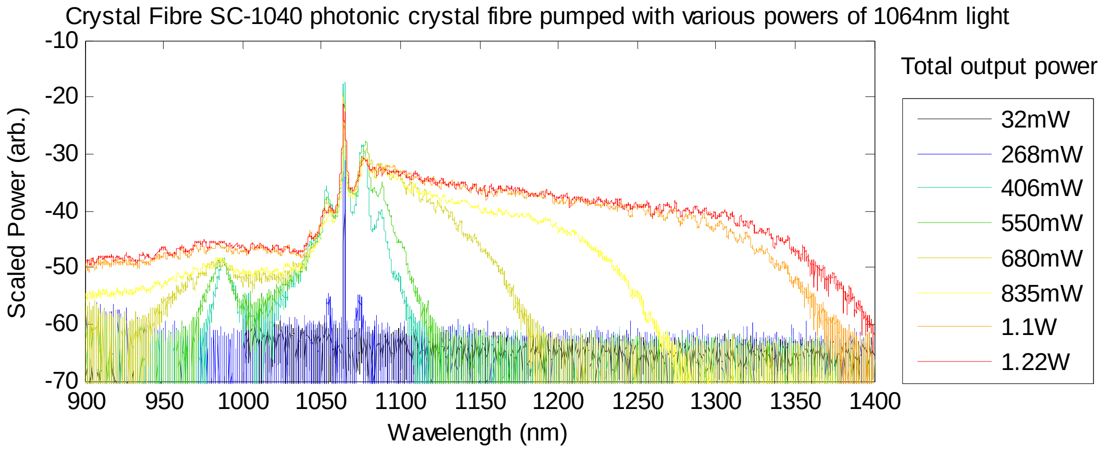

Figure 6.12: Spectra obtained from the fibre when pumped at different powers. The legend shows the output power. All the data is shown on the same chart to allow easy viewing of the supercontinuum evolution.

At low pump power, the beam is merely guided through the fibre and nothing unusual occurs. When 1W of pump power is used, side bands are generated on either side of the pump ~ 10nm away due to self-phase modulation. Increasing the pump power increases the amount of self-phase modulation and the pump becomes much broader, spanning from 1005nm to 1125nm when 2W is pumping the fibre. A secondary broad peak, containing ~ 0.8% of the output power and spanning 40nm, can be seen centred on 985nm. As the power is increased further, the two peaks merge together and broaden further. At 2.5W, only 30% of the light remains within 5nm either side of the pump wavelength. 5% of the output light is at shorter wavelengths than the pump, down to as far as 930nm. The majority of the light (65%), however, is found above the pump wavelength between 1070nm and 1190nm. The same pattern continues as the power is increased until at 4.5W only 17% of the output light lies within 5nm of the pump. Again

5% is found at shorter wavelengths, but now stretching to below 900nm. 78% of the light exists in a broad supercontinuum extending from 1070nm to 1380nm – the wavelength where OH bond absorption occurs.

Figure 6.13 shows the 4.5W spectrum on both linear (a) and logarithmic (b) scales. The plot on the linear scale is a better representation of the spectrum obtained. Although the magnitudes of the newly generated frequencies are much lower compared with the residual pump power, the frequencies are generated over a very broad range. For this reason, the total power is much greater. In contrast, the logarithmic plot highlights exactly where the power is transferred to. It is less useful for comparing power levels in those regions.

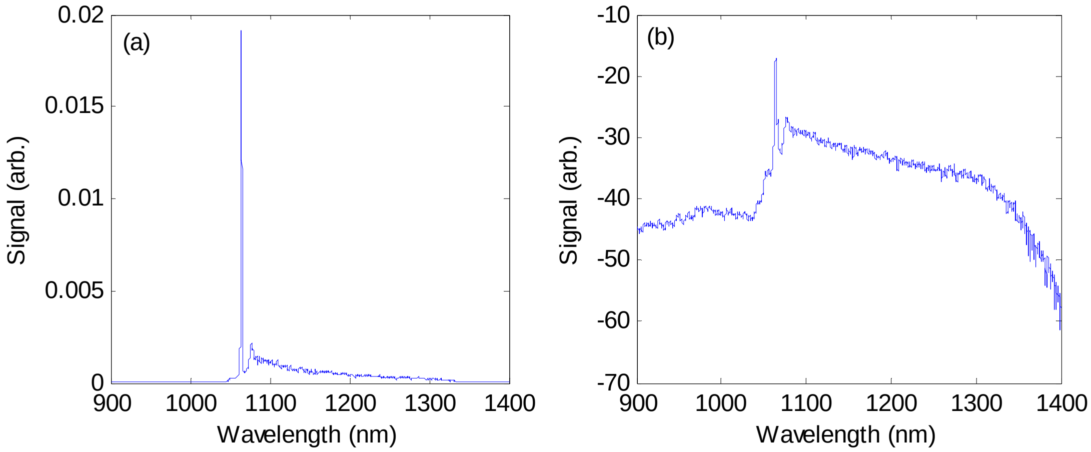

Figure 6.13: Spectrum obtained when the fibre was pumped at maximum (4.5W) power. (a) has a linear scale, which is more representative of the power levels obtained. (b) has a logarithmic scale, which shows the spectral detail more clearly.

6.7 Conclusions

A spectrally-flat supercontinuum laser source stretching from 1100nm-1380nm has been demonstrated by pumping a PCF with ZGVD at 1070nm with 27ps pulses of 1064nm light. Approximately 70% of the input power was converted into the supercontinuum.

The mechanism for the supercontinuum generation is somewhat unusual. The pump pulses are shifted into the anomalous dispersion regime via Raman scattering. The Raman scattered pulses then undergo broadening to form the supercontinuum. The pump pulse does not broaden significantly itself, as is the usual mechanism with femtosecond pulses.

FWM has also been demonstrated and used to generate light at 894nm and 1314nm with conversion efficiencies of ~14% and ~11%, respectively. This is a novel and potentially efficient technique for frequency conversion. An unexpected signal at 658nm was also observed. This signal is extremely close to that for frequency doubling from 1314nm and may indeed be a SHG signal. However this is particularly surprising because this would infer a $\chi^{(2)}$ process and the fibre is non-centrosymmetric.

6.8 References

1. JC Knight, TA Birks, P St J Russell, DB Atkin, “All-silica single mode optical fiber with photonic crystal cladding”, *Opt. Lett.*, **21** (19) 1547-1549 (1996); Errata, *Opt. Lett.*, **22** (7) 484-485 (1997)
2. From fibre specification sheet (Crystal Fibre)
3. GP Agrawal, *Nonlinear Fiber Optics*, 3rd ed. (Academic Press, 2001)
4. CV Raman, *Indian J. Phys.* **2**, 387 (1928)
5. EM Mitschke, LF Mollekauer, “Discovery Of the soliton Self-frequency shift” *Opt. Lett.* **11** 659-661 (1986)
6. JP Ciordon, “Theory of the soliton self-frequency shift” *Opt Lett.* **11**, 662-664 (1986)
7. S Coen, AHL Chau, R Leonhardt, JD Harvey, JC Knight, WJ Wadsworth, PStJ Russell, “Supercontinuum generation by stimulated Raman scattering and parametric four-wave mixing in photonic crystal fibers” *J. Opt. Soc. Am. B.* **19** 753-764 (2002)
8. KM Hilligsøe, HN Paulsen, J Thøgersen, SR Keiding, JJ Larsen, “Initial steps of supercontinuum generation in photonic crystal fibers” *J. Opt Soc. Am B.* **20** 1887-1893 (2003)
9. J Takayanagi, N Nishizawa, H Nagai, M Yoshida, T Goto, “Generation of high-power femtosecond pulse and octave-spanning ultrabroad supercontinuum using all-fiber system” *IEEE Phot. Tech. Lett.* **17** 37-39 (2005)
10. G Genty, M Lehtonen, H Ludvigsen, J Broeng, M Kaivola, “Spectral broadening of femtosecond pulses into continuum radiation in microstructured fibers” *Opt. Express.* **10** 1083-1098 (2002)
11. TH Graf, AI Ferguson, E Bente, D Burns, MD Dawson, “Multi-Watt ND:$YV0_4$ laser, mode-locked by a semiconductor saturable absorber mirror and side-pumped by a diode-laser bar” *Opt. Comms,* **159** 84-87 (1999)
12. WJ Wadsworth, N Joly, JC Knight, TA Birks, F Biancalana, P St J Russell, “Supercontinuum and four-wave mixing with Q-switched pulses in endlessly single-mode photonic crystal fibres” *Opt. Express.* **12** 299-399 (2004)

Appendix 6-A All individual unseeded 150m spectra

Spectrum when 150m fibre is pumped with 100mW

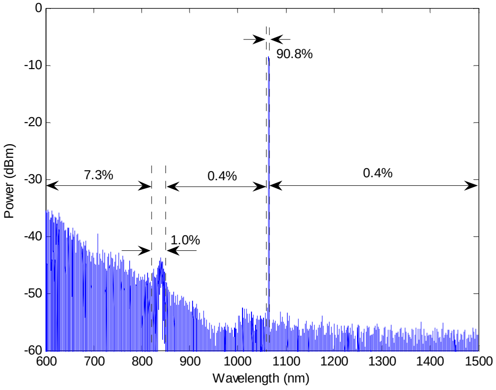

Spectrum when 150m fibre is pumped with 1.5W

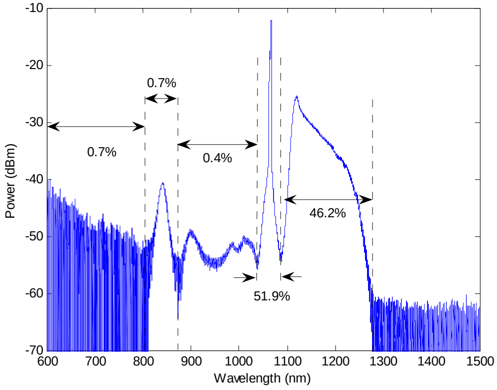

Spectrum when 150m fibre is pumped with 600mW

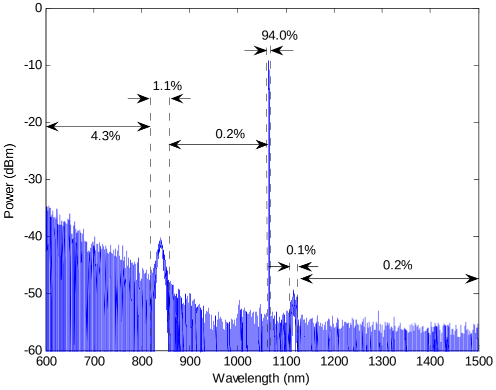

Spectrum when 150m fibre is pumped with 2W

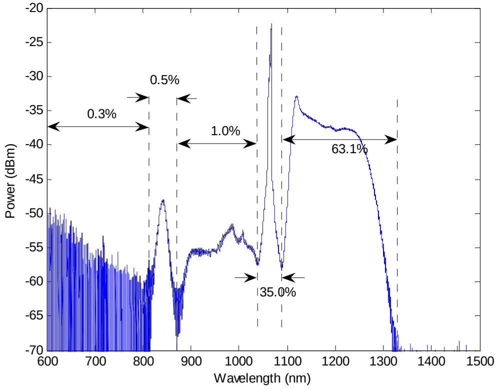

Spectrum when pumped with a power of 1W

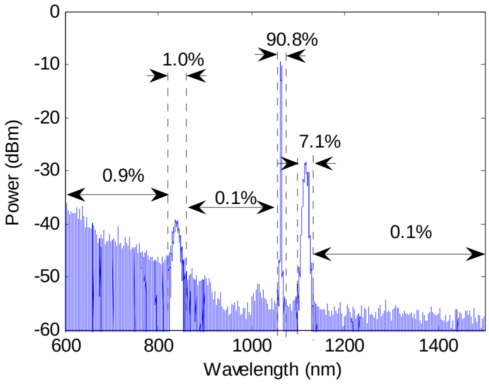

Spectrum when 150m fibre is pumped with 3W

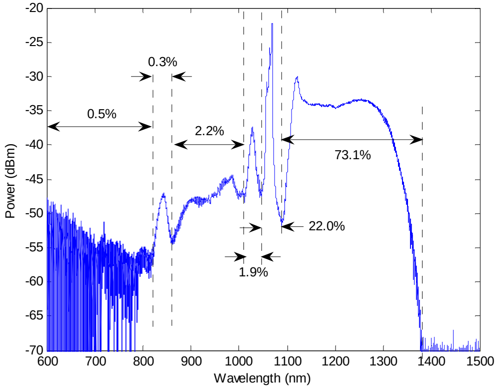

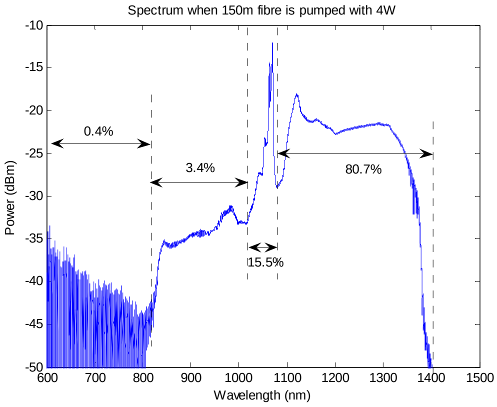
Spectrum when 150m fibre is pumped with 4W
Power (dBm)
Wavelength (nm)
-10
-15
-20
-25
-30
-35
-40
-45
-50
600
700
800
900
1000
1100
1200
1300
1400
1500
0.4%
3.4%
15.5%
80.7%

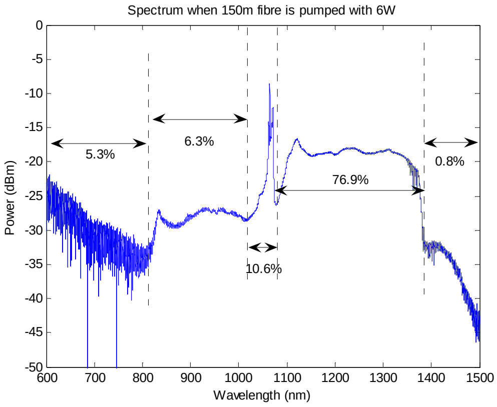
Spectrum when 150m fibre is pumped with 6W
Power (dBm)
Wavelength (nm)
0
-5
-10
-15
-20
-25
-30
-35
-40
-45
-50
600
700
800
900
1000
1100
1200
1300
1400
1500
5.3%
6.3%
10.6%
76.9%
0.8%

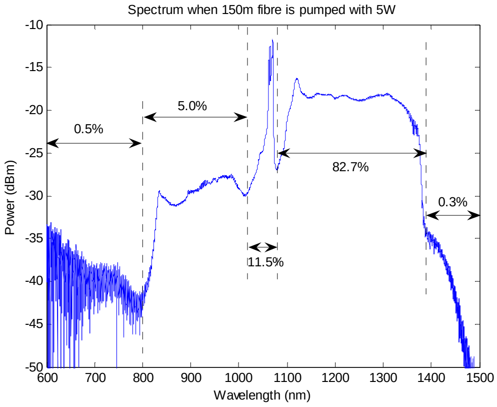
Spectrum when 150m fibre is pumped with 5W
Power (dBm)
Wavelength (nm)
-10
-15
-20
-25
-30
-35
-40
-45
-50
600
700
800
900
1000
1100
1200
1300
1400
1500
0.5%
5.0%
11.5%
82.7%
0.3%

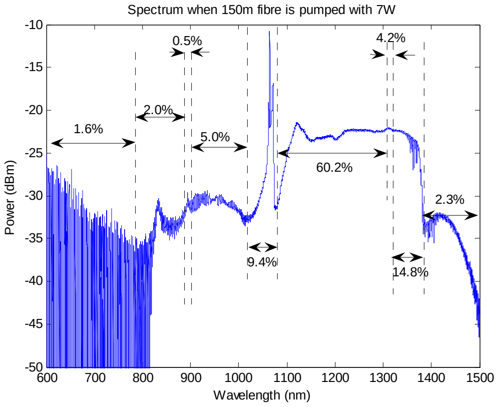
Spectrum when 150m fibre is pumped with 7W
Power (dBm)
Wavelength (nm)
-10
-15
-20
-25
-30
-35
-40
-45
-50
600
700
800
900
1000
1100
1200
1300
1400
1500
1.6%
2.0%
0.5%
5.0%
9.4%
60.2%
4.2%
14.8%
2.3%

Appendix 6-B All individual seeded 150m spectra

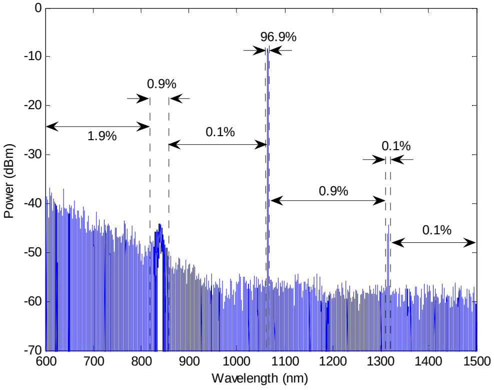
Spectrum when pumped with a power of 100mW and seeded with the diode laser

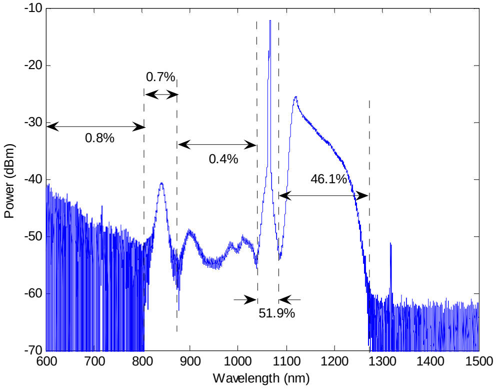
Spectrum when pumped with a power of 1.5W and seeded with the diode laser

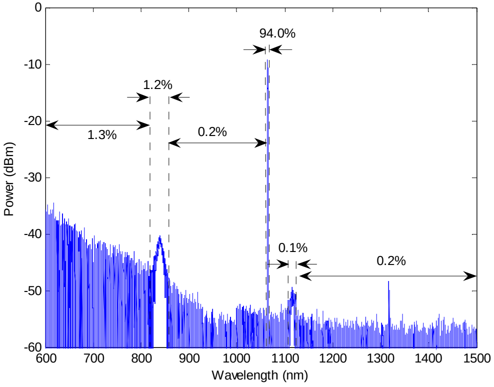
Spectrum when pumped with a power of 600mW and seeded with the diode laser

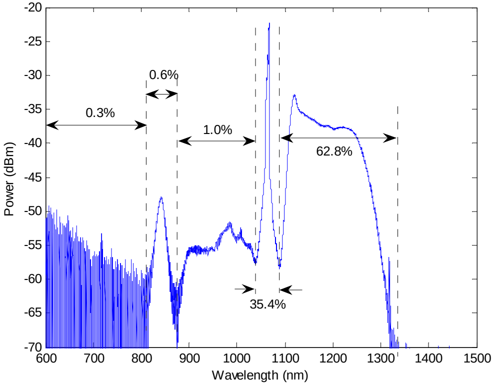
Spectrum when pumped with a power of 2W and seeded with the diode laser

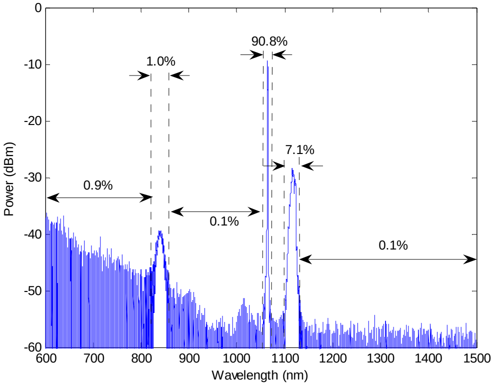
Spectrum when pumped with a power of 1W and seeded with the diode laser

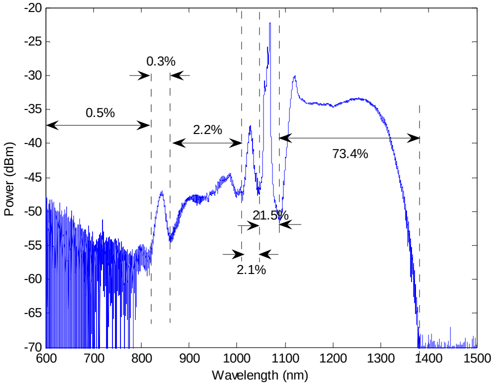
Spectrum when pumped with a power of 3W and seeded with the diode laser

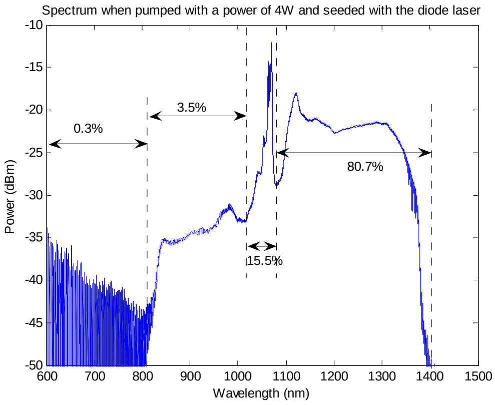
Spectrum when pumped with a power of 4W and seeded with the diode laser
Power (dBm)
Wavelength (nm)
-10
-15
-20
-25
-30
-35
-40
-45
-50
600
700
800
900
1000
1100
1200
1300
1400
1500
0.3%
3.5%
15.5%
80.7%

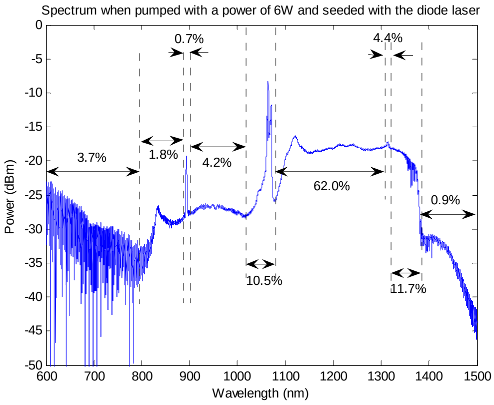
Spectrum when pumped with a power of 6W and seeded with the diode laser
Power (dBm)
Wavelength (nm)
0
-5
-10
-15
-20
-25
-30
-35
-40
-45
-50
600
700
800
900
1000
1100
1200
1300
1400
1500
0.7%
4.4%
3.7%
1.8%
4.2%
62.0%
0.9%
10.5%
11.7%

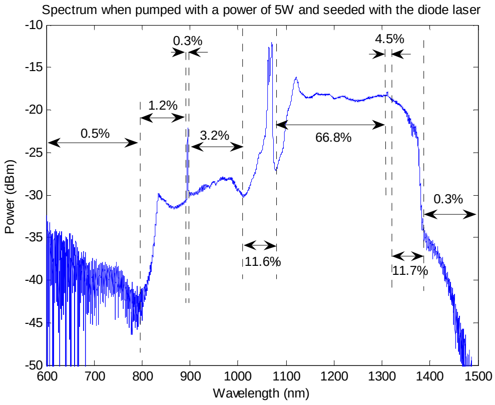
Spectrum when pumped with a power of 5W and seeded with the diode laser
Power (dBm)
Wavelength (nm)
-10
-15
-20
-25
-30
-35
-40
-45
-50
600
700
800
900
1000
1100
1200
1300
1400
1500
0.3%
4.5%
1.2%
0.5%
3.2%
66.8%
0.3%
11.6%
11.7%

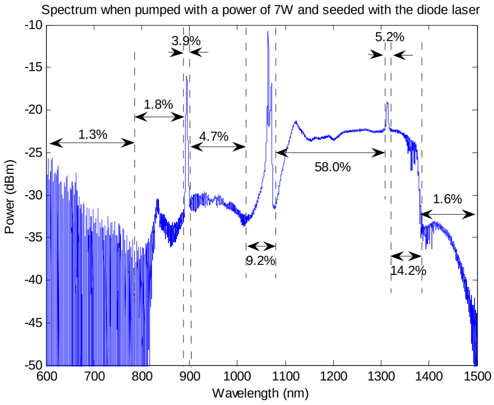
Spectrum when pumped with a power of 7W and seeded with the diode laser
Power (dBm)
Wavelength (nm)
-10
-15
-20
-25
-30
-35
-40
-45
-50
600
700
800
900
1000
1100
1200
1300
1400
1500
3.9%
5.2%
1.8%
1.3%
4.7%
58.0%
1.6%
9.2%
14.2%

Appendix 6-C All individual unseeded spectra from varying fibre lengths

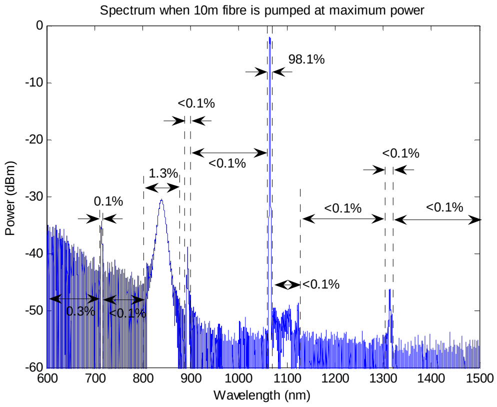

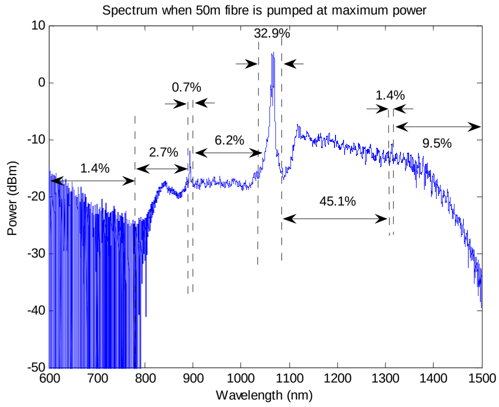

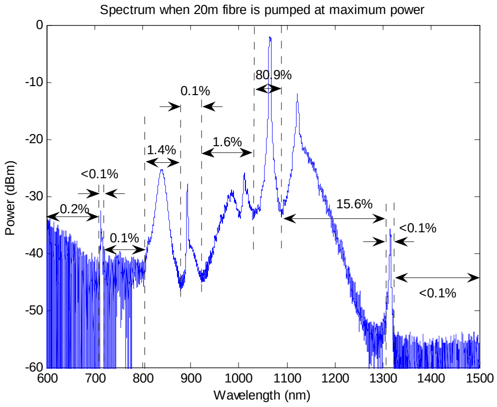

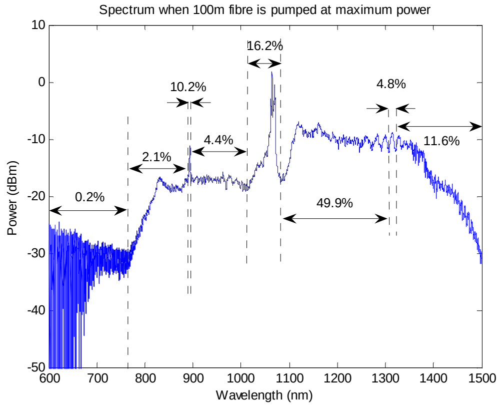

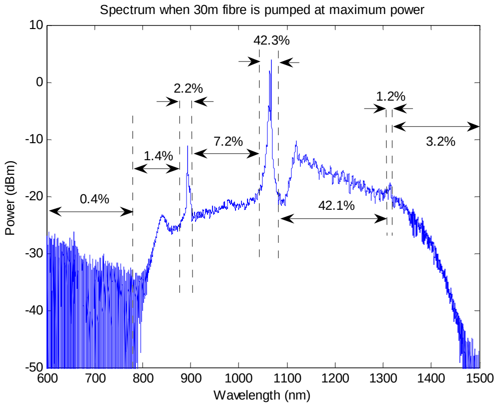

Appendix 6-D All individual seeded spectra from varying fibre lengths

Spectrum when 10m fibre is pumped at maximum power and seeded with the diode laser

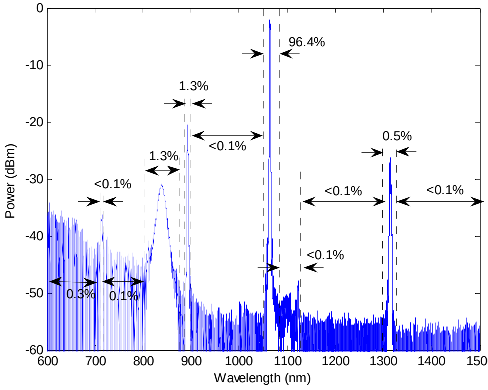

Spectrum when 20m fibre is pumped at maximum power and seeded with the diode laser

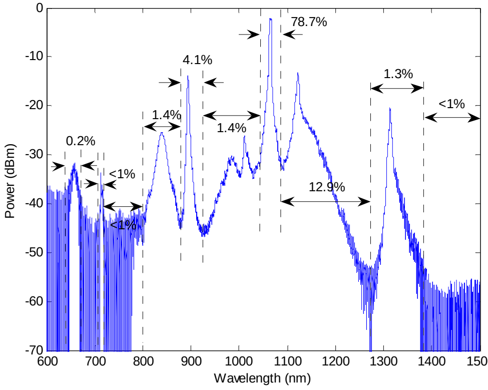

Spectrum when 30m fibre is pumped at maximum power and seeded with the diode laser

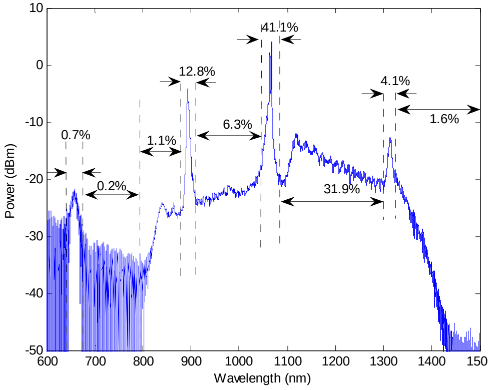

Spectrum when 50m fibre is pumped at maximum power and seeded with the diode laser

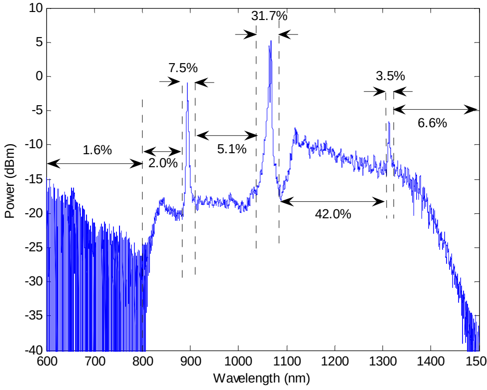

Spectrum when 100m fibre is pumped at maximum power and seeded with the diode laser

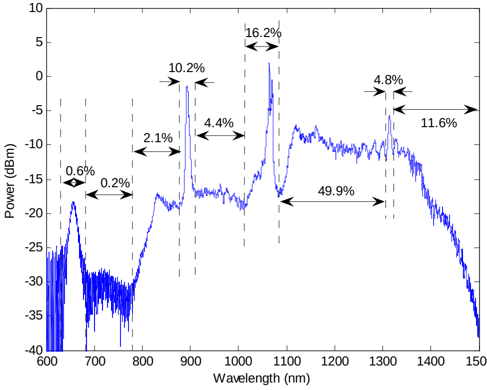

Spectrum when 150m fibre is pumped at maximum power and seeded with the diode laser

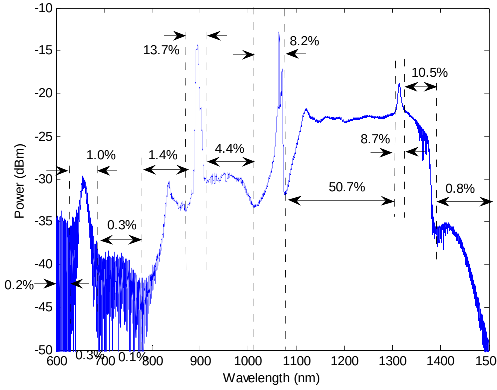

7 Conclusions

7.1 Introduction

In this chapter I draw together the conclusions on the nonlinear measurements on the indium phosphide and cadmium mercury telluride. The results of the experiments are summarised in section 6.2 to 6.4. In section 6.5, a further experiment is used to demonstrate that the nonlinear coefficients determined by me give a closer match to the experimental results than those reported before this study was started or those calculated from theory. Section 6.6 contains suggestions for further work and, finally, section 6.7 contains a list of references.

7.2 Measurement of β in indium phosphide

With long pulse durations, free-carriers produce a significant contribution to the observed absorption, hence the measured absorption is a combination of TPA and FCA. There is no way to separate these contributions under long pulse excitation. Instead, ultrafast pulses are used, as no free-carrier effects occur on such short timescales, allowing the TPA to be measured in isolation.

Open-aperture z-scans were performed at various input pulse energies using a laser producing pulses of 130 femtoseconds in duration. There were some issues with the results that could not be explained satisfactorily. The β values measured at different energies varied, dropping from 46cm/GW down to 12cm/GW as the energy was increased. Only the first 3 values, which were measured at relatively low energies, remained consistent at ~45cm/GW. This is slightly higher than the value predicted by theory (25cm/GW[1]) and the values measured by other researchers (22-35cm/GW[2] and 24-33cm/GW[3]). None of the obvious experimental problems, such as detector saturation or refraction causing beam spreading explain a decrease in the value of β as the energy is increased. Instead, it's possible that some unknown physical process resulting in saturation of the two-photon absorption is occurring, resulting in the TPA being weaker than expected.

7.3 Measurement of σ_{fca} in indium phosphide and cadmium mercury telluride

Two-photon absorption results in the generation of free-carriers. These free carriers simultaneously absorb and refract the beam. Open-aperture z-scans were performed in order to measure the free-carrier absorption coefficient. This involves measuring the light transmitted through a sample of the material being analysed as it is scanned through the focus of a beam. As the intensity increases near the focus, more TPA occurs, generating more free carriers, causing the beam to be more strongly absorbed. Because the scan measures the total amount of absorption in the material, β needs to be known so that the absorption due to TPA can be accounted for.

Unfortunately, analysis of the results revealed that the σ_{fca} was increasing with energy, which does not agree theory. Large nonlinear refraction occurs within the sample which causes the beam to spread. It is believed that the beam diameter becomes larger than the detector resulting in some of the beam not being collected, thus giving rise to a perceived transmission loss and leading to the incorrect deduction that the absorption has increased. This results in the measured value of σ_{fca} being larger than in reality. Therefore, the σ_{fca} values obtained in the analysis are overestimates, and only allow an upper limit to be determined.

The upper limits were found to be approximately $1\text{x}10^{-15}\text{cm}^2$ for the indium phosphide and approximately $3\text{x}10^{-15}\text{cm}^2$ for the cadmium mercury telluride whereas a more realistic value is believed to be $1\text{x}10^{-17}\text{cm}^2$.

7.4 Measurement of σ_r in indium phosphide and cadmium mercury telluride

The final experiments performed on the materials were closed-aperture z-scans. These experiments allow the nonlinear refraction to be quantified. As the refraction causes the beam size to vary over the aperture, the amount of light transmitted by the aperture varies. This is modelled using the parameters determined in the other experiments and values obtained from theory and the literature.

In each case the value obtained was consistent at different energy levels. When fitting the experimental data, different β values were used, as theory and experimental measurements in chapter 3 and in the literature did not tally with each other. In the case of the indium phosphide, β values of 22cm/GW at 1.064μm and 20cm/GW at 1.534μm were assumed. These came from a semi-empirical equation developed by Van Stryland et al.[1]. The σ_r values were found to be -5.1x10^{-20}cm^3 and -4.1x10^{-20}cm^3 respectively. These are both approximately 5 times those predicted by the theory of Wherret[4]. However, the quantity $\beta\sigma_{fca}$ was found to be constant at ~-113x10^{-20}cm^4/GW at 1.064μm and ~-84x10^{-20}cm^4/GW at 1.534μm. Therefore, increasing the value for β led to a reduction in the σ_{fca} value measured. Using 45cm/GW, the value that was measured in the femtosecond experiments in chapter 3, gives values of -2.5x10^{-20}cm^3 and -1.9x10^{-20}cm^3 at 1.064μm and 1.534μm respectively. These are approximately 2-3 times the values predicted by theory.

The experimental results are found to scale with wavelength in very good agreement with theory. Experimentally, the σ_r value at 1.064μm is 1.2 times the σ_r value at 1.534μm, whilst theory suggests the ratio is 1.24.

Similar experiments were performed on two pieces of CMT having band edges at 1.4mm (CMT1) and 1.5mm (CMT2). In the case of the first sample, σ_r was measured to be -1.7x10^{-20}cm^3. This is 2-3 times lower than the value predicted by theory. However, as with the indium phosphide, this number depended on the two-photon absorption coefficient used because the quantity $\beta\sigma_r$ is a constant (-148x10^{-20}cm^4/GW). Unfortunately, no results for the TPA coefficient could be found in the literature for the composition of the material used in the experiments, so a value of 87cm/GW calculated from theory was used.

The second CMT sample had a bandgap equal to the laser wavelength, resulting in significant linear absorption (75%). This linear absorption caused many more free-carriers to be generated than with the other semiconductor samples, which led to an order of magnitude increase in the nonlinear processes observed.

The linear absorption made the results difficult to quantify. The fitting model was altered to include an estimation of the effects of the linear absorption but the resulting experimental fit was poor. This was coupled with the fact that only one closed aperture z-scan could be performed due to the low energy levels used in the experiments causing detector noise to become an issue.

The important result however is that the nonlinear processes are increased significantly due to the presence of linear absorption, and the fact that the bandgap in CMT is tunable over a large wavelength range means it can be adapted for use at specific wavelengths.

7.5 Use of the experimentally determined parameters

A nonlinear transmission experiment with pulses of nanosecond duration was used to validate my measured parameters. A model developed by one of my supervisors was used to fit the experimental data. Data generated using my parameters and those of theory were compared to the results, as shown in figure 7.1.

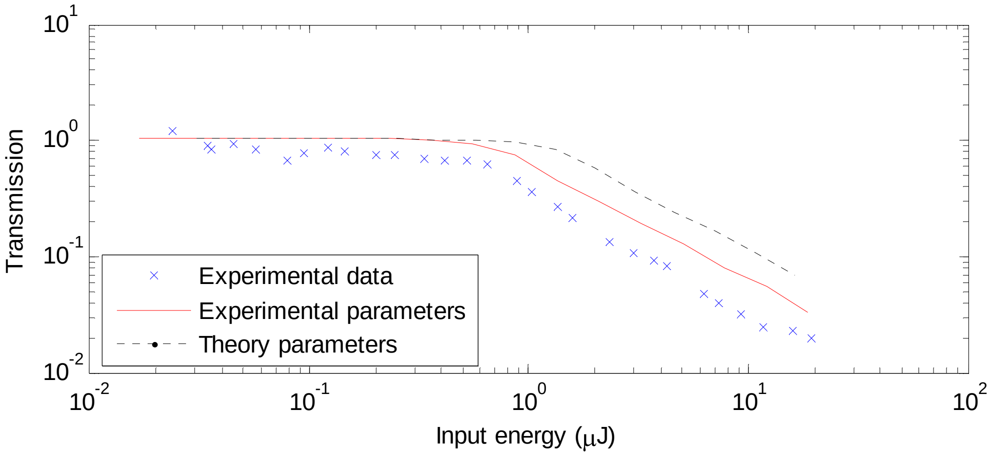

Figure 7.1: Graph showing InP transmission for varying input energy. The crosses are the experimental data, the lines are the fits. The red line is the fit generated using the free-carrier refraction cross-section value measured in chapter 4. The black line is the curve generated using values determined by theory.

As can be seen, my experimental values are a closer fit to the measured experimental data than the values calculated from theory. This suggests that one or more of the theoretical values are incorrect. However, the experimental values do not produce exact matches to the data. In order to get better agreement, either σ_r or β must be increased so that the overall refraction is increased.

7.6 Further semiconductor work

In order to measure the free-carrier absorption coefficient accurately the effects of refraction need to be removed from the experiment. This can be done by minimising the distance between the sample and the detector window. One possible way of doing this would be to bond the sample directly to the detector. However, this would probably introduce further experimental problems, because the sample would have to be scanned through the beam focus with the sample, making it susceptible to damage or nonlinear response as the beam becomes very small.

For the linearly absorbing CMT sample, it would be interesting to see what effect reducing the amount of absorption has on the nonlinear effects produced. This would allow optimisation of the CMT material for use at specific wavelengths. This will be done at some point in the future using a tunable wavelength to ‘walk’ the beam along the band edge, and measure the nonlinear refractive index cross-section versus wavelength.

7.7 New frequency generation in photonic crystal fibres

A photonic crystal fibre was pumped with a 1064nm laser to generate light at 894nm and 1314nm via four-wave mixing. The conversion efficiencies were 14% and 11% respectively. Typically, femtosecond lasers are used for such frequency conversion. However in this case, the laser pulses are 27ps in duration. This leads to a much higher average output power.

In addition, a spectrally-flat supercontinuum stretching between 1100nm and 1380nm was demonstrated. Approximately 70% of the input power was converted into the supercontinuum.

The mechanism for the supercontinuum generation is somewhat unusual. The pump pulses are shifted into the anomalous dispersion regime via Raman scattering. The Raman scattered pulses then undergo broadening to form the supercontinuum. The pump pulse does not broaden significantly itself, as is the usual mechanism with femtosecond pulses.

An oral presentation of this work was given at the Photon 06 conference in Manchester. The application of the fibre as a high average ouput power optical parametric amplifier has been published in Optics Express[5].

7.8 Future photonic crystal fibre work

The FWM conversion only began to occur at the highest powers available from the laser and whether any signal was observed depended strongly on the coupling efficiency. Therefore, using a higher peak power source should allow the FWM to be observed much more readily. The fact that the FWM peaks increase without the same increase in residual pump power exiting the fibre suggests the conversion should occur with greater efficiency.

Kafka and Baer [6] report using 100ps pulses to pump a standard optical fibre with optical feedback to generate ~200fs pulses. The nonlinear mechanisms involved are similar to those observed in the above experiments so it would be interesting to reproduce their experiment but with photonic crystal fibre. In this way we could dispense with the need to seed the nonlinear process and may achieve more efficient conversion.

This work demonstrates that it is possible to build a supercontinuum source in the short-wave infrared band (SWIR) at the watt level. This laser source, with a 30m long, supercontinuum fibre has been used as part of an active hyper-spectral imaging trial. The source was used to illuminate various materials and objects and the reflected spectra were measured at range.

7.9 References

1. E.W. Van Stryland, M.A. Woodall, H. Vanherzeele, M.J. Soileau "Energy band-gap dependence of two-photon absorption" *Opt. Lett.* **10** p490 (1985)
2. T. Sloanes, P.K. Milsom, K.J. McEwan, M.B. Haeri, T.O. Clatterbuck, J. McCartney, H. Bookey, A.K. Kar, "Two-photon induced free-carrier absorption and refraction in indium phosphide", *To be submitted to J. Appl. Phys.*
3. D. Vignaud, J.F. Lampin, F. Mollot,"Two-photon absorption in InP substrates in the 1.55μm range" *Appl. Phys. Lett.* **85(2)** p239 (2004)
4. B.S. Wherrett, A.C. Walker, F.P. Tooley, *Optical Nonlinearities and Instabilities in Semiconductors*, Ch10. Ed. Hartmut Haug (Academic Press 1998)
5. T.J. Sloanes, K.J. McEwan, L. Michaille, B. Lowans. "Optimisation of high average power optical parametric generation using a photonic crystal fiber", *Opt. Express.* **16** p19724 (2008)
6. JD Kafka, T Baer, "Fiber Raman soliton laser pumped by a Nd:YAG laser" *Opt. Lett.* **12** p181 (1987)